

# Numerical study of alfvénic wave activity in the solar wind as a cause for pitch angle scattering with focus on kinetic processes

Duncan Keilbach

Masterarbeit

July 23, 2017

## Abstract

Studies, that determine the inflow direction of the local interstellar medium from e.g. anisotropies in the longitudinal trend of interstellar pickup ions' radial velocity [e.g. Möbius et al. (2016)] give rise to the question how transport effects of interstellar pickup ions in the solar wind influence the pickup ion velocity distribution function (VDF). An undisturbed pickup ion VDF is believed to be a torus in velocity space [Drews et al. (2013)], which is believed to become isotropized by wave particle interactions quickly [Heerikhuisen et al. (2010)].

Therefore this study investigates the interaction between singly charged oxygen pickup ions and alfvénic waves numerically using a test particle approach. In contrast to other studies, which describe PUI transport using diffusion equations [e.g. Chalov and Fahr (1998)], this study aims to observe wave particle interactions qualitatively at the most basic level, where the trajectories of single particles in pitch angle space can be traced.

It has been concluded, that the interaction with continuous mono frequent alfvénic waves causes the particles to perform oscillatory stationary trajectories in pitch angle space. This means, that additional effects are needed to cause a systematic broadening of the pitch angle distribution. Therefore this study also investigates, how the test particles react to intermittent waves. A broadening of the pitch angle distribution similar to, what a diffusion approach from quasi-linear theory would expect [Schlickeiser (1994)] was observed. It was also observed, that the test particles did not interact most strongly at wave frequencies in resonance with the particles' gyro frequency. However, a strong modulation of the pitch angle distribution was found at wave frequencies close to the first order resonance.

Using a qualitative approach to investigate wave particle interactions in basic systems this study was able to disentangle, how typical parameters (such as wave frequency and amplitude) influence the modification of pitch angle distributions. We have also observed, that the interaction with a mono frequent wave is not systematically broadening pitch angle distributions over time. The superposition with other effects is needed, whereas the influence of intermittent wave fields has been investigated. Within the framework of this study it is possible to investigate, how a variety of these effects (like collisions with solar wind particles, gradient drifts in the interplanetary magnetic field or the interaction with typical wave spectra in the solar wind) influence wave particle interactions. Therefore this work is a first step to a better understanding of wave particle interactions at a basic level and on microscopic scales.

## Zusammenfassung

Im Rahmen von Studien, die die Einflussrichtung des lokalen interstellaren Mediums zum Beispiel auf der Basis der Anisotropie der Radialkomponente der Geschwindigkeit von interstellaren Pickup-Ionen als Funktion der ekliptischen Länge herausgefunden haben [z.B. Möbius et al. (2016)], hat sich die Frage nach dem Einfluss, den Transporteffekte im Sonnenwind auf die Geschwindigkeitsverteilungsfunktion der Pickup-Ionen haben, gestellt. Typischerweise sind Pickup-Ionen, die nicht durch Transporteffekte beeinflusst worden sind, auf einem Torus im Geschwindigkeitsraum verteilt [Drews et al. (2013)]. Man geht allerdings davon aus, dass diese Torus-Geschwindigkeitsverteilung vergleichsweise schnell durch Welle-Teilchen-Wechselwirkung isotropisiert wird [Heerikhuisen et al. (2010)].

Daher ist im Rahmen dieser Studie die Wechselwirkung zwischen einfach geladenen Sauerstoff-Pickup-Ionen und Alfvénwellen mit Hilfe eines Testteilchenansatzes numerisch untersucht worden. Im Vergleich zu vorangegangenen Studien [z.B. Chalov and Fahr (1998)] hat diese Studie das Ziel, die Interaktion qualitativ auf der elementarsten Ebene zu untersuchen, sodass Einzelteilchentrajektorien im Pitchwinkelraum nachverfolgt werden können.

Wir haben herausgefunden, dass die Interaktion mit kontinuierlichen monofrequenten Wellen zu stationären oszillatorischen Trajektorien der Testteilchen im Pitchwinkelraum führt. Diese sind insbesondere stationär, sodass die Wechselwirkung mit kontinuierlichen monofrequenten Wellen keine systematische Verbreiterung der Pitchwinkelverteilung über die Zeit bewirkt.

Daher wurde auch die Wechselwirkung mit intermittenter Wellen untersucht. Dabei ist eine Verbreiterung der Pitchwinkelverteilung als Funktion der Zeit gefunden worden, die den Erwartungen der quasi-linearen Theorie [z.B. Schlickeiser (1994)] z.T. entspricht. Die beobachtete Verbreiterung findet jedoch auf viel zu großen Zeitskalen statt. Darüber hinaus wurde beobachtet, dass keine vergleichsweise starke Interaktion der Teilchen bei resonanten Wellenfrequenzen stattfindet, allerdings für Frequenzen um die Resonanzfrequenz der ersten Ordnung herum eine starke Modifikation des Pitchwinkels stattfindet.

Mittels des qualitativen Ansatzes, den diese Arbeit zur Untersuchung von Welle-Teilchen Wechselwirkung in möglichst grundlegenden Systemen verwendet hat, ist der Einfluss typischer Parameter (wie Wellenfrequenz -und Amplitude) auf die Modifikation von Pitchwinkelverteilungen einzeln untersucht und entschlüsselt worden. Es wurde dabei herausgefunden, dass die Interaktion mit monofrequenten Wellen alleine keine systematische Verbreiterung der Pitchwinkelverteilung über die Zeit auslöst. Hierzu ist die Superposition mit anderen Effekten erforderlich, wobei diese Studie den Einfluss intermittenter Wellenfelder untersucht hat. Es ist darüber hinaus auf Basis dieser Studie möglich, den Einfluss solcher Effekte (zum Beispiel Kollisionen mit Sonnenwindteilchen, Gradientendrifte im interplanetaren Magnetfeld oder die Interaktion mit für den Sonnenwind typischen Wellenspektren) genauer zu untersuchen. Daher ist diese Arbeit ein erster Schritt, um Welle-Teilchen Wechselwirkung auf einer grundlegenden Ebene und auf mikroskopischen Skalen besser zu verstehen.

# Contents

<b>1</b>	<b>Introduction</b>	<b>1</b>
<b>2</b>	<b>Theoretical overview</b>	<b>2</b>
2.1	The Heliosphere and the solar wind . . . . .	2
2.2	Pickup Ions (PUIs) . . . . .	3
2.2.1	Production of interstellar Pickup Ions . . . . .	4
2.2.2	Global velocity characteristics of PUIs . . . . .	5
2.2.3	Local phase space distribution of PUIs . . . . .	6
2.3	Disturbances in the IMF and alfvénic turbulence . . . . .	8
2.3.1	Modification of PUI velocities by the global magnetic field geometry . . . . .	10
2.3.2	Large scale disturbances in the IMF . . . . .	10
2.3.3	Alfvénic turbulence . . . . .	12
2.3.4	Alfvénic cyclotron waves . . . . .	13
2.4	Interaction between particles and alfvénic waves . . . . .	14
2.4.1	General considerations . . . . .	14
2.4.2	Resonant wave particle interactions . . . . .	16
2.4.3	Quasi-Linear theory . . . . .	18
2.5	Goal of this work . . . . .	19
<b>3</b>	<b>Methodology</b>	<b>21</b>
3.1	Modeling the particles' motion . . . . .	21
3.1.1	The PUIs' equations of motion . . . . .	21
3.1.2	Time step-Algorithms . . . . .	21
3.1.3	Implementation of the Leapfrog algorithm for electric -and Lorentz force .	22
3.1.4	Coupling of field -and particle equations . . . . .	23
3.2	Implementation of initial particle and field conditions . . . . .	25
3.2.1	Feeding predefined magnetic structures into the simulation . . . . .	25
3.2.2	Implementation of intermittent waves . . . . .	27
3.2.3	Implementation of particle boundary conditions . . . . .	29
3.2.4	Choice of time step . . . . .	30
3.3	Derivation of the pitch angle . . . . .	32
<b>4</b>	<b>Simulation setup</b>	<b>34</b>
4.1	Guidelines . . . . .	34
4.2	Simulation setup ordered by chapter . . . . .	35
<b>5</b>	<b>Results and discussion</b>	<b>39</b>
5.1	Interactions of oxygen PUIs with a continuous, single frequency wave . . . . .	39
5.1.1	Trajectories of selected torus particles . . . . .	39
5.1.2	Study of the case of first-order resonance: perpendicular acceleration -and deceleration . . . . .	46
5.1.3	Time-evolution of the pitch angle distribution of an initial torus . . . . .	48
5.1.4	Time-averaged pitch angle distributions as a function of the wave frequency	51
5.1.5	Study of wave particle interactions as a function of the wave amplitude .	55
5.1.6	Conclusions . . . . .	64
5.2	Interactions of oxygen PUIs with an intermittent, single frequency wave . . . . .	66
5.2.1	Convoluting continuous waves with an activation function . . . . .	66
5.2.2	Convoluting continuous waves with a deactivation function . . . . .	70
5.2.3	Intermittent wave fields . . . . .	73
5.2.4	Parameter studies for intermittent wave fields . . . . .	75

5.2.5	Scattering of the particle energy . . . . .	81
<b>6</b>	<b>Conclusions</b>	<b>83</b>
<b>7</b>	<b>Outlook</b>	<b>85</b>
<b>8</b>	<b>Bibliography</b>	<b>88</b>
<b>9</b>	<b>Tools and utilities</b>	<b>91</b>
<b>10</b>	<b>Acknowledgments</b>	<b>92</b>
	<b>Appendices</b>	<b>93</b>
<b>A</b>	<b>Time averaged pitch angle distributions as a function of the wave frequency for initial pitch angles of <math>105^\circ, 120^\circ, 150^\circ</math> and <math>175^\circ</math> exposed to continuous waves of <math>0.1 \text{ nT}</math> amplitude</b>	<b>93</b>
<b>B</b>	<b>Time derivative of the parallel velocity component from Newton's equation</b>	<b>96</b>
<b>C</b>	<b>A wave-influenced particle's energy in the bulk frame as a function of its pitch angle</b>	<b>97</b>
<b>D</b>	<b>Modification of the parallel velocity by waves</b>	<b>98</b>
<b>E</b>	<b>Implementation of alfvénic waves propagating along the Parker spiral</b>	<b>99</b>
<b>F</b>	<b>Video: Animated particle velocity under the influence of a continuous mono frequent wave field</b>	<b>100</b>

---

## 1 Introduction

The transport of pickup ions (PUIs) through the interplanetary magnetic field has been a matter of many studies (e.g. Keilbach (2015), Chalov (2014) or Florinski et al. (2010)). Especially the question of how the velocity distribution function of pickup ions, which is anisotropic at the time of a PUI's injection [Drews et al. (2013)], is isotropized in the interplanetary magnetic field is a topic of high interest. Mostly the interaction with waves in the solar wind is held responsible for this [e.g. Heerikhuisen et al. (2010)].

Hence this work investigates the interaction of pickup ions - treated as test particles - with alfvénic waves in the solar wind (using an approach similar to Lehe et al. (2009)). In contrast to other studies, which treat the PUI transport through diffusion approaches [e.g. Isenberg (2005); Heerikhuisen et al. (2010)], this work aims to study the interactions at the most basic level possible with focus on the question, which basic assumptions are needed to the system in order to obtain isotropization of initially anisotropic pitch angle distributions. So this work studies wave particle interactions qualitatively in systems as basic as possible.

---

## 2 Theoretical overview

In this chapter we will focus on providing the theoretical aspects necessary for this work.

### 2.1 The Heliosphere and the solar wind

Before discussing nature and origin of pickup ions a brief introduction to the solar wind, which can be seen as the plasma background, through which pickup ions move, is given.

The solar wind is a continuous stream of approximately radially expanding ionized and magnetized gas originating at the Sun [McComas et al. (2000)]. Typical solar wind velocities range from 200 km/s to 800 km/s, where one roughly distinguishes between fast solar wind (velocities above 450 km/s) and slow solar wind (velocities below 450 km/s) [Kallenbach et al. (2000)]. Parker (1958) introduced a common model to describe the solar wind under idealized solar minimum conditions on large scales in both spatial and temporal dimensions:

Since the kinetic pressure in the solar wind exceeds the magnetic pressure, the interplanetary magnetic field (IMF) - embedded into the solar wind - is governed by the solar wind's motion (frozen-in field) [Schatten et al. (1969)]. So the solar wind expands radially outwards. At the same time the photosphere, which is believed to be the location, where solar wind streams originate, is performing a rotation, meaning that the sources of solar wind also rotate differentially. This causes a solar wind stream to appear curved towards a spiral (like water originating from a sprinkler). Hence the magnetic field - carried by the solar wind - has the shape of an in-ecliptic spiral [Parker (1958)].

This in-ecliptic spiral magnetic field, called the Parker spiral is given by

$$\vec{B}(r) = B_0 \cdot \left( \frac{r_0}{r} \right)^2 \cdot \left( \vec{e}_r - \frac{\Omega_\odot \sin(\theta)}{v_r} \vec{e}_\phi \right), \text{ where} \quad (1)$$

$\Omega_\odot$  describes the photosphere's rotational period at the latitude  $\theta$  and  $v_r$  is the solar wind's initial velocity and  $\vec{e}$  is given by  $\vec{e}_\phi$  (unit vector pointing in azimuthal direction), but tilted by  $\theta$  (the inclination angle with respect to the in-ecliptic plane) [Scherer et al. (2000)].  $B_0$  is a scaling factor, that determines the magnetic field at a fixed distance  $r_0$ . Typically  $r_0$  is set to 1 AU, so that  $B_0$  means the IMF strength at earth's orbit. Although that value is generally fluctuating in a realistic situation a good guideline value is  $B_0 = 5$  nT [Prölss (2003)]. The by-streaming plasma gives rise to an electric  $-\vec{v}_{sw} \times \vec{B}$ -field with  $\vec{v}_{sw}$  being the solar wind velocity. It consists of the radial expansion and the initial velocity component obtained from the photosphere's rotation  $\vec{v}_{sw} = \vec{u} + \vec{\Omega}_\odot \times \vec{r}$  [Scherer et al. (2000)]. This yields an electric field given by

$$\vec{E} = -\Omega_\odot r_0^2 \frac{B_0}{r} \sin(\theta) \vec{e}_\phi. \quad (2)$$

An example of the Parker spiral IMF can be seen in fig. 1.

The region in space governed by the solar wind is called the Heliosphere [McComas et al. (2012)] (compare fig. 1). It moves through a thin cloud of partly ionized gas, called the local interstellar medium (LISM) with a velocity of about 25.4 km/s and a temperature of  $\sim 1$  eV [McComas et al. (2015)]. At the point, where the expanding solar wind hits the LISM, it is decelerated and a boundary between the LISM and the solar wind is emerging called the heliopause, which has been observed by Voyager 1 at a distance of  $\sim 120$  AU from the Sun [Gurnett et al. (2013)]. The solar wind is a medium generally streaming at supersonic velocities. This gives rise to a shock wave in the solar wind downstream of the heliopause. Because of the curved geometry of the heliospheric boundary the solar distance of this shock, called the termination shock varies with the direction, where it is observed. It has been observed by Voyager 1 at  $\sim 94$  AU distance from the Sun [Stone et al. (2005)] and by Voyager 2 at a distance of  $\sim 83$  AU [Burlaga et al.

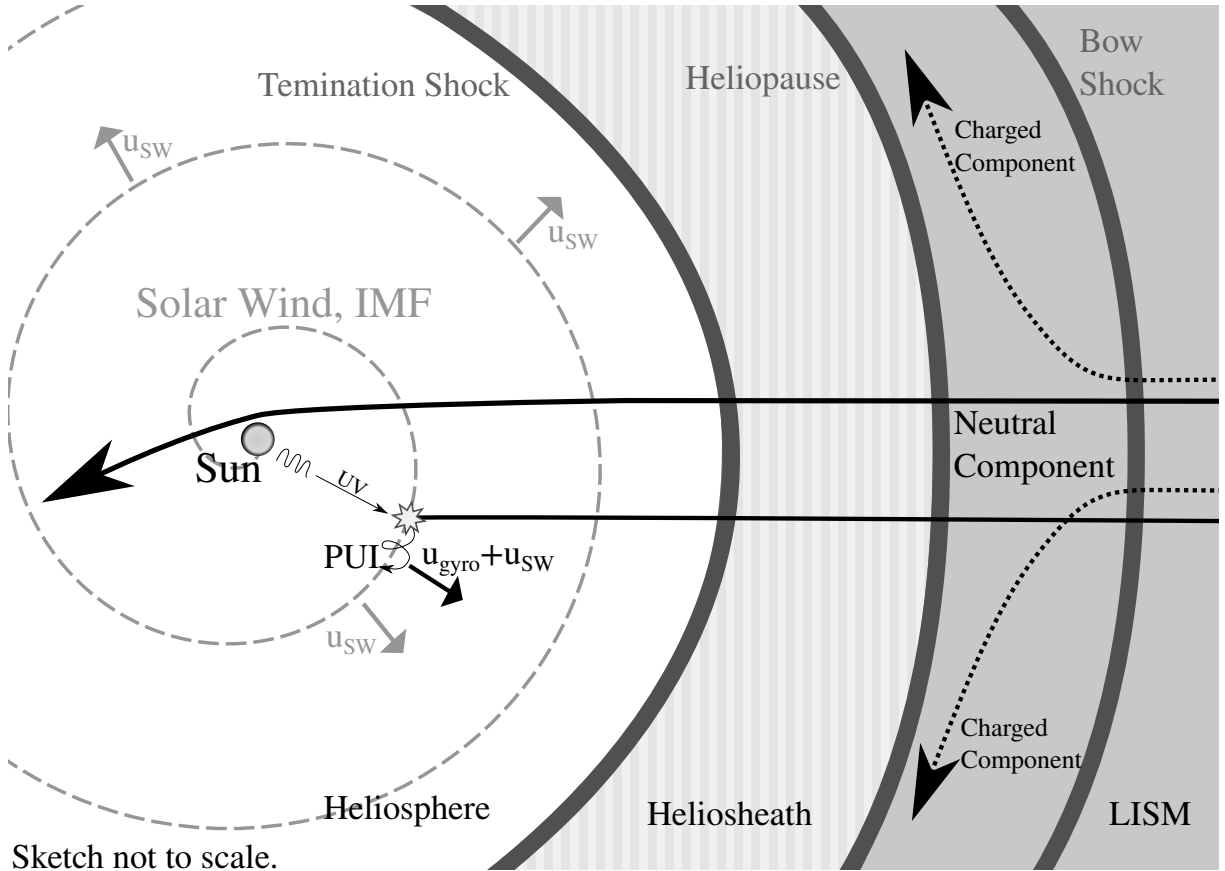


Figure 1: Sketch to visualize the origin of interstellar pickup ions. The neutral component of the LISM enters the heliosphere (two example trajectories are drawn) and forced onto Kepler orbits by the Sun's gravitational force. Through ionization (e.g. photoionization from solar UV radiation as shown in the figure) the neutrals can become ionized. After ionization these particles are bound to gyro orbits around the IMF, which is governed by the solar wind's kinetics [Vasyliunas and Siscoe (1976); Kallenbach et al. (2000)].

(2008)]. A textbook guideline value is given by e.g. Prölss (2003), which locates the termination shock at  $\sim 80$  AU distance from the Sun. Conversely, the charged component of the LISM hitting the heliospheric boundary gives rise to a shock wave in the LISM in front of the heliosphere's motion - the Bow Shock. However, its existence is a matter of great discussion at the moment [McComas et al. (2012)]. Since no direct observation of the Bow Shock exists at the moment, its distance to the Sun can not be stated exactly. A typical textbook value [e.g. Prölss (2003)] is  $\sim 350$  AU .

## 2.2 Pickup Ions (PUIs)

While the charged component of the LISM is deflected at the heliopause by the interplanetary magnetic field (IMF), the LISM's neutral component can enter the Heliosphere, since it is unaffected by magnetic and electric fields [Kallenbach et al. (2000)]. In the Heliosphere a neutral's motion is generally influenced by two forces: The Sun's gravitational force, which is inversely proportional to the solar distance squared, and the radiation pressure caused by the Sun's light. However, for all neutrals except Hydrogen and to some extent Helium the radiation pressure is negligible. Hence the interstellar neutrals perform Kepler orbits around the Sun [Vasyliunas and Siscoe (1976)]. In fig. 1 such an orbit is sketched as an example trajectory of an interstellar neutral.

The Kepler orbits give rise to a region in the heliosphere, where enhanced densities of neutral

---

particles are expected because of gravitational focusing. This region can be found in opposite direction to the inflow direction of the LISW with respect to the Sun. Traces of this region have been observed in interstellar pickup ion densities [Moebius et al. (1995)].

These come into existence, when an interstellar neutral is ionized in the Heliosphere. Being charged the former neutral experiences Lorentz-force caused by the IMF and is therefore forced onto gyro orbits around its field lines, which as introduced in chapter 2.1 are carried by the solar wind. So effectively the guiding center of the newly created ion's motion is "picked-up" by the solar wind. That's why this species of ions is called pickup ions (PUIs) [Vasyliunas and Siscoe (1976); Moebius et al. (1985)].

### 2.2.1 Production of interstellar Pickup Ions

The ionization of interstellar neutrals is accomplished through three processes: The most dominant process is photoionization through solar UV photons [Cummings et al. (2002); Ruciński et al. (1996)] (compare fig. 1). Especially important for heavy neutrals is charge exchange [Cummings et al. (2002); Ruciński et al. (1996)] with the solar wind. Lastly, there is the probability of ionization from electron impact [Möbius et al. (2004)]. In the following the former two will be discussed.

The probability of photoionization is dependent on the abundance of solar UV photons. Hence it is dependent on structures on or above the solar surface and of course dependent on the solar cycle (the reader may refer to Bochsler et al. (2014)). In order to simplify the calculations and focus on the basic physical processes, it is convenient to omit these dependencies and consider the flux of UVs originating at the Sun to be isotropic. This means, that the number of UVs on the surface of any sphere centered around the Sun is constant. Hence the density of UVs scales with the distance to the Sun like  $r^{-2}$ . Considering, that (apart from an energy dependent cross section for photoionization) the probability of being photoionized is proportional to the probability of hitting an UV photon, which scales with the UV density, we conclude, that the probability of photoionization per time unit scales like  $r^{-2}$  (This approach was used in e.g. Sokół et al. (2016)). Using the approach

$$P_{ion}(r) = P_0 \cdot \left(\frac{r_0}{r}\right)^2 \quad (3)$$

and setting  $r_0 = 1$  AU we can obtain values at all distances to the Sun linked to measurements of PUI production rates from photo-ionization at 1 AU. These are compiled in the following table.

Ion species	PUI production rate at 1 AU [Cummings et al. (2002)] $P_0 / s^{-1}$
He	$(1.18 \pm 0.10) \cdot 10^{-7}$
O	$(4.86 \pm 0.30) \cdot 10^{-7}$
Ne	$(3.60 \pm 0.29) \cdot 10^{-7}$

The probability of ionization by charge exchange can also be approximated by the  $r^{-2}$ -approach, since it is dependent on the solar wind density [Ruciński et al. (1996); Cummings et al. (2002)], which in the idealized Parker model (introduced in chapter 2.1) scales with  $r^{-2}$  [Parker (1958)]. It is a crude approximation, since the solar wind is a highly turbulent medium containing various macroscopic and microscopic structures [Tu and Marsch (1995)]. Already when considering a simple model, where only two solar wind streams are considered, the  $r^{-2}$ -approach will fail (as it will be described in chapter 2.3.2). For a better approximation extensive data of the solar wind density as a function of location in three dimensions throughout the heliosphere would be needed, which does not exist. Obtaining such density profiles from simulations would require MHD simulations of the solar wind, which is beyond the scope of this work. So the crude approximation is a justifiable approach, that allows us to look at the basics of PUI physics, while anisotropies coming from anisotropic injection rates (the interested reader may refer to Sokół

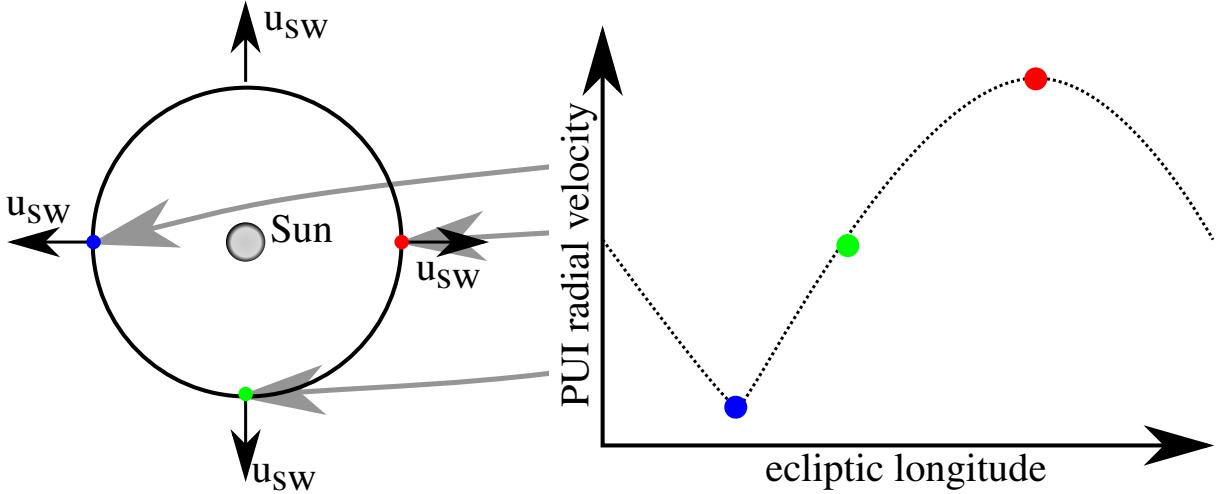


Figure 2: Visualization of the dependency of the PUI cutoff velocity on the ecliptic longitude. On the left hand side example ISN trajectories are shown for three characteristic ecliptic longitudes leading through vector addition to the velocity profile sketched on the right hand side.

et al. (2016)) are omitted. In the following table PUI production rates from charge exchange at 1 AU are compiled.

Ion species	PUI production rate at 1 AU [Cummings et al. (2002)] $P_0 / s^{-1}$
He	$(3.40 \pm 0.39) \cdot 10^{-10}$
O	$(3.61 \pm 0.08) \cdot 10^{-7}$
Ne	$(4.67 \pm 0.53) \cdot 10^{-9}$

It can be seen, that charge exchange is especially relevant for oxygen neutrals.

### 2.2.2 Global velocity characteristics of PUIs

Pickup ions move under the influence of the Lorentz force and are therefore forced onto gyro-orbits around the IMF. The IMF is carried by the solar wind, so the gyro orbits are carried by the solar wind in an outward motion (compare fig. 1). That's why these ions are called pickup ions - they have been picked up by the solar wind [Kallenbach et al. (2000)]. The overall PUI velocity is therefore a superposition of the solar wind speed and the gyro-motion, which (apart from transport effects) is given by the neutral's radial velocity component at the point of the PUI's origin. Also the neutral's velocity component parallel to the IMF may add an additional drift component to the PUI's velocity.

This causes a dependency of the PUI's initial radial velocity from their point of injection with respect to the interstellar neutral inflow direction [Möbius et al. (2015, 2016)], which is evident from fig. 2 - a sketch of example interstellar neutrals close to 1 AU, where three special cases have been marked. The blue dot marks a direction opposite to the inflow direction. Here, the former ISN's velocity has been nearly parallel to the solar wind velocity. Hence the PUI's radial velocity reaches a local maximum here. In the opposite direction (red spot) the former ISN's velocity is nearly antiparallel to the solar wind (the only non-vanishing velocity-component is radial). So here a local minimum of the radial PUI velocity is found. Lastly, the green spot marks a direction, where the former ISN's radial velocity component vanishes. Here the tangential velocity component reaches a local maximum.

### 2.2.3 Local phase space distribution of PUIs

While the foregoing chapter discussed global implications to the PUI velocities on macroscopic scales, this chapter is going to discuss the local PUI velocity distribution function (VDF) on microscopic scales based on the findings of Drews et al. (2013, 2015) and Drews et al. (2016). As a first grasp to this function one may consider, that the VDF needs to represent the PUIs' gyration. During gyration the PUIs' velocity rotates around an axis in velocity space given by the magnetic field lines. Hence all PUI velocities need to be distributed on a torus, which is perpendicular to the local magnetic field (see fig. 3). It is convenient to split a gyrating particle's velocity  $\vec{v}$  into a component parallel ( $\vec{v}_{||}$ ) and perpendicular ( $\vec{v}_{\perp}$ ) to the local magnetic field  $\vec{B}$  (compare fig. 3), so that

$$\vec{v} = \vec{v}_{||} + \vec{v}_{\perp} \quad (4)$$

applies [e.g. Tsurutani and Lakhina (1997)]. A particle distributed on an ideal torus in phase space has the same  $\vec{v}_{||}$  and  $\vec{v}_{\perp}$  as other particles on the same torus. It is therefore convenient to define the pitch angle  $\alpha$  (compare fig. 3 (right)), which is the angle between a particle's total velocity and its field-parallel velocity component.  $\vec{v}$ ,  $\vec{v}_{\perp}$  and  $\vec{v}_{||}$  form a rectangular triangle and we obtain

$$\sin(\alpha) = \frac{|\vec{v}_{\perp}|}{|\vec{v}|} \text{ or } \tan(\alpha) = \frac{|\vec{v}_{\perp}|}{|\vec{v}_{||}|} \text{ [Tsurutani and Lakhina (1997)]}. \quad (5)$$

Since all particles distributed on the same torus also possess the same pitch angle, we will generally reference to torus distributions by their pitch angle. This means, that when a torus with a pitch angle of e.g.  $120^\circ$  pitch angle referred to, a VDF is meant, where all particles are found with a pitch angle of  $120^\circ$ .

So the velocity space distribution of freshly created PUIs is believed to be a torus distribution. Nevertheless, PUI measurements mostly contain PUI velocities distributed on isotropic shells in velocity space. This gives rise to the question, which processes in the solar wind change the PUI VDF into an isotropic shell.

We will discuss these effects with focus on the timescale, that they happen on. At first the slowest timescale is considered. On a global scale the PUI VDF is affected by the large scale change of the interplanetary magnetic field during its outward transport by the solar wind. Assuming an ideal Parker spiral as a magnetic field configuration, there are two things to be considered: Since the magnetic field becomes weaker with solar distance, an outward pointing magnetic mirror force (for an introduction into the magnetic mirror the reader may refer to chapter 2.3.1), which causes the PUIs' velocity component parallel to the magnetic field lines to increase. Since magnetic fields can't exert work, this happens to the cost of the PUIs' velocity component perpendicular to the magnetic field lines. Hence the torus decreases in radius and its center wanders on the surface of a shell with a radius given by the PUIs' total velocity [Tsurutani and Lakhina (1997); Drews et al. (2015)].

Additionally the heliospheric magnetic field is curved. When a PUI experiences changes in the magnetic field's direction, which happen slowly compared to the PUI's gyro motion, the gyro orbit will just adapt to the new magnetic field configuration remaining at a gyro-trajectory around the local magnetic field vector. Hence the torus is rotated during large-scale transport in the solar wind. When waves with low frequencies, but high amplitudes hit the particle, the same thing happens [Tsurutani and Lakhina (1997)]. This is depicted in fig. 4.

One needs to keep in mind, that PUIs are injected throughout the heliosphere (with location-dependent ionization rates, that is). So a newly injected torus always mixes with older PUI distributions. Altogether it is imaginable, how the mixing of rotated tori can lead towards a shell-like PUI distribution [Drews et al. (2016)], but there is a caveat toward this idea, which is the fact, that the preferred magnetic field configuration is to be seen in only one hemisphere of the shell (the Parker field introduces an angle of  $0^\circ$  at 0 AU and  $45^\circ$  at 1 AU [Parker (1958)]).

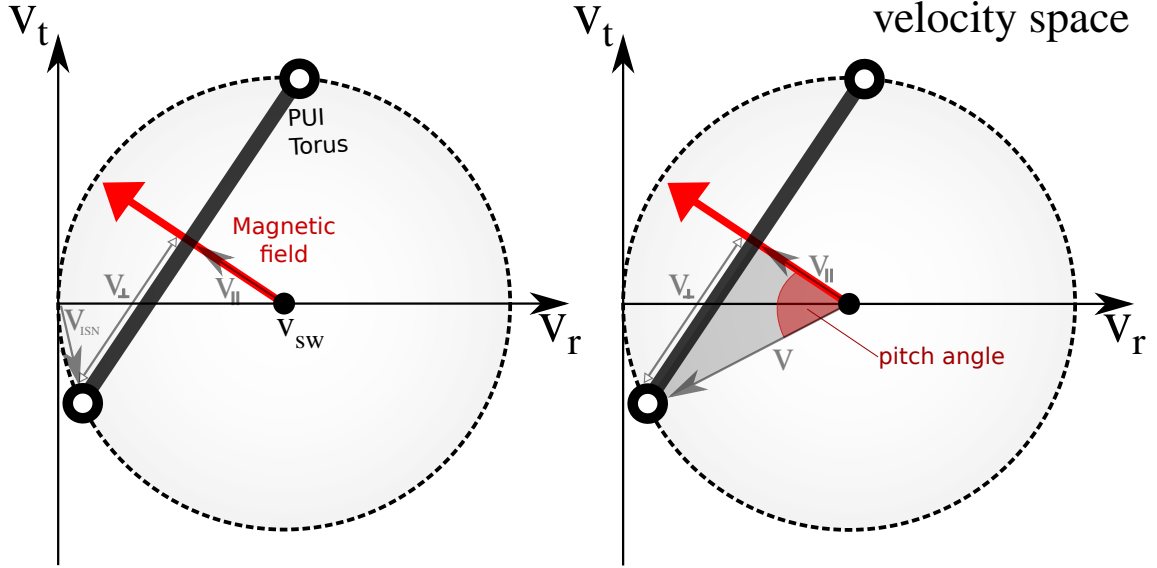


Figure 3: Sketch of the PUI torus as a 2-dimensional projection into the plane of radial and tangential velocity (Where radial means the velocity component in direction of the solar wind's expansion and tangential means the perpendicular velocity component in the in-ecliptic plane. In this coordinate system the normal velocity points out of the ecliptic plane perpendicularly.). An example magnetic field vector can be seen as a red arrow. The torus, which is perpendicular to this field vector intersects the plane in two points depicted by two big dots. Between them the PUI velocities are out of the  $v_r$ - $v_t$ -plane. From the torus' position, size and orientation quantities can be derived. For a freshly created PUI, the torus' orientation and velocity space location is determined by the interstellar neutral's velocity, it originated from. This is depicted as  $v_{ISN}$  in the left figure. Also we see, that the torus' height along the magnetic field is determined by the PUI's velocity component parallel to the local magnetic field  $v_{||}$ . The perpendicular component  $v_{\perp}$  is determined by the torus' radius. Since the PUIs' energy is conserved, the torus will always locate on a spherical shell, whereas the radius of that shell is given by the PUIs' total velocity vector. Also, since the PUIs are carried by the solar wind, the shell centers at the solar wind speed in phase space. The right figure depicts the same situation in order to illustrate the pitch angle's definition, which is the angle between the particle's velocity component parallel to the magnetic field and the particle's total velocity. The figures were inspired by Drews et al. (2016).

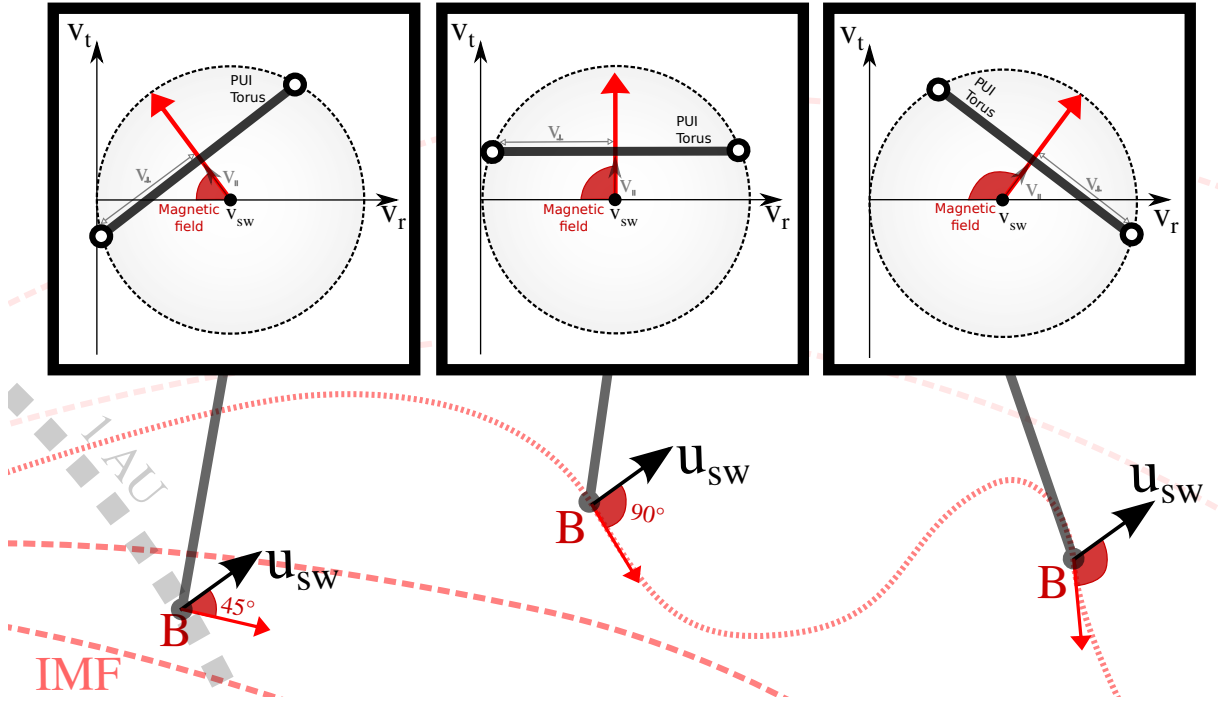


Figure 4: Visualization of the torus' rotation during changes in the heliospheric magnetic field on global scales. The left magnetic field configuration is found at 1 AU, where the ideal Parker field has an angle of  $45^\circ$  with regards to the solar wind velocity vector. In the middle and right configuration we see PUIs transported on another field line, which experiences high amplitude disturbances at low frequencies.

So other processes might be of importance to the PUI VDF.

These necessarily happen on faster timescales, e.g. on a timescale comparable to the PUIs' gyro frequency. This is the time scale of resonant wave-particle-interactions, which happen, when the frequency of the (assumed to be wavelike) disturbance in the magnetic field is resonant to the PUIs' gyro frequency [Tsurutani and Lakhina (1997)]. This may lead to perpendicular or parallel acceleration/deceleration (see top left of fig. 5) or, if the field changes on comparable timescales, but non-resonant to the gyro frequency, towards the torus being curved and distorted as seen in the down left panel of fig. 5.

Finally, on the fastest timescale it is generally believed, that the PUIs' gyro orbit is broken by a field changing much faster than the gyro-frequency. So also the torus is broken, as seen in fig. 5. Interaction with alfvénic waves on this timescale is believed to quickly isotropize the PUI VDF and to be the origin of the PUI shell [Heerikhuisen et al. (2010)]. So numerical simulations of the PUI transport during turbulent conditions may shed light on this process, which is the focus on this work. We will not investigate the PUI transport on global scales.

### 2.3 Disturbances in the IMF and alfvénic turbulence

During the transport of PUIs in the IMF there are several effects, that have an impact on the PUI velocity distribution function and therefore cause systematic changes in the observed PUI velocities as well as their velocities' spatial distribution. While an idealized undisturbed PUI velocity distribution has been discussed in chapter 2.2.3 , this chapter will focus on structures in the solar wind capable of modifying the PUI VDF.

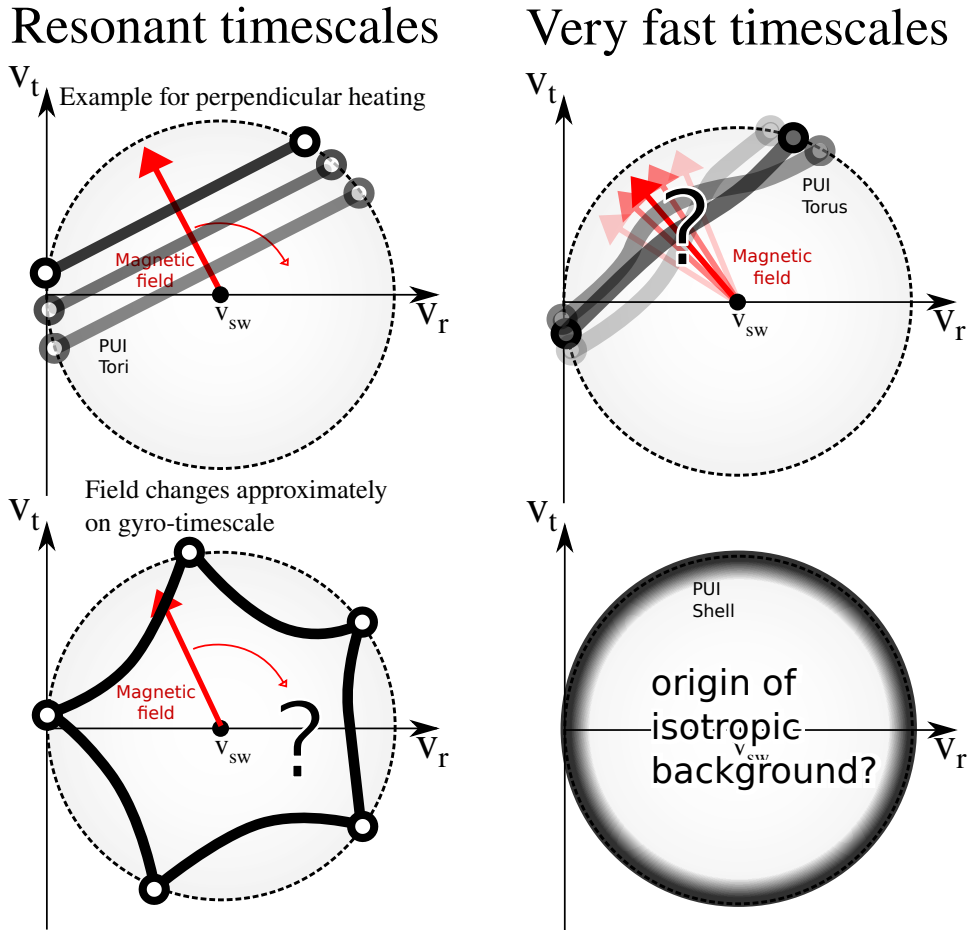


Figure 5: Examples for interactions of the PUI torus with changes of the magnetic field either comparable and resonant to the gyro frequency (left) or much faster than the gyro frequency (right). At the moment there is not enough knowledge to represent these processes in a full and right manner. Hence some of these figures are marked with question marks, since this work is focused on investigating these processes closer. The sketches are inspired by Drews et al. (2016).

---

### 2.3.1 Modification of PUI velocities by the global magnetic field geometry

In the IMF the field strength is generally a function of location (compare chapter 2.1). Therefore a new situation arises, as it can be seen in fig. 6. There a magnetic field configuration is shown, where the field strengthens in one spatial dimension. This causes the field lines to narrow together. Hence along the gyro orbit of the particles the field lines point towards a central magnetic field line, which causes the Lorentz force (always perpendicular to the magnetic field) to point inwards and gives rise to a net force pointing in direction of decreasing magnetic field strength. This force is called the magnetic mirror force [Tsurutani and Lakhina (1997)]. So for a particle moving toward a magnetic field of increasing strength, the particle's parallel velocity is decreasing. If the parallel velocity is small enough, the particle will reverse its parallel motion and be accelerated away from the strengthening magnetic field. Since magnetic fields don't exert work on particles, these changes in parallel velocity happen with cost or gain to the perpendicular velocity component, because the particle's energy is conserved and the particle's pitch angle is modified. We can also explain the modification of the particle's velocity components from the fact, that the magnetic moment  $\mu = E_{\perp}/B$  is conserved as an adiabatic invariant [e.g. Piel (2010)]. Therefore in a decreasing magnetic field the perpendicular energy is decreased. This, at the same time, brings the pitch angle closer to  $0^{\circ}$ . Therefore broad pitch angle distributions are expected to become narrower (or focused), when they experience a weakening magnetic field (like e.g. when transported outward in the IMF, compare chapter 2.1). This is called adiabatic focusing [Prölss (2003); Tsurutani and Lakhina (1997)].

In addition to a longitudinal gradient, which gives rise to the magnetic mirror, a magnetic field may also become weaker in a direction transversal to the magnetic field lines. In such a situation a particle will experience a net force during its gyro orbit, since at a fraction of the orbit the local Lorentz force (proportional to the magnetic field) is stronger, than at the rest of the orbit. When approximating the motion of the particle by the motion of the guiding center of its gyration, a drift velocity of the guiding center is found given by

$$\vec{v}_{drift} = \pm v_{\perp} \cdot r \frac{\vec{B} \times \nabla |\vec{B}|}{|\vec{B}|^2}, \text{ where} \quad (6)$$

$r$  is the radius of the particle's gyro motion around the local magnetic field  $\vec{B}$  and  $v_{\perp}$  is the particle's velocity perpendicular to the local magnetic field.  $\vec{v}_{drift}$  is often referred to as gradient drift velocity and its sign is determined by the particle's sign of charge [e.g. Piel (2010)].

A curvature of the magnetic field gives rise to another modification of the particles' velocity, since in a curved magnetic field the particle experiences a net force [e.g. Piel (2010)]: Along its gyro orbit the particle experiences the centripetal force  $\vec{F} = \hat{e}_R m v_z^2 / R_c$ , where  $\hat{e}_R$  is the unit vector pointing in radial direction (with respect to the curvature) and  $R$  the curvature radius. When averaging the centripetal force over a gyro orbit one obtains the drift velocity

$$\vec{v}_R = \frac{1}{q} \cdot \frac{\vec{F}_c \times \vec{B}}{B^2} = \frac{m v_z^2}{q B^2} \frac{\vec{R}_c \times \vec{B}}{R_c^2}, \text{ where} \quad (7)$$

$\vec{R}_c$  is the vector of the magnetic field's curvature.

### 2.3.2 Large scale disturbances in the IMF

In an idealized model, where the solar wind streams with one constant velocity, the IMF would be shaped like the Parker spiral (see chapter 2.1). Under real conditions, however, the solar wind speed is highly variable. From this discontinuities can emerge [Prölss (2003)]:

Consider two solar wind streams having two different velocities (fig. 7). Since one of the two

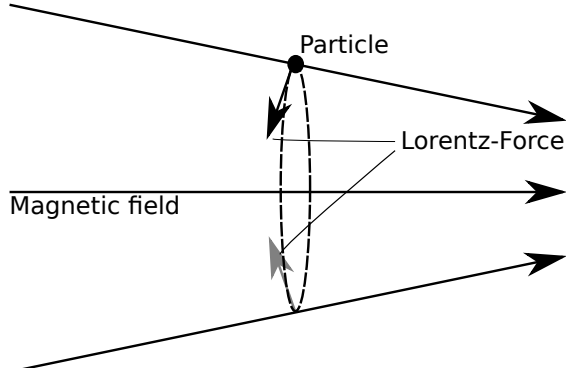


Figure 6: An example configuration to illustrate the magnetic mirror force. Where the magnetic field lines narrow together, it can be seen, that the Lorentz force always points inwards with respect to the gyro trajectory of a charged particle (dashed oval).

streams is slower than the other, the attributed Parker spiral is more curved. So necessarily both spirals will intersect, which in context of the solar wind means, that the plasma streams will interact with each other. To be more precise the faster solar wind stream having a less curved spiral will hit the slower stream. Since the magnetic field is frozen into the solar wind (the solar wind can be considered as ideally conducting, compare chapter 2.1) and magnetic field lines can not cross each other, mixing of both types is impossible. So the slow stream becomes an obstacle for the fast stream and is accelerated. At the same time the fast wind is decelerated until both streams agree to a common speed. Hence the continued stream is neither as fast as the initially faster stream nor as a slow as the initially slower stream.

The solar wind is also streaming at supersonic speed. So the information about the deceleration of the fast stream as well as the acceleration in the slow stream will be passed through shock waves: A forward and a reverse shock. At the point of intersection a compression region is formed. Generally such structures are called streaming interaction regions (SIRs) and if they stay stable over more than one Carrington rotation, they are called co-rotating interaction regions (CIRs). A sketch of a CIR can be seen in fig. 7.

Another effect not included into the idealized model of the solar wind is a coronal mass ejection (CME) [Prölss (2003)]: Mostly during periods of high solar activity the magnetic field of the corona is structured in a chaotic way. Therefore restructuring of the coronal magnetic field is very likely. When it comes to magnetic reconnection, magnetic structures can emerge, which feature a cloud of plasma tossed out of the corona quickly. These plasma clouds often form a huge obstacle for the solar wind as they propagate through the heliosphere and drive shocks in front of them. Inside such a structure cold (with respect to the surrounding solar wind) plasma is found. A large-scale sketch of a CME can be found in fig. 7.

Naturally, these large-scale structures have an effect on the background magnetic field, in which the pickup ions move. However, they are generally not believed to isotropize velocity distributions of gyrating particles. This is a feature most attributed to small scale effects like turbulence in the magnetic field [Heerikhuisen et al. (2010)].

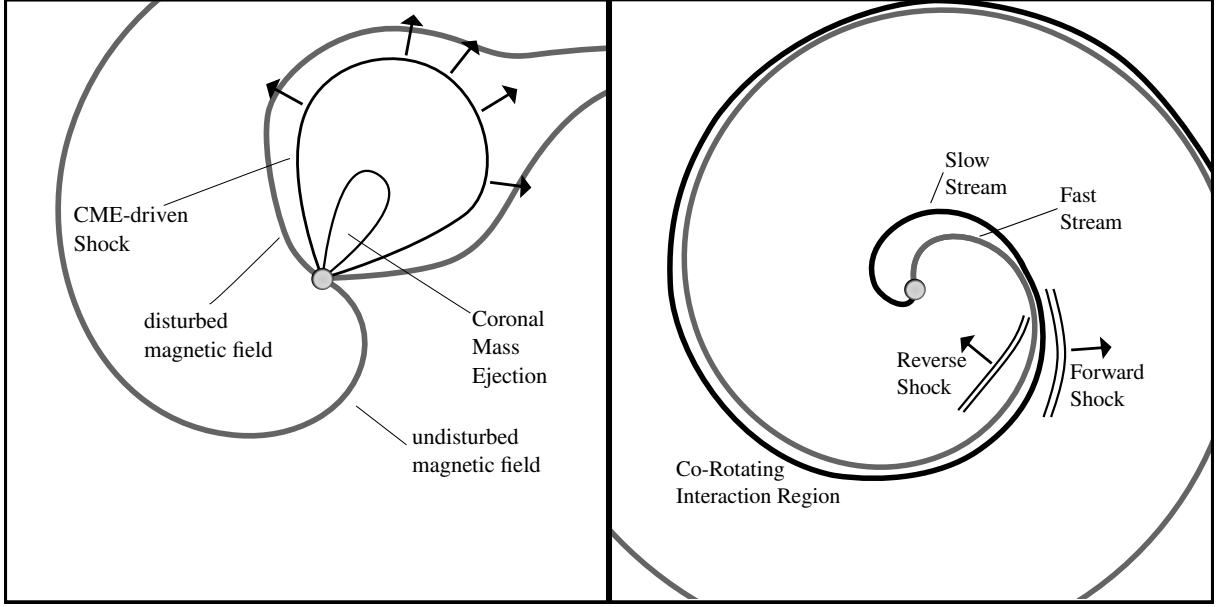


Figure 7: Left: A sketch of a coronal mass ejection (CME). Right: A sketch of a co-rotating interaction region (CIR). Information about CMEs or CIRs can be found in e.g. Prölss (2003).

### 2.3.3 Alfvénic turbulence

More than large scale disturbances small scaled turbulence in the solar wind plays an important role, when it comes to modifying the PUI VDF [Heerikhuisen et al. (2010)]. Generally the solar wind is dominated by a broad spectrum of waves. Since these waves are perturbing a magnetized plasma, these turbulences affect the solar wind plasma as well as the IMF [Tu and Marsch (1995)]. A simple but important type of these waves has first been predicted by Alfvén (1942) and describes a transversal wavelike perturbation of the magnetic field lines correlated with a transversal wave perturbing the solar wind plasma.

Generally a shear alfvénic wave can be described using the magnetohydrodynamic equation of motion as well as the equation of induction [e.g. Piel (2010)], namely

$$\rho_m \frac{\partial \vec{v}_m}{\partial t} = \vec{j} \times \vec{B} \quad (8)$$

$$\frac{\partial \vec{B}}{\partial t} = \nabla \times (\nabla \times \vec{B}). \quad (9)$$

Here  $\rho_m$  is the plasma mass density and  $\vec{v}_m$  the average plasma velocity of all particle species weighted with their respective mass. Using an approach well described in Piel (2010) the magnetic field and velocity is split into a background and a wavelike perturbation with  $\vec{B} = \vec{B}_0 + \vec{B}_1$  and  $\vec{v}_m = \vec{v}_0 + \vec{v}_1$ . It is further assumed, that  $\vec{B}_0 = (0, 0, B_0)$  applies as well as  $\vec{B}_1 = (B_{1x}, 0, 0)$ ,  $\vec{v}_0 = 0$  and  $\vec{v}_1 = (v_{1x}, 0, 0)$ . Using these assumptions as well as a few relations for the vector product the equations above can be transformed into

$$\rho_m \frac{\partial v_{1x}}{\partial t} = \frac{B_0}{\mu_0} \frac{\partial B_{1x}}{\partial z} \quad (10)$$

$$\frac{\partial B_{1x}}{\partial t} = B_0 \frac{\partial v_{1x}}{\partial z}. \quad (11)$$

Combining these one obtains wave equations for  $v_{1x}$  and  $B_{1x}$  given by

$$\left[ \frac{\partial^2}{\partial t^2} - \frac{B_0^2}{\mu_0 \rho_m} \frac{\partial^2}{\partial z^2} \right] \begin{pmatrix} B_{1x} \\ v_{1x} \end{pmatrix} = 0, \text{ which} \quad (12)$$

describes a sinusoidal transversal wave affecting both magnetic field and plasma velocity in a coupled way with the group velocity  $v_A = B_0/(\mu_0 \rho_m)^{1/2}$ , which is known as the alfvénic speed [Piel (2010); Alfvén (1942)]. This simplified approach is a good foundation for the description of alfvénic waves. However, caused by the simplifications the  $y$ -component has not been treated. Generally in the solar wind circularly polarized waves are found [Tsurutani and Lakhina (1997)]. Therefore a sinusoidal  $y$ -component is introduced into the wave field, which is phase shifted by  $\pm\pi/2$  to the  $x$ -component. Assuming  $B_{1x} \propto \sin(\omega t - \vec{k} \cdot \vec{x})$  and  $B_{1y} \propto \sin(\omega t - \vec{k} \cdot \vec{x} + \pi/2) = \cos(\omega t - \vec{k} \cdot \vec{x})$  the absolute value of the circularly polarized oscillating magnetic field vector becomes  $|\vec{B}| \propto (\sin^2(\omega t - \vec{k} \cdot \vec{x}) + \cos^2(\omega t - \vec{k} \cdot \vec{x}))^{1/2} = 1$  and is therefore independent of the location (similar arguments are found for a positive phase shift).  $\nabla \cdot \vec{B} = 0$  is satisfied, when  $k_x = k_y = 0$  applies. This is satisfied intrinsically, since alfvénic waves propagate along the local magnetic field lines (which point in our example in  $z$ -direction).

Altogether the alfvénic wave is a circularly polarized [Tsurutani and Lakhina (1997)] transversal wave perturbing both magnetic field and plasma velocity. Their phase speed is the alfvénic speed [e.g. Piel (2010)]. Generally alfvénic waves are observed at low frequency regimes in the solar wind ( $\omega_{wave} \ll \omega_c$ ), where  $\omega_c$  is the gyro frequency of a typical solar wind ion [Tsurutani and Lakhina (1997)]. Here, the dispersion relation simplifies to  $v_A \approx v_{ph} = \omega/k$  [Tsurutani and Lakhina (1997)]. Also, during alfvénic wave activity the perturbed velocity -and magnetic field components are correlated or anticorrelated. The direction of correlation depends on the direction of wave propagation. In the solar wind outward propagating waves show an anticorrelation and inward propagating waves vice-versa. This leads to the relation

$$\delta \vec{v} = \pm \frac{\delta \vec{B}}{\sqrt{\mu_0 \rho}} \quad (13)$$

between the velocity perturbation amplitude  $\delta \vec{v}$  and the magnetic field perturbation amplitude  $\delta \vec{B}$ . The sign is determined by  $\text{sign}(-\vec{k} \cdot \vec{B}_0)$  [Belcher and Davis (1971)].

From induction the wavelike change in magnetic field and plasma velocity leads to an oscillating electric field given by  $\vec{E} = -\vec{u} \times \vec{B}$  [Tu and Marsch (1995)].

### 2.3.4 Alfvénic cyclotron waves

The approach to the alfvénic waves provided in chapter 2.3.3 is restricted to  $\omega_{wave} \ll \omega_c$ , which comes from the fact, that at time scales similar to the ion gyro frequency the MHD must be replaced by kinetic theory [Stix (1992)]. However, displaying the exact treatment of this theory is beyond the scope of this work and can be found in several textbooks (the interested reader may refer to Baumjohann and Treumann (1997) or Stix (1992)).

At the interesting scales ( $\omega_{wave} \approx \omega_c$ ) the alfvénic turbulence (which is caused by ions in the plasma) is represented by ion cyclotron waves. For these the plasma's refraction index has finite values for frequencies below the ion cyclotron frequency (in the solar wind the proton cyclotron frequency) and reaches a resonance asymptotically for  $\omega_{wave} \rightarrow \omega_c$  [Baumjohann and Treumann (1997)]. The dispersion relation of this kind of waves can be found in Verscharen and Marsch (2011) and is given by

$$\left( \frac{\omega_{wave}}{\omega_{c,p}} \right) = (kl_p)^2 + \frac{1}{2}(kl_p)^4 - \frac{1}{2}(kl_p)^3 \sqrt{(kl_p)^2 + 4}, \text{ where} \quad (14)$$

$l_p$  is a proton's inertial length given by  $l_p = c/\omega_{pp}$  with the proton plasma frequency  $\omega_{pp} = \sqrt{n_p q_p^2 / (\epsilon_0 \cdot m_p)}$ .

Fig. 8 depicts the resulting dispersion relation in comparison to the approximation of  $\omega_{wave} = kv_A$ . The resulting phase velocity  $v_\varphi = \omega_{wave}/k$  is similar to the alfvénic speed for  $\omega_{wave} \ll \omega_c$ , but then becomes smaller than the alfvénic speed for increasing velocities. The increase of the wave vector for increasing frequencies becomes stronger as the frequency reaches the proton

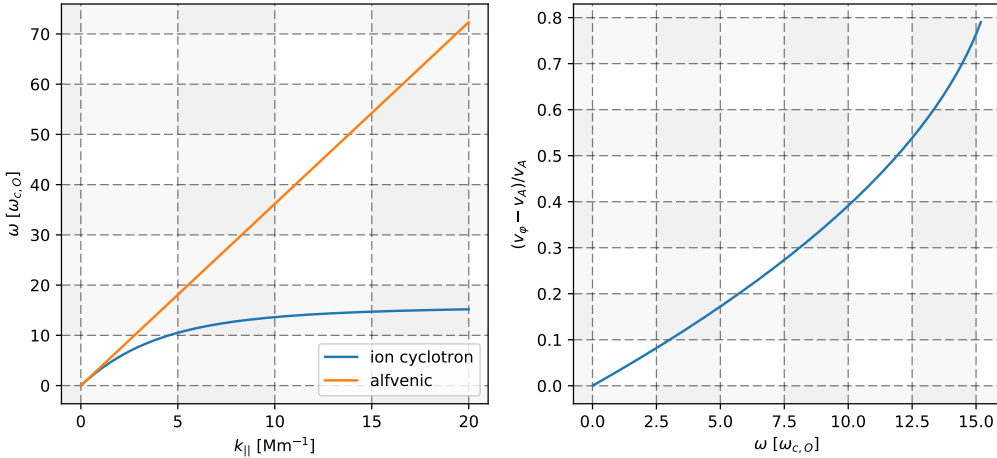


Figure 8: Left: Comparison of the dispersion relation of ion cyclotron waves vs. the simple approach  $\omega = kv_A$  (called alfvénic). It can be seen, that at low frequencies the dispersion relation behaves similar to the simple approach, but diverges from it, as the wave vector (or the frequency, respectively) increases. Right: The absolute difference between phase velocity and alfvénic speed divided by alfvénic speed. As evident from the left panel, the phase velocity is similar to the alfvénic speed at low frequencies, but diverges quickly for increasing frequencies. The frequencies are plotted in units of the oxygen cyclotron frequency, which is approximately 16 times lower than the proton cyclotron frequency. The plots were created assuming a background magnetic field of 5 nT and a proton density of  $10^6 m^{-3}$ .

cyclotron frequency. This also shows, why the approximation of the foregoing chapter of  $v_\varphi \approx v_A$  is only satisfied for  $\omega_{wave} \ll \omega_c$ .

In this work generally ion cyclotron waves are used. Because their dispersion relation varies from the standard alfvénic wave solution, resonances with charged particles may appear at slightly different frequencies. For oxygen ions for instance with a cyclotron frequency much smaller than the proton cyclotron frequency (their mass is approximately sixteen times the proton mass) this effect may only contribute significantly at higher order resonances. To provide an illustrative overview over resonant frequencies fig. 9 shows the resonant wave frequency (in units of the singly-charged oxygen cyclotron frequency) and wave vector to particles distributed on a torus as a function of the torus' pitch angle for example boundary conditions (the background magnetic field is 5 nT, the proton density is  $10^6 m^{-3}$  and the solar wind speed is 450 km/s). Here zeroth-order is not plotted, since it would only appear, when the very delicate condition of  $v_\varphi = v_{||}$  is fulfilled.

## 2.4 Interaction between particles and alfvénic waves

The focus of this work is to investigate interactions between gyrating pickup ions and alfvénic waves. Therefore this section will discuss, how these particles interact with alfvénic waves and especially provide an introduction into the basic physical concepts of resonant wave particle interactions of single particles. Afterwards a brief introduction into the well-established theory of describing wave-particle interactions of particle ensembles through a diffusion approach will be provided.

### 2.4.1 General considerations

Generally, alfvénic waves only exist upon a background magnetic field [Tu and Marsch (1995)]. Therefore the interaction between alfvénic waves and particles is based on the Lorentz-Force

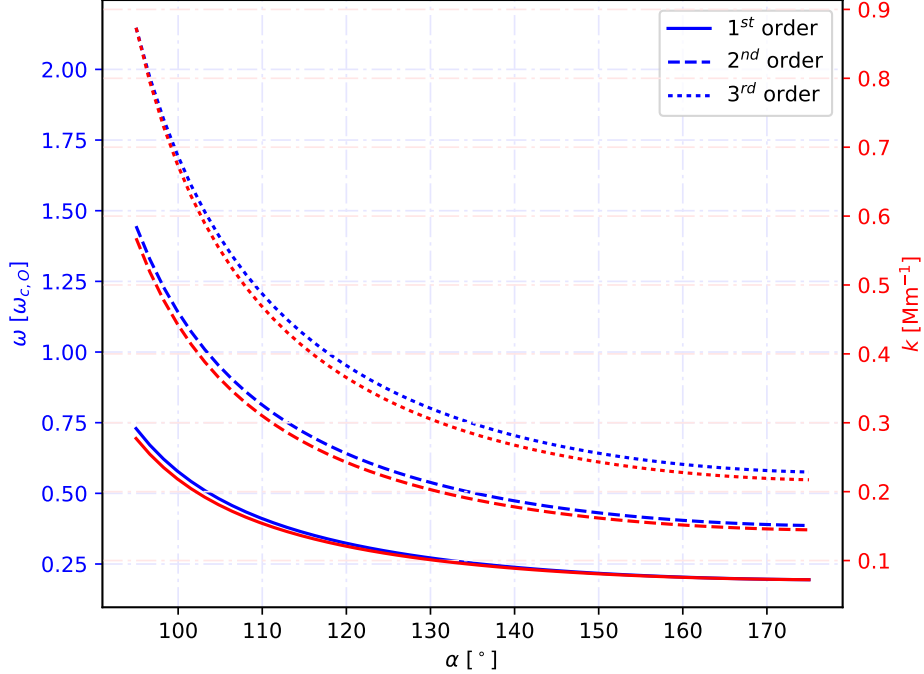


Figure 9: Plot of the wave frequencies (in units of the singly-charged oxygen cyclotron frequency) and wave vectors in first, second and third order resonance to the cyclotron motion of singly-charged oxygen ions as a function of their pitch angle. As boundary conditions to calculate resonances a background magnetic field of 5 nT, a proton density of  $10^6 \text{ m}^{-3}$  and a solar wind velocity of 450 km/s were used.

$\vec{F} = q \cdot \vec{v} \times \vec{B}$ , where  $q$  and  $\vec{v}$  are the particle's charge and velocity and  $\vec{B}$  is the total magnetic field [Tsurutani and Lakhina (1997)]. Superimposed to the magnetic field also a weak electric field  $\vec{E}$  is observed (compare chapter 2.3.3), which introduces the electrical force  $q \cdot \vec{E}$  into the effective force applied to the particle.

But for now only a magnetic field is considered, since the electrical field is a  $\vec{u} \times \vec{B}$ -field with  $\vec{u}$  being the local plasma velocity vector. Because the Lorentz-Force applies perpendicular to the local magnetic field, it is convenient to separate the particle's velocity into a component parallel to the magnetic field and a component perpendicular to the magnetic field with

$$\vec{v} = \vec{v}_{||} + \vec{v}_{\perp}. \quad (15)$$

When a particle moves under the influence of the Lorentz-force, it is tied to circular orbits around the magnetic field. Since these orbits are stable, the centripetal force  $m \cdot |\vec{v}_{\perp}|^2/r$  is in equilibrium with the Lorentz-force, which yields  $m \cdot v_{\perp}^2/r = qv_{\perp}B$ , where the vectors have been replaced by their absolute values.  $v_{\perp}$  is interpreted as the particle's velocity along its gyro-orbit. We see now, that the radius of the particle's orbit is given by

$$r = \frac{m \cdot v_{\perp}}{q \cdot B}, \text{ which} \quad (16)$$

is called the Larmor-Orbit [e.g. Piel (2010)]. With the relation  $\omega \cdot r = v_{\perp}$  we obtain

$$\omega_c := \omega = \frac{q \cdot B}{m}, \text{ which} \quad (17)$$

defines the cyclotron frequency . That is the orbit frequency, of a gyrating particle [e.g. Piel (2010)].

---

So when a particle is injected into a constant magnetic field, the field-perpendicular component of its initial velocity will transform into gyro-orbits around the magnetic field and its field-parallel component will cause the particle's gyro-orbits to translate along the magnetic field lines. Which of both movement types is stronger, can be determined by the pitch angle  $\alpha$ . It is defined as the angle between the particle's total velocity and its field-parallel velocity component.

### 2.4.2 Resonant wave particle interactions

Using the basic concepts covered in chapter 2.3.1 we now investigate the interaction between alfvénic waves and gyrating particles on a basic level, which in approximation only regards a particles' initial velocity. The concepts presented in this section have been well described by Tsurutani and Lakhina (1997) and Lehe et al. (2009).

#### 0<sup>th</sup>-order resonance

As an illustrative example we will consider a particle moving approximately with alfvénic speed, together with an alfvénic wave at cyclotron frequency. Then the particle and the wave will propagate nearly with a constant phase difference towards each other, which means, that the particle will experience a nearly constant magnetic field. This has been sketched in fig. 10. However, because of a slight deviation from the alfvénic speed, the particle will eventually phase shift further from the wave, which causes a slowly emerging variation of the net magnetic field, that the particle will experience. This can be interpreted as a field giving rise to a magnetic mirror force working against the phase shift. Hence, if the particle's velocity is slightly larger than the alfvénic speed, the particle will be slightly decelerated (see fig. 10). If the particle is slower than the alfvénic speed, it will be accelerated, conversely. So the particle's overall velocity parallel to the background magnetic field will be synchronized to the wave. The mirror force works against a difference in alfvénic speed and the particle's parallel velocity. The particle will behave like a wave rider.

It is worth mentioning, that this effect is only expected, when the particle's velocity is deviating only slightly from the alfvénic speed. This is explainable by the magnetic mirror force not being strong enough to compensate large differences in the particle's parallel velocity to the alfvénic speed. When the mirror force can't dampen the difference sufficiently, the particle will not synchronize with the wave.

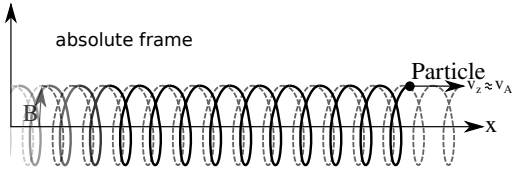
#### n-th order resonance

Considering the 0<sup>th</sup>-order resonance, we saw, that the particle interacts with an alfvénic wave strongly, when it experiences a net Lorentz-force arising from the magnetic field configuration along its gyro-orbit. This means, that the particle needs to sample similar magnetic field configurations periodically in its own frame of reference. Hence the wave frequency, that the particle experiences, must be an integer multiple of the cyclotron frequency. This yields, together with the Doppler-shifted frequency  $\omega_d := \omega_{wave} - \vec{k} \cdot \vec{v}_{||}$ , the resonance condition given by

$$n \omega_c = \omega_{wave} - \vec{k} \cdot \vec{v}_{||}. \quad (18)$$

This also includes the 0<sup>th</sup>-order resonance ( $n \approx 0$ ). There,  $0 = \omega_{wave} - \vec{k} \cdot \vec{v}_{||}$  is obtained, which with  $\omega/k = v_{ph}$  yields  $v_{||} = v_{ph}$ , which we already stated as the condition for 0<sup>th</sup>-order resonance. In the generalized case the particle's parallel velocity at the beginning of the interaction between

without interaction



with interaction

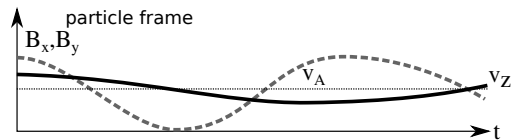
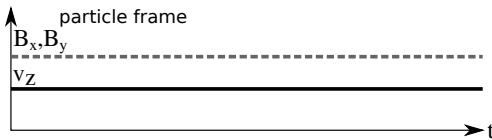
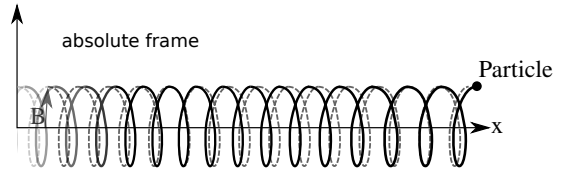


Figure 10: Cartoon of the zeroth-order interaction between a gyrating particle and an alfvénic wave. On the left we see an unrealistic situation without the mirror force, which visualizes, that the magnetic field as seen by the particle is nearly constant in this configuration. On the right we see a more realistic sketch, where the particle's parallel velocity oscillates around the alfvénic speed.

particle and wave can be expressed by

$$v_{||} = v_{ph} - \frac{n\omega_c}{k_{||}}, \text{ which} \quad (19)$$

is obtained from the resonance condition.

To make predictions about, what will happen to the particle during wave activity, we consider, that the particle will gain or lose quanta of energy given by  $\Delta E = \hbar\omega$  together with a change in impulse given by  $m\Delta v_{||} = \Delta p = \hbar k$ . Since  $E = m(v_{\perp}^2 + v_{||}^2)/2$  applies, we obtain  $\Delta E = m(v_{\perp}\Delta v_{\perp} + v_{||}\Delta v_{||})$  from differentiation. Using  $\Delta p$  this transforms to  $m\Delta v_{||}\omega/k = m(v_{\perp}\Delta v_{\perp} + v_{||}\Delta v_{||})$ . By factoring out  $m\Delta v_{||}$  and with  $v_{ph} = \omega/k$  we obtain  $0 = m(v_{\perp}\Delta v_{\perp} + (v_{||} - v_{ph})\Delta v_{||})$ . This can be integrated into

$$\text{const.} = \frac{m}{2} ((v_{||} - v_{ph})^2 + v_{\perp}^2), \text{ which} \quad (20)$$

tells us, that the particle's energy in the wave's frame is conserved. This also gives rise to the fact, that the magnetic mirror force as explanation for interactions between particle and wave is applicable in the wave frame, but not in the laboratory frame. In the laboratory frame one may find equivalent arguments using the wave electric field.

Also the equation includes two kinds of interaction between the particle and the wave: A change in  $|v_{||} - v_{ph}|$  causes an anticorrelated change in  $|v_{\perp}|$ . We see, that a particle's parallel velocity may be increased (parallel acceleration), which happens to the cost of the perpendicular velocity, if the parallel velocity is faster than the phase velocity. Oppositely, an acceleration in the perpendicular component will lower the difference between parallel and phase velocity. One still needs to keep in mind, that the resonance condition is obtained from the particles' initial velocity. Therefore, resonances may change, when the pitch angle is changed dynamically. From fig. 8 by calculating  $v_{\varphi} = \omega/k$  at e.g. the first order resonance of a torus with a pitch angle of 120° a phase velocity in the magnitude of  $\sim 200$  km/s is found, which is in a comparable range to typical solar wind velocities of  $\sim 450$  km/s (compare chapter 2.1). So it is expected, that for the wave particle interactions presented in this study the  $\vec{k} \cdot \vec{v}_{||}$  part of the resonance condition

---

is very relevant, but at the same time subject to dynamic change over time.

### Resonances for different types of charged particles

So far the resonance conditions have been stated without looking at the sign of the particles' and waves' helicities, which shall be covered in this paragraph.

For resonance with a left handed wave the particle's gyro-orbit must be left handed, if the wave overtakes the particle. Conversely, right handed waves interact with right handed particles. This is inversed, when a particle overtakes a wave. Then left handed waves interact with right handed particles and right handed waves with left handed particles.

E.g. a left hand polarized wave can interact with positive ions (which have left handed orbits) by overtaking them or with electrons or negative ions (right handed) by being overtaken. But e.g. a positive ion will not interact resonantly with an alfvénic wave by overtaking it.

#### 2.4.3 Quasi-Linear theory

Quasi-Linear theory seeks to describe the propagation of cosmic rays through the interplanetary magnetic field by diffusion approaches. Instead of the pitch angle  $\alpha$  the pitch angle cosine  $\mu := \cos(\alpha)$  is conveniently used. The resonance condition  $n \cdot \omega_c = \omega - k \cdot v_{\parallel}$  then transforms with  $v_{\parallel} = \cos(\alpha)v$  into  $n \cdot \omega_c = \omega - kv\mu$  [Schlickeiser and Miller (1998)]. Quasi-linear theory has found much agreement with spacecraft observations [e.g. Schlickeiser (1994); Schlickeiser and Miller (1998)]. and therefore is the established theory in the description of cosmic ray propagation. However, it is based upon the basic assumption, that the ratio between wave-inflicted force and Lorentz force caused by the background field is very low, so that it can be neglected in the second order through  $q_L := (\delta F/F_0)^2 \leq 1$  [Schlickeiser (1994)]. As a second assumption it is then generally assumed, that the magnetic field fluctuations only change as a function of the field-parallel coordinates and that the background magnetic field is given by  $\vec{B}_0 = B_0 \hat{e}_z$ , so that the particles' phase space density  $f$  is investigated as a function of the  $z$ -coordinate, the impulse  $p$ , the pitch angle cosine  $\mu$  and the time  $t$  [Schlickeiser (1994); Jokipii (1966); Hasselmann and Wibberenz (1970)]. Quasi-linear theory is then interested in the first-order influences to the particle's motion by the wave field, which is (following the approach by Jokipii (1966)) considered as a random field. It is useful to express the electric and magnetic field trough a Fourier transformation like

$$\vec{E} = \delta \vec{E} = \int d^3 \vec{k} \vec{E}(\vec{k}, t) \exp(i \vec{k} \cdot \vec{x}) \text{ and} \quad (21)$$

$$\vec{B} = \vec{B}_0 + \delta \vec{B} = B_0 \hat{e}_z + \int d^3 \vec{k} \vec{B}(\vec{k}, t) \exp(i \vec{k} \cdot \vec{x}) \text{ [Schlickeiser (1994)]}. \quad (22)$$

Then one may either consider the particles' equation of motion (Lorentz-force) and observe the average squared pitch angle cosine change during a time step  $\Delta t$  (which is the approach presented in Jokipii (1966)) or start with the Vlasov equation [Schlickeiser (1994); Kennel and Engelmann (1966)]. Both approaches give rise to describing the problem through a diffusion equation in pitch angle cosine and  $z$ -space, where the diffusion equation itself is generally of Fokker-Planck-type , which is often referred to as diffusion approximation [Schlickeiser (1994, 1989)]. Therefore the diffusion coefficients  $D_{\mu\mu}$  and  $D_{\parallel\parallel}$  describe the average amount, by which the particles are scattered over time. Jokipii (1966) derived in the case, that the variation of the particle density with  $z$  is negligible, the relation

$$D_{\parallel\parallel} = V^2 \int_{-1}^{+1} \mu_1 \left[ \int^{\mu_1} \frac{(1 - \mu^2)}{D_{\mu\mu}} d\mu \right] d\mu_1, \text{ where} \quad (23)$$

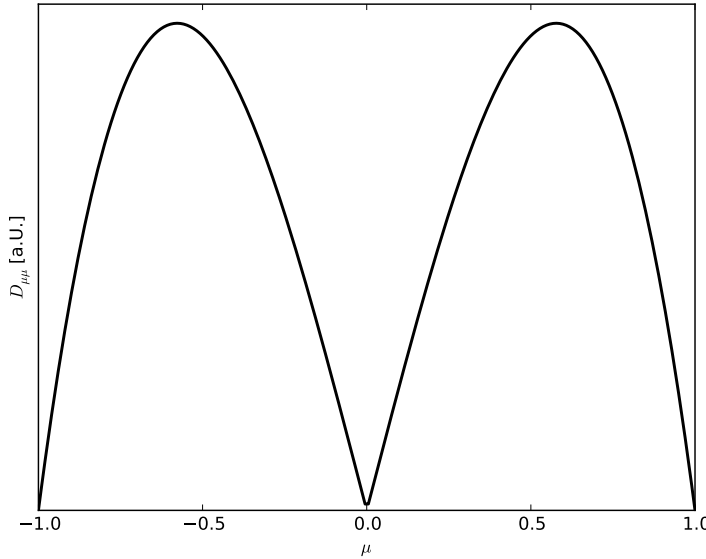


Figure 11: Qualitative curve to illustrate the general approach to the pitch angle diffusion coefficient  $D_{\mu\mu}$  as a function of the pitch angle cosine  $\mu$ . The coefficient has roots at  $\mu \in \{-1, 0, 1\}$ .

the pitch angle cosine diffusion coefficient is defined by

$$D_{\mu\mu} = \frac{\langle (\Delta\mu)^2 \rangle}{\Delta t}. \quad (24)$$

Typical approaches use  $D_{\mu\mu} \propto |\mu|^{q-1}(1-\mu^2)$  with  $q > 1$  [Beeck and Wibberenz (1986)], which reaches zero at  $\mu \in \{-1, 0, +1\}$  meaning, that pitch angle diffusion is least efficient at pitch angles of  $0^\circ$ ,  $90^\circ$  and  $180^\circ$ . Therefore these pitch angles are expected to be points of accumulation, when pitch angle scattering in the diffusion approximation is considered. For reference a qualitative curve is plotted in fig. 11 to illustrate  $D_{\mu\mu}$  as a function of  $\mu$ .

Further modifications of the theory, that treat diverging magnetic background fields, include adiabatic focusing of the pitch angle over the focusing length  $L$  with  $L^{-1} = -B^{-1}(dB/dz)$  have lead to the focused transport (Fokker-Planck) equation [Roelof (1969)]. It is given by

$$\frac{\partial f}{\partial t} + v\mu \frac{\partial f}{\partial z} + \frac{v}{2L}(1-\mu^2)\frac{\partial f}{\partial \mu} = \frac{\partial}{\partial \mu} \left( D_{\mu\mu} \frac{\partial f}{\partial \mu} \right), \text{ where} \quad (25)$$

the  $(1-\mu^2)$ -dependent part of the equation represents the adiabatic focusing [Beeck and Wibberenz (1986)]. Then the mean free path of pitch angle scattering is then given by

$$\lambda_0 = \frac{3v}{8} \int_{-1}^{+1} \frac{(1-\mu^2)^2}{D_{\mu\mu}} d\mu \text{ [Beeck and Wibberenz (1986)]}. \quad (26)$$

## 2.5 Goal of this work

In the foregoing subsections the velocity distribution function of pickup ions and the modification of charged particles' velocities by resonant wave particle interaction has been introduced. It is the goal of this work to investigate qualitatively, how the interaction of pickup ions with alfvénic waves is modifying their velocity distribution function. Especially the distribution of the pickup ions' pitch angle and its modification is of interest, since pitch angle scattering from waves is often assumed to happen swiftly and to be approximable by linear diffusion coefficients (compare

---

chapter 2.4.3). It is furthermore the question, what the key processes are, that perform pitch angle scattering. Therefore numerical simulations of small scale processes during pickup ion transport are conducted, which the next chapter is dedicated to.

---

## 3 Methodology

This chapter will cover the methodology used in this work in order to simulate the PUI transport under turbulent conditions. Especially it will provide an overview over simulation techniques with focus on their application in this work. However, details on the concrete setup of the simulations done in this work will be the concern of chapter 4.

### 3.1 Modeling the particles' motion

It is this work's goal to observe wave particle interactions at the most basic level. Hence it is necessary to simulate the motion of charged particles in electric and magnetic fields. Therefore this first part of the Methodology will explain, which equations describe the motion of the test particles and how these equations were solved numerically.

#### 3.1.1 The PUIs' equations of motion

Pickup Ions (PUIs) in the solar wind are mainly subject to electromagnetic forces, as they are bound to gyrate around the interplanetary magnetic field's (IMF) field lines (compare chapter 2.2). In order to describe their dynamic behavior during transport throughout the heliosphere many models of approximation have been developed. The most popular model is to describe the PUI transport using a diffusion equation (e.g. Isenberg (2005), compare chapter 2.4.3). In addition, the guiding-center model [e.g. Piel (2010)] is often used to describe a charged particle's motion around a magnetic field line. There, the particle's gyro-motion is approximated by a ring-current and the kinetic description of the particle is approximated by a net motion of the ring-current [e.g. Piel (2010)].

This work, however, will use the most basic approach possible, which is the integration of the equation of motion for test particles (We define test particles in the sense of this work as charged particles, that do not influence electric or magnetic fields). Hence the solar wind will be considered as a homogenous background plasma unaffected by pickup ions. This approximation is justifiable, since PUIs are a very small component of the solar wind's particle population [e.g. Kallenbach et al. (2000)].

As commonly known, a charged particle of charge  $q$  and mass  $m$  is subject to an electric force  $q\vec{E}$  caused by an electric field  $\vec{E}$  and to Lorentz-Force  $\vec{v} \times \vec{B}$  due to a magnetic field  $\vec{B}$ . Using Newton's second axiom for resulting forces  $\vec{F} = m d\vec{v}/dt$  and the definition of velocity  $\vec{v} = d\vec{x}/dt$  we find a simple set of equations of motion

$$\frac{d\vec{v}}{dt} = \frac{q}{m} \vec{E} + \vec{v} \times \vec{B} \quad (27)$$

$$\frac{d\vec{x}}{dt} = \vec{v} \quad [\text{Birdsall and Langdon (2004)}]. \quad (28)$$

This set of equations is often called the Lorentz-Newton equations, since Newton's second axiom and the definition of the Lorentz force constitute them [Birdsall and Langdon (2004)].

#### 3.1.2 Time step-Algorithms

The most popular approach to solving equations of motions is to use time step algorithms. Their way of working is explained in this chapter. Extensive information about, how time step algorithms work, can be found in e.g. Birdsall and Langdon (2004) or Bärwolff (2015).

The basic problem of solving the differential equations that describe the particles are the derivatives of location and velocity. In a time step algorithm these are treated by approximation of the differential quotient over time  $t$  with a difference quotient evaluated during a finite time step  $\Delta t$  (hence this is also called the finite difference approach). This means e.g. for the velocity,

that

$$\frac{d\vec{v}}{dt} \approx \frac{\Delta\vec{v}}{\Delta t} = \frac{\vec{v}(t + \Delta t) - \vec{v}(t)}{\Delta t} \quad (29)$$

applies. Since  $d\vec{v}/dt$  can be replaced by the right hand side of the particle's equation of motion the particle's velocity at a time of  $t + \Delta t$  is approximated by the particle's velocity at the time  $t$  by

$$\vec{v}(t + \Delta t) \approx \vec{v}(t) + \left( \frac{q}{m} \vec{E} + \vec{v} \times \vec{B} \right) \cdot \Delta t. \quad (30)$$

Similarly the location is obtained in approximation from  $\vec{x}(t + \Delta t) \approx \vec{x}(t) + \vec{v}(t) \cdot \Delta t$ . Yet, this approach causes an error of the approximated trajectories scaling linearly with the time step  $\Delta t$ .

This linear error is canceled out, when using a central difference quotient to approximate the time derivatives of  $\vec{x}$  and  $\vec{v}$  like e.g.

$$\frac{d\vec{v}}{dt} \approx \frac{\vec{v}(t + \Delta t/2) - \vec{v}(t - \Delta t/2)}{\Delta t}. \quad (31)$$

Since the electric and magnetic fields are generally a function of a particle's location in order to obtain  $\vec{v}(t)$  the quantities  $\vec{x}(t - \Delta t/2)$  and  $\vec{x}(t + \Delta t/2)$  are needed. Therefore the velocity is stored in-between time steps (meaning, that  $\vec{v}(t)$  is evaluated for  $t = t_0 + (n + (1/2))\Delta t$  for  $n \in \mathbb{N}$  and  $t_0$  being the initial time of simulation), while the location is stored on whole time steps ( $t = t_0 + n\Delta t$  for  $n \in \mathbb{N}$ ). This method is called the Leapfrog algorithm and is schematically depicted in fig. 12. The approximation with the central difference quotient introduces an error to the simulation scaling in second order with  $\Delta t$ , which is desirable over a linear scaling, since  $\Delta t$  is generally set to small values.

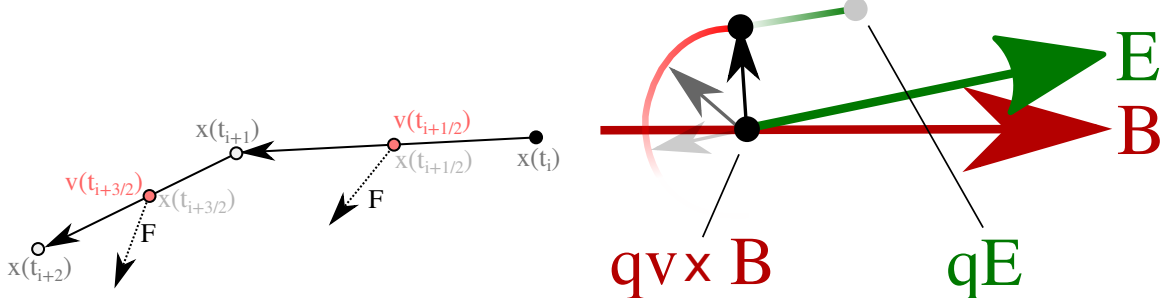


Figure 12: Left: A scheme of how the Leapfrog algorithm is working. The particle locations are stored on integer time steps and the velocities are stored in-between (half way between the time steps of location). So the force is applied to the particle velocities in-between two time steps, but the location is advanced in time from integer time step to integer time step. Right: Decomposition of electric and magnetic force. The electric field (green) accelerates the particle linearly, whereas the magnetic field (red) rotates the particle velocity.

### 3.1.3 Implementation of the Leapfrog algorithm for electric -and Lorentz force

In this work a modified version of the Leapfrog algorithm is used, called the Boris-scheme. To be more specific the approach to integrate the velocity-part of the equations of motion is modified. A detailed description of the Boris-scheme can be found in e.g. Birdsall and Langdon (2004).

The equation of motion for a charged particle in an electric and a magnetic field (compare chapter 3.1.1) consists of the electric force  $q\vec{E}$  and the magnetic force  $q\vec{v} \times \vec{B}$ . Fig. 12 decomposes the effects of both forces. The electric force accelerates a particle in direction of the electric field. The Lorentz force rotates  $\vec{v}$  around  $\vec{B}$ , where the rotation angle is the cyclotron-frequency

---

$\omega_c = eB/m$  times the time step  $\Delta t$ . This is due to the fact, that when only considering the Lorentz force the differential equation

$$\frac{d\vec{v}}{dt} = \frac{q}{m} \vec{v} \times \vec{B} \quad (32)$$

is found, which describes a rotation.

Combining both effects the following scheme is found to obtain the velocity at any time step:

1. Evaluate the electric force and add half of the acceleration caused by the electric force to the particle velocity.
2. Rotate the velocity around the magnetic field by an angle of  $\omega_c \cdot \Delta t$ .
3. Add the other half of the acceleration caused by the electric force to the particle velocity.

In order to ensure invariance of the algorithm under Lorentz-transformation we used a modified version of the Boris-scheme, which is a relativistic generalization. A description of the modified Boris-scheme can also be found in e.g. Birdsall and Langdon (2004).

The modification includes replacing the particle velocity  $\vec{v}$  by  $\vec{u} = \gamma \vec{v}$  in the velocity's equation of motion with  $\gamma^2 = (1 + (|\vec{u}|/c)^2)^{-1}$ . The time step integration of the location then remains unchanged, but during the time step integration of the Lorentz force the rotation angle around the magnetic field is modified by a factor of  $1/\gamma$ . Since  $\vec{u}$  is expected to be small versus the speed of light (typical solar wind velocities are in the magnitude of  $10^5$  m/s, compare chapter 2.1),  $\gamma$  is expected to deviate only slightly from 1.

### 3.1.4 Coupling of field -and particle equations

To this point the treatment of the particle equations has been looked upon. However, these equations are governed by electric and magnetic field conditions. That's why this chapter is dedicated to discuss, how the fields have been implemented. To include them into the simulation one might use one of these methods:

- Use a per-time step integration of Maxwell's equations to simulate the field's evolution in location and time alongside the particle's motion, which is the Particle-in-cell-algorithm (PIC) and also includes the simulated particles into the calculation of the fields for a full treatment of Maxwell's equations [Birdsall and Langdon (2004)], which will be further explained in the following paragraphs. But since PUIs are treated as test particles, these parts of Maxwell's equations will be neglected. Furthermore, including turbulent conditions of the solar wind as background conditions of the simulation would mean in the approach of the PIC-algorithm, that alongside the desired PUI simulation a full solar wind simulation would be needed to be conducted, which is beyond the scope of this work.
- An alternative approach is to use a predefined field structure, which has been derived from analytical expressions. No calculations of the fields during the simulation are necessary. However, one needs to ensure, that these fields are physically correct, meaning they need to obey Maxwell's equations. This is the approach, which this work will follow.

So this work will treat PUIs as test particles, which means in contrast to the PIC-algorithm, that they will not influence the background electric and magnetic fields. Still, discussing the PIC-algorithm, which finds self-consistency by including particles into the field equation it integrates, will give insights on how to implement electromagnetic simulations. The following discussion of the PIC-Algorithm is using information from Birdsall and Langdon (2004).

In a run of the full PIC-Algorithm both particles and fields are treated in one computational cycle, whereas the particles are computed on unquantized positions and obey the Lorentz-Newton

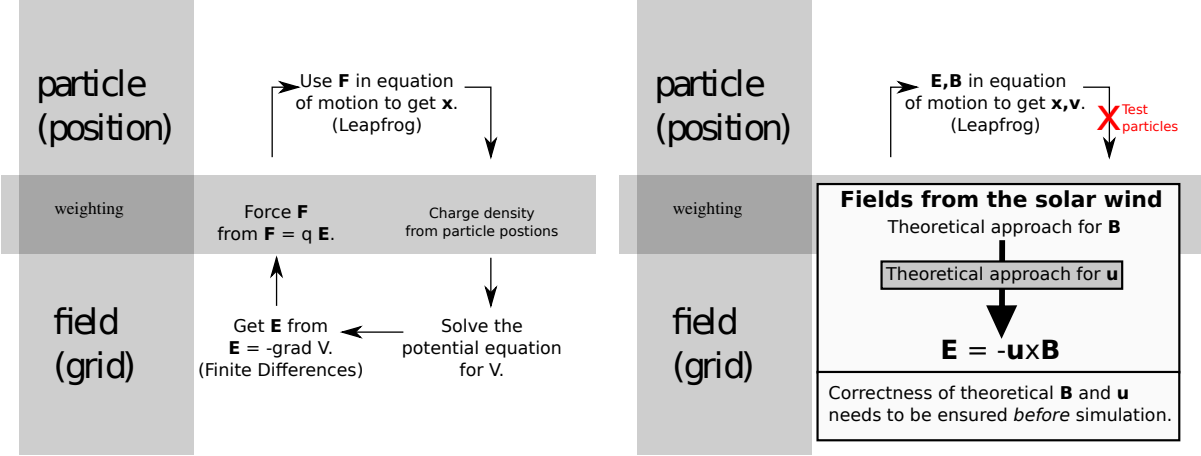


Figure 13: Left: Scheme of a computational cycle of a full PIC (Particle-In-Cell) algorithm. The computation of the magnetic field and the coupling between electric and magnetic field has been left out for simplification. Right: A modified version of this algorithm used in this work using the test particle approach. In the test particle approach the field conditions are uninfluenced by the simulated particles.

equations, which need both the electric and magnetic fields to work. These, however are considered on a quantized grid, which means, that after each computation of the particle-part of the algorithm, the unquantized particle positions need to be translated into charge -and current densities ( $\phi, \vec{j}$ ) stored on a grid. Then the fields can be integrated, whereas the electric field is found from Poisson's law  $\nabla^2\phi = \rho/\epsilon_0$  with the potential obeying  $-\nabla\phi = \vec{E}$ . The magnetic field is then calculated from Ampere's law  $\nabla \times \vec{B} = \mu_0 \cdot \vec{j}$ . Now Ampere's law also contains a second term dropped in the calculation, which is  $\mu_0 \epsilon_0 \partial \vec{E} / \partial t$  and describes together with Faraday's law  $\nabla \times \vec{E} = -\partial \vec{B} / \partial t$  the coupling of magnetic and electric field. Since the fields are stored on a grid, their rotations are readily calculated using a finite difference approach for the partial differentials in  $\nabla$  and one can use the rotation of  $\vec{E}$  for a given time step  $\Delta t$  to approximate the corresponding change of  $\vec{B}$  over time as given by the time derivative of  $\vec{B}$  in Faraday's law. Also, the rotation of  $\vec{B}$  drives a time derivative of  $\vec{E}$ , which means, that these equations can, after the particle-corresponding parts of Maxwell's equations are computed, be integrated with one Leapfrog time step. Afterwards the resulting fields need to be translated to the particle's positions, which is done by weighting the grid points, and the computational cycle of the PIC-Algorithm can start over again. A simplified overview of a computational cycle of the algorithm is given in the left panel of fig. 13.

As mentioned before, this work will not treat particle and field-equations simultaneously. Hence the PIC-algorithm has been modified (see right panel of fig. 13) in order to save computational time: Since PUIs make up a small component of the surrounding solar wind plasma [Kallenbach et al. (2000)], they only make up a little contribution to the generation of fields. Hence the PUIs are treated as test particles, which means, that the background plasma remains unaffected by the PUIs.

So predefined magnetic structures are fed into the simulation as background fields based on analytical expressions found from MHD equations and solar wind measurements. While this approach saves time, the self-consistency of the fields needs to be proven beforehand, since it is not given a-priori by the simulation algorithm. So the next chapter will discuss and motivate the magnetic structures fed into the simulation.

---

## 3.2 Implementation of initial particle and field conditions

Now, that the methods of integrating the observed particles' set of equations of motion are explained, this chapter addresses the magnetic and electric fields affecting these particles and how the particle's kinetic boundary conditions are implemented.

### 3.2.1 Feeding predefined magnetic structures into the simulation

The PUI transport simulation will obtain the simulation's magnetic field each time step from a predefined time-dependent function of the magnetic field. A consistent electric field is then found by defining an analytical background plasma velocity  $\vec{u}$  and applying  $\vec{E} = -\vec{u} \times \vec{B}$ . In addition, the relativistic version of the Boris-scheme (compare chapter 3.1.3) is used to treat the equations of motion, which implies additional electric and magnetic fields, that may arise from a Lorentz transformation into the particle's frame of reference [Birdsall and Langdon (2004)]. But since the particles move much slower than the speed of light, these will probably be negligible. Our approach has the advantage, that in contrast to a full MHD-simulation the fields do not need to be integrated on a grid throughout the whole simulation space. Rather the field conditions only need to be calculated at the particles' positions, which significantly saves computational time.

While this method has the advantage of controllable magnetic conditions it has the caveat, that it has to be made sure before the simulation, that the magnetic fields fulfill Maxwell's equations. Thus the implementation of magnetic fields used in this work will be discussed now.

### Implementation of a transversal alfvénic wave

We model the alfvénic waves with sinusoidal circularly polarized waves superimposed to a constant background magnetic field  $\vec{B}_0$  pointing in  $z$ -direction for simplicity. Since alfvénic waves propagate along magnetic field lines (compare chapter 2.3.3), the wave vector  $\vec{k}$  is therefore also pointing in  $z$ -direction. The alfvénic wave is then modeled by  $\vec{B}_{1x} = \delta B \cdot \hat{e}_x \sin(\vec{k} \cdot \vec{x} - \omega t)$  superimposed to  $\vec{B}_{1y} = \delta B \cdot \hat{e}_y \sin(\vec{k} \cdot \vec{x} - \omega t + \varphi)$  with the phase shift  $\varphi = \pm\pi/2$  between  $x$ -and  $y$ -component of the wave magnetic field (chapter 2.3.3 pointed out, that such an approach models a circularly polarized wave). For visualization, the general field configuration is sketched in fig. 14. The wave frequency  $\omega$  is obtained from the wave vector using the dispersion relation given in 2.3.4. Altogether the total magnetic field is given by

$$\vec{B} = \vec{B}_0 + \delta B \cdot \begin{pmatrix} \sin(\vec{k} \cdot \vec{x} - \omega t) \\ \delta B \hat{e}_y \sin(\vec{k} \cdot \vec{x} - \omega t + \varphi) \\ 0 \end{pmatrix}. \quad (33)$$

The electric field attributed to the alfvénic waves is then derived from induction through  $\vec{E} = -\vec{u} \times \vec{B}$  (compare chapter 2.3.3), where  $\vec{u}$  is a superposition of the solar wind velocity  $\vec{v}_{sw}$  and the velocity fluctuation  $\delta v$  (as defined in equation 13 in chapter 2.3.3). The solar wind velocity is chosen in dependency of the coordinate system, that the simulation works in. E.g. when the simulation computes trajectories in the solar wind bulk system,  $\vec{v}_{sw}$  is equal to the zero vector.

The particles' boundary conditions will be implemented with respect to the background magnetic field. Yet a circularly polarized wave will always have a constant amplitude vector. This means, that during the first time step the particles will be affected by a discontinuous magnetic field, as the boundary conditions can be seen as a previous time step. So just superimposing a circularly polarized wave will have an effect on the particles, which is the same as exposing them to a discontinuous magnetic field. In order to illustrate this, fig. 15 shows the effect of

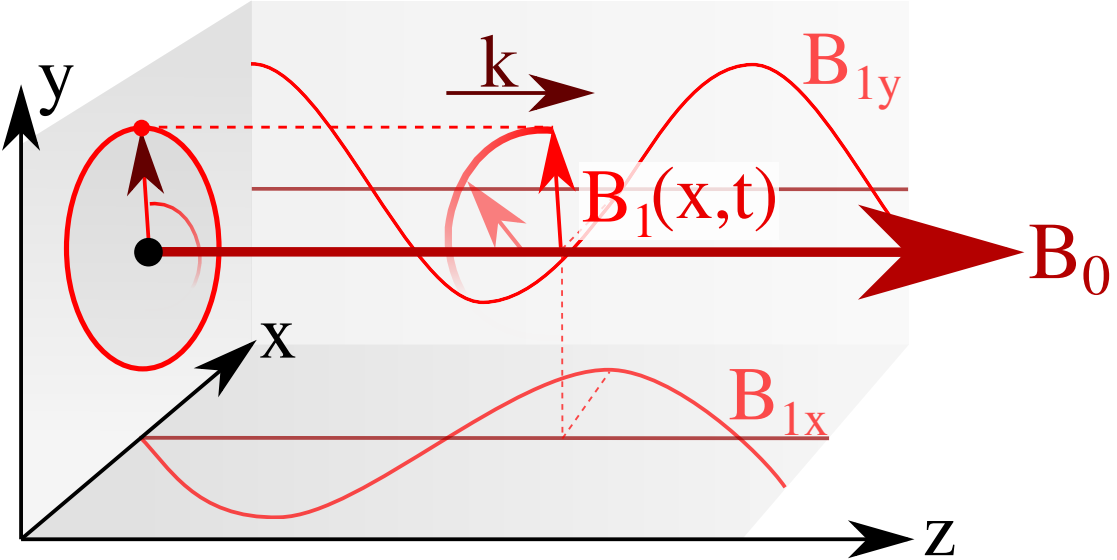


Figure 14: Illustration of the implementation of Alfvénic waves. A circularly polarized wave is achieved by superimposing sinusoidal waves with amplitudes pointing in  $x$ - and  $y$ -direction to each other, where the wave in  $y$ -direction is phase shifted by  $\pm\pi/2$  to the wave in  $x$ -direction. Both waves propagate with a wave vector of  $\vec{k}$  along the background magnetic field, which points in  $z$ -direction.

a discontinuous magnetic field to a torus distribution of particles according to the boundary conditions, that will be provided in chapter 4.1. The magnetic field was consisting of a constant background field pointing with a strength of 5 nT in  $z$ -direction and an additional field being 0 nT strong at the beginning, but pointing with 0.5 nT in  $y$ -direction only at the time step of  $t = 500$  and therefore modeling a delta peak in time. We see, that the brief period of discontinuity has broadened the initial delta peak in pitch angle space into a distribution broadened by  $\sim 1^\circ$ . Evidently a discontinuity of the magnetic field would falsify the results of the simulations.

Hence the circularly polarized wave needs to be faded in. This is however also problematic, since a justified amplitude shape function over time is needed. Also a wave fading in means, that the total magnetic field increases over time, and therefore implies a magnetic mirror force. Speaking in frequency space an amplitude fading in will introduce more frequencies into the frequency spectrum of the magnetic field. Both effects are unwanted when simulating the interaction with continuous waves. That's why the wave is only faded in during a very short time period, so that on the one hand the discontinuity is circumvented and on the other hand the exposition of the particle to the effects of an amplitude fading in is as brief as reasonably possible.

Since waves with an initial phase of 0 will be used in the simulation, one component of the circularly polarized wave will follow a sine-function in its time-dependent behavior, which is 0 at the beginning. The other one will follow a cos-function, which is 1 at the beginning, but 0 at a phase of  $\pi/2$ . So a reasonable time period to fade in the wave is until the wave phase reaches  $\pi/2$ . We use a parabolic amplitude modulation to fade the wave in, because it is within certain boundaries similar in shape to a sine and it approaches its extremum smoothly. With  $\omega$  being the wave's frequency the amplitude modulation function  $A(t)$  is given by

$$A(t) = \begin{cases} 1 - \left(\frac{2\omega t}{\pi} - 1\right)^2 & : t < \frac{\pi}{2\omega} \\ 1 & : t \geq \frac{\pi}{2\omega} \end{cases}. \quad (34)$$

The resulting time dependent behavior of the wave and the modulation function are shown in

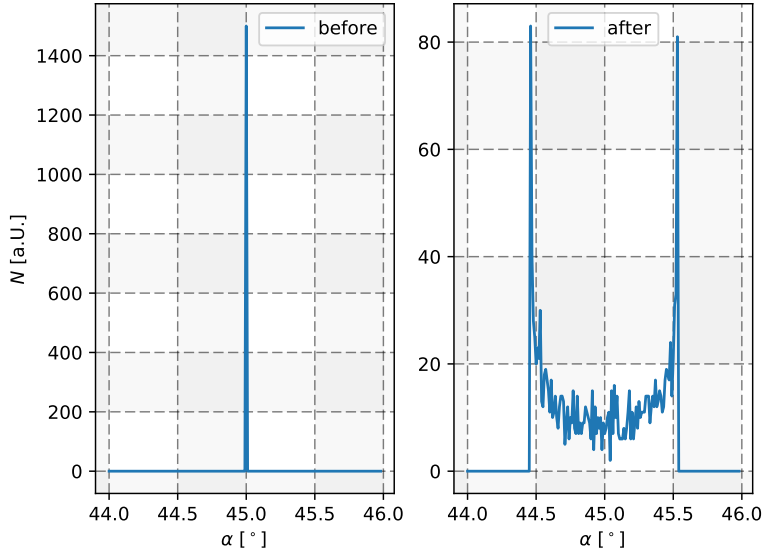


Figure 15: Histograms of the pitch angle distribution of initially torus distributed particles before (left) and after (right) a discontinuous magnetic field has occurred. The discontinuity was modeled with a magnetic field turned on instantly during a time step and then turned off again during the next time step. The discontinuous field has broadened the pitch angle distribution by  $\sim 1^\circ$ .

fig. 16 and was used to obtain consistent boundary conditions for the simulation of waves both continuous in space and time (the results of which are presented in chapter 5.1). Yet, this work also simulated the interaction with intermittent wave activity. The implementation of that is covered in the next chapter.

### 3.2.2 Implementation of intermittent waves

This work investigates, how continuous and how intermittent waves affect pitch angle distributions. For the latter the implementation of continuous waves discussed in the foregoing chapter is modified: Again circularly polarized waves propagating in  $z$ -direction are superimposed to a constant magnetic field pointing in  $z$ -direction, but instead of just adding the wave field  $\vec{B}_1$  to the background field  $\vec{B}_0$  in order to obtain the total field  $\vec{B} = \vec{B}_0 + \vec{B}_1$  a wave amplitude multiplier  $f \in [0, 1]$  is introduced, so that the total field is obtained by  $\vec{B} = \vec{B}_0 + f \cdot \vec{B}_1$  (the electric field is determined in the same way with the same factor). In order to fade waves in or out a symmetric shape function is used, which fulfills the following conditions:

- The function is time-dependent and defined within time values of  $t \in [-a, a]$  with  $a \in \mathbb{R}$  being a measure for the time, that the wave needs to fade in or out.
- At  $t = -a$  and  $t = a$  the function returns zero.
- At  $t = 0$  the function has reached a local maximum at a function value of 1. Within the interval  $t \in [-a, a]$  this maximum is also an absolute maximum.

This work uses two different functions  $f_1$  and  $f_2$  to convolve the waves. They are given by

$$f_1 : [-a, a] \rightarrow [0, 1], t \mapsto f_1(t) = 1 - \left(\frac{x}{a}\right)^2 \quad \text{and} \quad (35)$$

$$f_2 : [-a, a] \rightarrow [0, 1], t \mapsto f_2(t) = \left(1 - \left(\frac{x}{a}\right)^2\right)^2. \quad (36)$$

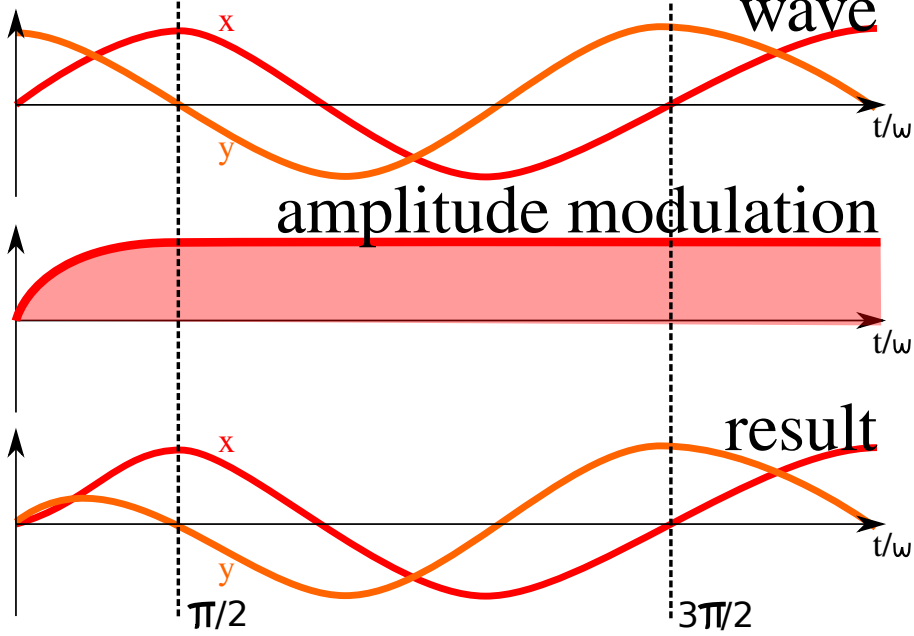


Figure 16: The time dependent behavior of the two components of the circularly polarized wave is sketched in the top panel. In the mid panel we see a parabolic shape function used to fade the wave in. In the bottom panel we see the resulting oscillation.

Both functions are plotted in fig. 17. In order to simulate wave packages passing through the simulation algorithm will use these functions to fade the waves in or out by random.

This is done by distinguishing between four states: wave is turned off, wave is turned on, wave is fading in and wave is fading out. Unless expressed explicitly otherwise the simulations will start with a wave turned off, so that consistent boundary conditions are ensured. The simulation distinguishes between a mean time, that the wave is staying on and off, respectively, which creates a respective probability of starting to fade for both cases. The states of operation are compiled in the following table, where  $f_i$  represents either of the functions  $f_1$  and  $f_2$ . One may also look at fig. 17 for reference.

state	value of $f$	end condition
wave is turned off	$f = 0$	Each time step a random number $\in [0, 1]$ is drawn. If it is smaller than the probability of fading in, the time step is denoted by $t_s$ and the state is changed to fading the wave in. In addition, the wave phase is set to a new random value.
wave is turned on	$f = 1$	Each time step a random number $\in [0, 1]$ is drawn. If it is smaller than the probability of fading out, the time step is denoted by $t_s$ and the state is changed to fading the wave out.
wave is fading in	$f = f_i((t - t_s) - a)$	If $t - t_s \geq a$ is fulfilled, the state changes to wave is turned on.
wave is fading out	$f = f_i(t - t_s)$	If $t - t_s \geq a$ is fulfilled, the state changes to wave is turned off.

The packages only evolve with time and are not location-dependent (in contrast to the

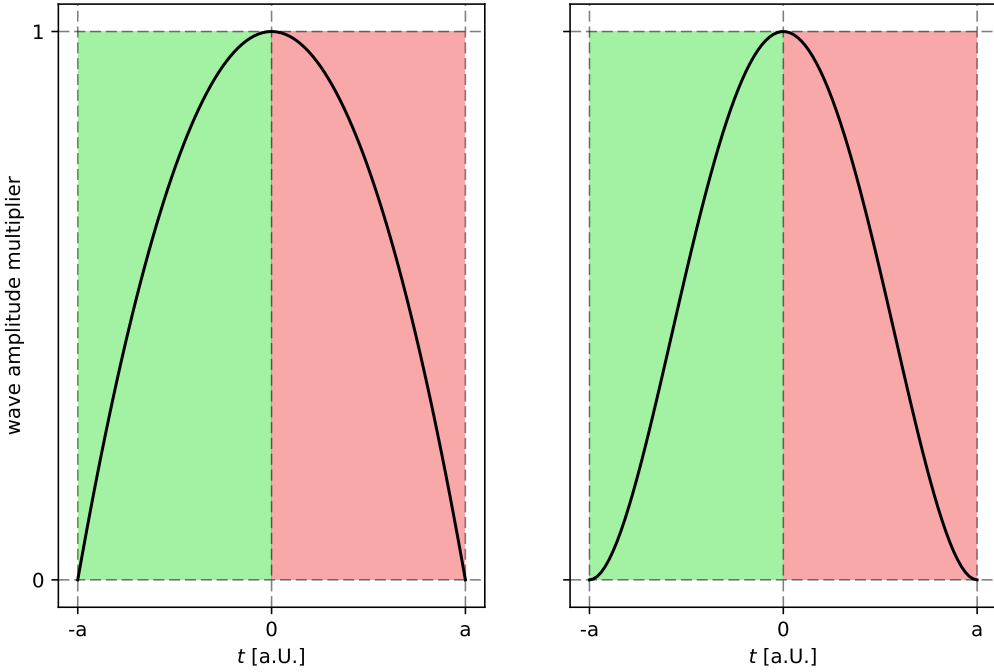


Figure 17: Left: Time evolution of  $f_1$ . Right: Time evolution of  $f_2$ . The green marked areas in time are used to fade the wave in. The red marked areas in time are used to fade the wave out.

implementation of wave shapes used to fade-in the continuous waves at the beginning of a simulation, which is described in the foregoing chapter). So effects arising from a wave front passing through are not simulated here. Yet, this approach grants more control over the actual field, the particles experience, since all particles are affected by the same amplitude factor at the same time, which will be convenient when discussing the results of this work.

### 3.2.3 Implementation of particle boundary conditions

After the detailed introduction into the implementation of the waves and fields this section will cover the implementation of particles or, more specific, how their boundary conditions are set up before simulation.

Generally, the particles are represented at each time step by four individual arrays of equal length (number of elements, not actual length in terms of memory usage), where the particles' mass and charge are stored in one array of float scalars each and the particles' position and velocity are stored in arrays of 3-vectors. Each particle has a number assigned to it, which is the array index, where the particle's respective quantities are to be found. This means for example, when the simulation contains a singly-charged oxygen-ion with the number 0, then the zeroth entry of the mass array is 16 u and the zeroth entry of the charge array has the value of one elementary charge.

We now want to take a look at how these arrays are filled with initial values, before the simulation runs.

The test particles are distributed on a torus in velocity space, so in the following an algorithm is described, which samples these particles. The algorithm needs a given particle position (which is always set to  $(0, 0, 0)$  if not explicitly described differently) a mass  $m$  and a charge  $q$  (particles of the same species are sampled from one run of the algorithm), the interstellar neutral velocity  $\vec{v}_{ISN}$  as a 3-vector and the solar wind speed  $v_{SW}$  and the local background magnetic field  $B$  as

---

scalar values together with the angle between solar wind and magnetic field vector  $\alpha$ . As a first step the 3-vectors of solar wind speed and magnetic field are obtained. For this the  $z$ -component is preliminarily assumed to model the radial direction with respect to the Sun, which means, that the vector describing the solar wind speed  $\vec{v}_{sw}$  consists only of a  $z$ -component equal to  $v_{sw}$ . Then  $\vec{B}$  is derived from the given angle via  $\vec{B} = B \cdot (-\vec{e}_x \sin(\alpha) + \vec{e}_z \cos(\alpha))$ . The resulting coordinate system can be seen in the left panel of fig. 19.

Now for any particle to be created the following three steps are gone through in order to obtain its velocity. These are depicted in fig. 18.

- **Translation to the solar wind system**

When the former neutral particle is picked up by the solar wind, it is inconvenient to describe the PUI's velocity in the resting frame with respect to the Sun (compare chapter 2.2). It is better to look at it in a system moving together with the solar wind (which is approximately the frame of the center of mass). Hence in the first step, the given particle gets the total velocity of  $\vec{v} = \vec{v}_{ISN} - \vec{v}_{SW}$  assigned to it (left panel of fig. 18).

- **Parallel and perpendicular velocities**

A torus population is best described using velocity components parallel and perpendicular to the background magnetic field. So we project  $\vec{v}$  to the magnetic field vector using the scalar product, which gives us

$$\vec{v}_{||} = \left( \frac{\vec{B}}{|\vec{B}|} \bullet \vec{v} \right) \frac{\vec{B}}{|\vec{B}|} . \quad (37)$$

As a computational note it is noteworthy, that simplifying this expression by transforming the  $1/|\vec{B}|$ -parts to  $1/|\vec{B}|^2$  saves computational time, since the square root in  $1/|\vec{B}|$  doesn't need to be evaluated then.

Now we obtain the perpendicular velocity from  $\vec{v}_{\perp} = \vec{v} - \vec{v}_{||}$ , since  $\vec{v} = \vec{v}_{||} + \vec{v}_{\perp}$  applies (compare chapter 2.2.3).

- **Rotation around the magnetic field vector**

So far only two-dimensional velocities have been obtained, which all point toward the same spot in velocity space. The three-dimensional torus distribution arises from this spot by featuring ions at different phases of their gyro-motion. This is achieved by rotating the obtained perpendicular velocity component by a uniformly distributed random angle around the magnetic field axis as shown in the right panel of fig. 18. (Note, that only this step needs to be repeated for every new particle of the same population. The two foregoing steps always yield the same result for each particle of the same torus distribution.) In conclusion, using the rotational Matrix around the magnetic field vector  $M(\alpha)$  for a random angle  $\alpha$ , the obtained particle velocity is given by

$$\vec{v} = \vec{v}_{||} + M(\alpha)\vec{v}_{\perp} . \quad (38)$$

It is noteworthy, that the whole simulation is considered to run in the solar wind frame of reference.

To simplify the implementation of alfvénic waves the whole coordinate system is rotated after the particle velocities have been derived, so that the background magnetic field, along which the alfvénic waves propagate, points in  $z$ -direction. The resulting coordinate system can be seen in the right panel of fig. 19.

### 3.2.4 Choice of time step

Since the interaction of waves and particles is studied, the choice of an appropriate time step is not only crucial to the simulation's results, because the approximative approach has a certain error coupled to the time step (compare chapter 3.1.2), but also because of the sampling

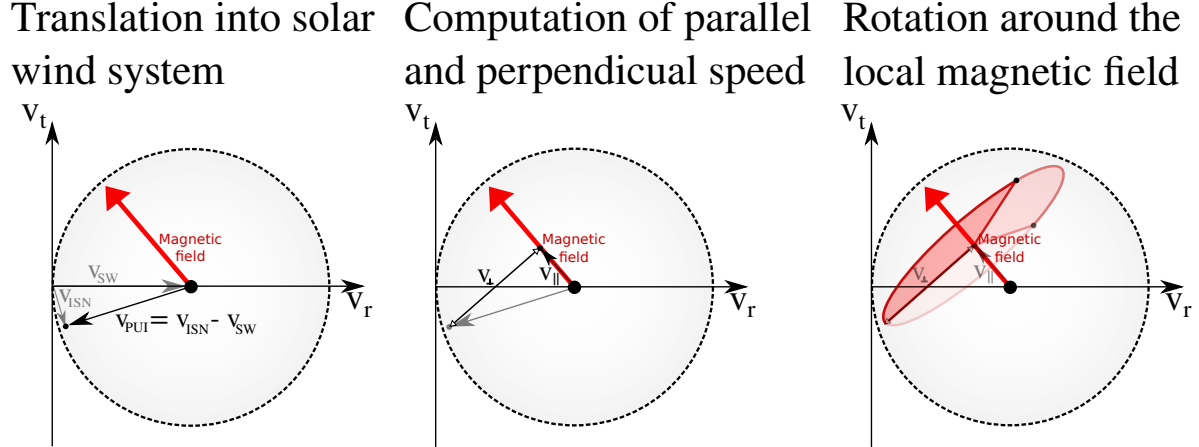


Figure 18: Depiction of the algorithm to sample torus distributed velocities. Its work can be broken down into three steps: Transforming into the solar wind frame (left), obtaining the parallel and perpendicular velocity components (center) and rotating the perpendicular velocity around the local magnetic field vector (right). The interstellar neutral velocity has been exaggerated for the purpose of visualization.

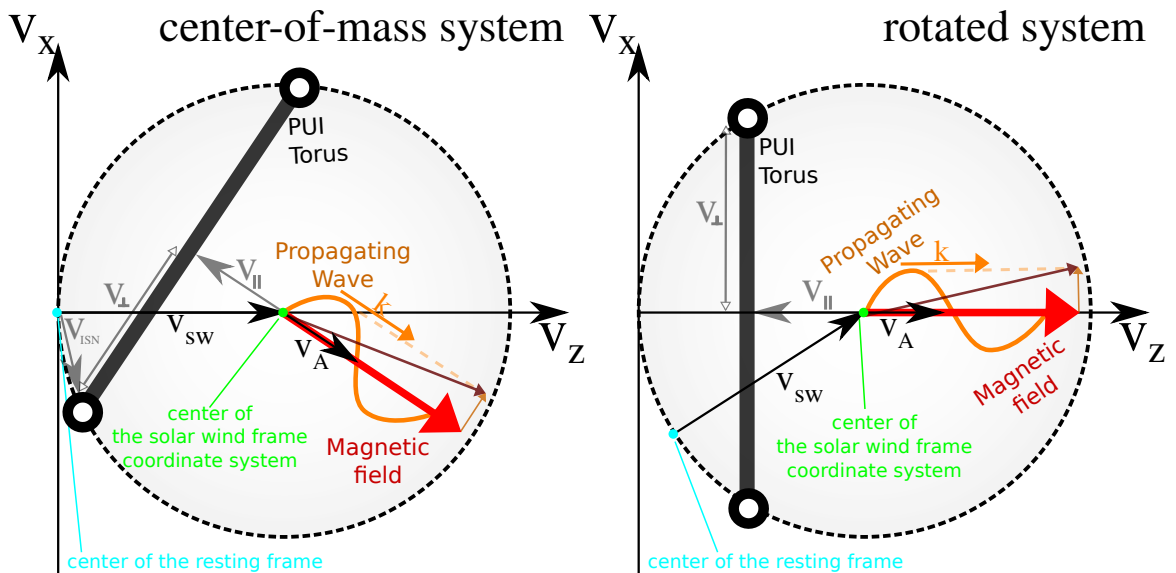


Figure 19: Sketch of an example torus configuration to illustrate the used coordinate systems. The left panel shows the basic configuration in the solar wind frame. The right panel shows the same configuration, but rotated in such a way, that the magnetic field vector points in  $z$ -direction, which is the coordinate system that the simulation uses.

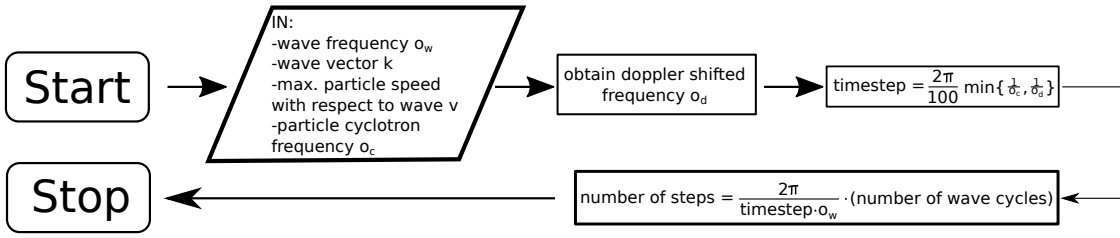


Figure 20: Algorithm to obtain the time step, which samples the waves with the desired precision (at least 100 data points per wave cycle and at least 100 data points per gyro orbit of the test particles). It also shows, how the number of time steps is obtained, when the simulation duration is input in units of wave cycles.

theorem, which states, that when digitizing oscillations into discrete time steps (their distance is given by the reciprocal of the sampling frequency) one can obtain the Nyquist-frequency at maximum, which is half the sampling frequency [e.g. Butz (2013)]. Hence the time step of a simulation featuring waves of a certain amplitude must be conducted with a maximal time step given by the reciprocal of twice the highest wave frequency occurring, in order to resolve these waves.

However, the particles move relatively to the wave, which makes them sample the waves Doppler shifted. This is especially important, when particles move towards the wave sender, which shifts the perceived wave frequencies towards higher values (compare chapter 2.4.2). Thus, if the sampling frequency is at a value sufficient to resolve a wave in a resting frame, this does not guarantee the wave to be resolved sufficiently in the particles' frame.

So altogether a good approach for the choice of time step is to derive the time period of one gyro orbit in the resting frame and (as an estimation) the time period of one wave cycle in the frame of the fastest particle with respect to the wave at the beginning of the simulation. Then one may use the smaller time scale of these and divide it by two to obtain a sampling frequency equal to the Nyquist frequency.

Yet, a time step that large won't be able to cover the detailed changes of motion, that occur during a cycle of the wave (it covers one cycle with only two points). Therefore in this work the time step is chosen in such a way, that at least 100 time steps pass during one particle-sampled wave cycle or gyro orbit (whichever produces the smallest time step). An algorithm has been implemented, which chooses the time step dynamically. It is depicted in fig. 20.

### 3.3 Derivation of the pitch angle

After a run of the simulation the particle's location and velocity are stored as well as the total electric and magnetic fields, the fluctuating components of them and their background components. Using these arrays the pitch angle is derived in the following way:

From fig. 21 we see, that the general definition of the pitch angle is equivalent to the angle between magnetic field and velocity vector (for a definition compare chapter 2.2.3). Hence we denote for the pitch angle  $\alpha = \angle(\vec{v}, \vec{B})$ . Using the scalar product's properties this means, that

$$\alpha = \arccos \left( \frac{\vec{v} \bullet \vec{B}}{|\vec{v}| \cdot |\vec{B}|} \right) \quad (39)$$

applies [Bronštejn et al. (2012)], which only requires the information already given from the simulation. Furthermore the parallel and perpendicular velocities are readily computed via

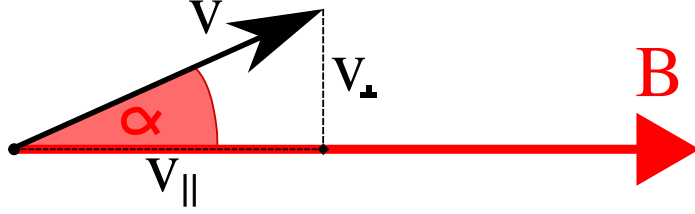


Figure 21: Definition of the pitch angle  $\alpha$ . The particle's total velocity  $\vec{v}$ , the perpendicular velocity  $\vec{v}_\perp$  and the parallel velocity  $\vec{v}_\parallel$  (with respect to the local magnetic field  $\vec{B}$ ) are the edges of a rectangular triangle. The pitch is the angle between the total and the parallel velocity.

$$v_\parallel = |\vec{v}| \cos(\alpha) \text{ and } v_\perp = |\vec{v}| \sin(\alpha).$$

Since the pitch angle is dependent on the local magnetic field the question arises, with respect to which field the pitch angle is best calculated. In this work we consider the pitch angle with respect to the background magnetic field (in the following called  $\alpha$ ) and the pitch angle with respect to the total (wave field plus background field) magnetic field (called  $\alpha^*$  in the following). The quantity  $\alpha^*$  is of special interest, when the magnetic field is changing on very large time scales compared to the particles' gyro motion. On such a time scale the particle will qualitatively react to the total magnetic field (wave plus background) like to a constant background field by remaining at a constant pitch angle to the total field. Such a situation is depicted in fig. 22. While  $\alpha^*$  remains constant,  $\alpha$  oscillates together with the wave. So at low wave frequencies  $\alpha$  is a problematic measure for the pitch angle. However, at very high wave frequencies compared to the particle gyro frequency  $\alpha^*$  will be a problematic measure, because a similar situation to fig. 22 arises: When the particle is not reacting to the wave (meaning  $\alpha$  remains constant), then  $\alpha^*$  will oscillate together with the wave, since the frame of reference, in which  $\alpha^*$  is obtained, is oscillating.

In conclusion both  $\alpha$  and  $\alpha^*$  have to be evaluated with care at certain time scales. Also sometimes the comparison between  $\alpha$  and  $\alpha^*$  is needed, when interpreting pitch angle data. In this work's simulations both are readily available. In real time data only a mixture of both is found, since spacecrafts sample with a limited time resolution. The obtained magnetic field data produces therefore a mixture of  $\alpha$  and  $\alpha^*$ .

However, since it is more intuitive, this work will generally investigate  $\alpha$ , unless explicitly expressed otherwise.

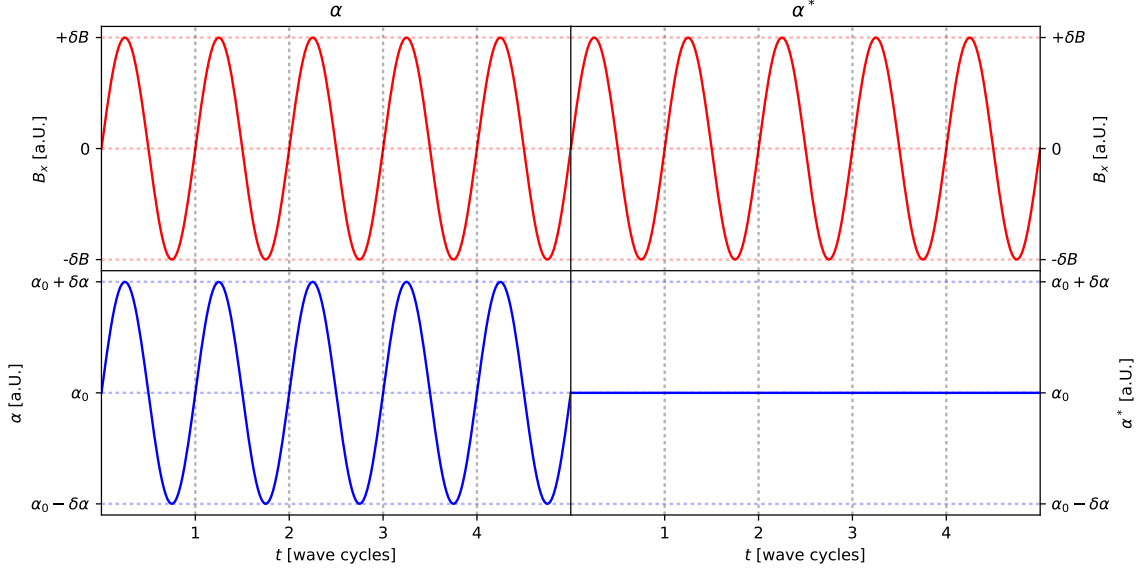


Figure 22: Schematic depiction of a particle reacting to a very slow wave with an amplitude of  $\delta B$ . The top panels depict the  $x$ -component of the total magnetic field. The left bottom panel depicts the pitch angle with respect to the background field and the right bottom panel depicts the time evolution of the pitch angle with respect to the total magnetic field. Since the particle adapts to the slowly moving wave,  $\alpha^*$  remains constant. However,  $\alpha$  shows an oscillation with an amplitude of  $\delta\alpha$  over time.  $\delta\alpha$  will be further discussed in chapter 5.1.4.

## 4 Simulation setup

This chapter will discuss the concrete setup of all relevant simulations done in this work.

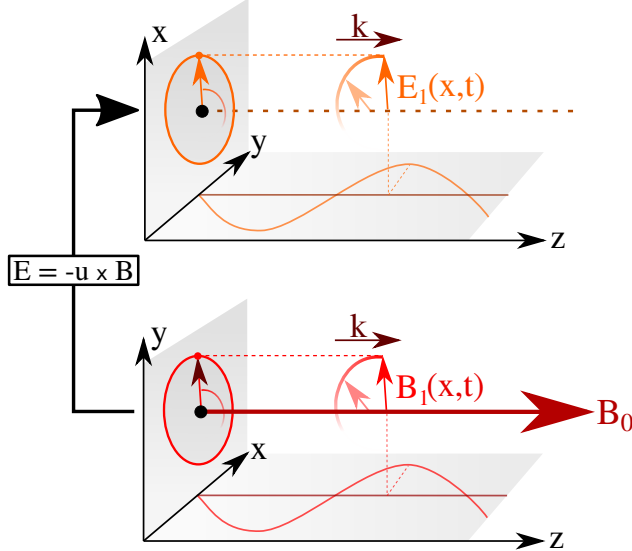
### 4.1 Guidelines

The purpose of this work is to study wave-particle interactions with application to the transport of interstellar PUIs in the solar wind during turbulent conditions at the most basic level. Hence the simulations are conducted with a simplified setup in order to obtain principles of wave-particle interactions unfalsified by effects also observed under real solar wind conditions (like curvature drift in the spiral-shaped magnetic field, non-wavelike density fluctuations and chaotic situations arising from the superposition of waves [Prölss (2003)]).

That's why the main part of these simulations feature the following setup: There is a background magnetic field of 5 nT (if not specified otherwise) pointing in  $z$ -direction with a uniform strength. A circularly polarized alfvénic wave propagating in  $z$ -direction is then introduced into the magnetic (and electric field) configuration as described in chapter 3.2.1. The background electric field is 0. A sketch of the general boundary conditions is provided by fig. 23.

Chapter 5.1 studies the interaction of particles with a continuous alfvénic wave. So all simulations of that chapter were conducted using waves both continuous in time and space, but faded in over the first quarter wave period according to chapter 3.2.1. Chapter 5.2 investigates the interactions with intermittent waves. Therefore the simulations of that chapter feature waves being turned on and off by the methods presented chapter 3.2.2. Chapters 5.2.3, 5.2.4 and 5.2.5 present simulations, where the waves are faded in and out randomly. In the chapters 5.2.1 and 5.2.2 the same method was used to simulate wave intermittency with the modification, the activation or deactivation of the wave did not take place randomly. In chapter 5.2.1 the activation of a wave was investigated and in chapter 5.2.2 the deactivation of a wave was investigated.

## field configuration



## particle configuration

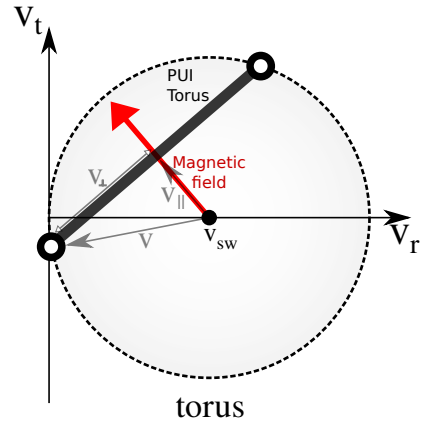


Figure 23: An overview over field -and particle boundary conditions. The left panels show the magnetic field configuration (bottom) and the electric field configuration (top). The magnetic field is a constant background field pointing in  $z$ -direction and a circularly polarized transversal wave. The electric field results from induction. The start conditions for the particles are depicted on the right. At the beginning of a simulation all particles are distributed on a torus in velocity space.

With the exception of chapter 5.2.1 all simulations of chapter 5.2 used the shape function  $f_2$  (compare chapter 3.2.2) to accomplish the fading. Chapter 5.2.1 used shape function  $f_1$ .

In all simulations (with the exception of chapter 5.1.2) the evolution of a torus distribution of singly charged oxygen PUIs (mass: 16 u, charge: one elementary charge) is used for the initial particle conditions. Their initial velocity distribution is generally represented by 500 test particles with velocities sampled according to chapter 3.2.3 (if the number of test particles deviates from that number, it is explicitly noted). In chapter 5.1.2 the particle velocities are set to a constant value described within the chapter.

The background solar wind velocity was set to 450 km/s, which is only of importance, when the boundary conditions are evaluated, since the simulation calculates its results in the solar wind bulk system (compare chapter 3.2.3). The solar wind density was set to  $10^6$  protons per cubic meter. A temperature is not needed for the simulation.

Altogether these boundary conditions yield the following values for alfvénic speed ( $v_A$ ), proton plasma frequency ( $\omega_{p,p}$ ) and singly-charged oxygen ion cyclotron frequency ( $\omega_{c,O}$ ):

- $v_A = 109.060 \frac{\text{km}}{\text{s}}$
- $\omega_{p,p} = 1.317 \text{ ms}^{-1}$
- $\omega_{c,O} = 30.151 \cdot 10^{-3} \text{ s}^{-1}$

## 4.2 Simulation setup ordered by chapter

This section will cover detailed values specific to the simulations conducted ordered by the chapter, their results are presented in. The quantities given in chapter 4.1 serve as guideline values. They will only be mentioned, when they differ from the values presented there.

The simulations of chapter 5.1 were generally conducted using a continuous wave. The following table provides an overview of the simulations conducted in that chapter. The simulations are referenced in order of appearance.

ch	fig	$\alpha_0$	$\omega_w$ [ $\omega_{c,O}$ ]	$\delta B$ [nT]	T	comments
5.1.1	26,27	120°	0.28	0.1	25 wave cycles	Instead of 500 particles four particles of the torus were selected with initial phase differences to the wave of $0,\pi/2,\pi$ and $3\pi/2$ .
5.1.1	28	120°	0.1	0.1	25 wave cycles	Instead of 500 particles four particles of the torus were selected with initial phase differences to the wave of $0,\pi/2,\pi$ and $3\pi/2$ .
5.1.1	29	120°	5	0.1	25 wave cycles	Instead of 500 particles four particles of the torus were selected with initial phase differences to the wave of $0,\pi/2,\pi$ and $3\pi/2$ .
5.1.2	30	-	0.5	$5 \cdot 10^{-4}$	$2 \cdot 10^4$ s	Instead of a torus one test particle was simulated. Its initial velocity is $(100\text{km/s}, 0\text{km/s}, 0.5v_A)$ . Therefore it is in first order resonance to the wave.
5.1.3	31	120°	0.28	0.1	5,25,1000 wave cycles	The three given values of T refer to individual runs of the simulation.
5.1.3	32	120°	0.28	0.1	5 wave cycles	Instead of 500 particles the trajectories of 20 particles were investigated.
5.1.4	33,34	120°	0.001...10	0.1	100 wave cycles	The simulation was run for several frequencies binned logarithmically in the given interval. The frequency interval $[0.01,0.1]$ $\omega_{c,O}$ was swept in 10 steps, the interval $[0.1,1]$ $\omega_{c,O}$ in 120 steps and frequencies out of the interval $[1,10]$ $\omega_{c,O}$ were treated in 20 steps.
5.1.5	36	120°	0.323	$10^{-11} \dots 10^{-2}$	100 wave cycles	The simulation was run for several amplitudes binned logarithmically into 50 steps in the given interval.
5.1.5	37	120°	0.001...10	$0.5, 1 \cdot 10^{-3}, 0.1 \cdot 10^{-3}$	100 wave cycles	The simulation was run for several frequencies binned logarithmically in the given interval. The frequency interval $[0.01,0.1]$ $\omega_{c,O}$ was swept in 10 steps, the interval $[0.1,1]$ $\omega_{c,O}$ in 120 steps and frequencies out of the interval $[1,10]$ $\omega_{c,O}$ were treated in 20 steps. This frequency-sweep was done for the three given amplitudes.
5.1.5	38	120°	0.28	0.001,0.01,0.025,0.05	25 wave cycles	The three given values of $\delta B$ refer to three individual runs of the simulation.
5.1.5	39	120°	0.28	0.0039,0.0045	5 wave cycles	Instead of 500 particles the trajectories of 2 particles were investigated. The two values of the amplitude refer to two separate runs.
5.1.5	40	120°	0.28	0.0039,0.0045	5 wave cycles	Instead of 500 particles the trajectory of 1 particle was investigated. The two values of the amplitude refer to two separate runs. This particular run was not done with the usual simulation algorithm, but conducted with an euler integration of the equations of appendix B.
5.1.5	41	120°	0.28,0.38	0.0045	5 wave cycles	Instead of 500 test particles 1000 test particles were used.

**Key to the table** ch: chapter, fig: figure(s), which show results of the simulation,  $\alpha_0$ : initial pitch angle,  $\omega_w$ : wave frequency,  $\delta B$ : wave amplitude, T: total simulated time

The results of chapter 5.2 featured waves being turned on and off. This was achieved by introducing a global time-dependent weight factor  $f \in [0, 1]$  into the superposition of background  $\vec{B}_0$  and wave fields  $\vec{B}_1$ , so that the total magnetic field is obtained from  $\vec{B} = \vec{B}_0 + f \cdot \vec{B}_1$  (the electric field is obtained in the same way) A detailed introduction into this technique is provided in chapter 3.2.2. An overview of the simulations conducted for chapter 5.2 is compiled in the following table.

ch	fig	$\alpha_0$	$\omega_w [\omega_{c,O}]$	$\delta B$ [nT]	T	$t_{on}$	$t_{off}$	a	comments
5.2.1	43,44,45	120°	0.28	0.1	25	-	-	0,0.25,1, 2,4,8, 12.5,25	The wave amplitude factor is 0 at the beginning and the wave is faded in immediately after the simulation starts. The different values of a refer to individual runs of the simulation.
5.2.2	46,47	120°	0.28	0.1	25	-	-	0, 1,4,8,16	The wave amplitude factor is 1 at the beginning and the wave is faded out after half the simulation time for all $a < 16$ . For $a = 16$ the wave is faded out after one-eighth of the simulation time. The different values of a refer to individual runs of the simulation.
5.2.3 5.2.5	48,49 56	120°	0.28	0.121	5000	5	0.1	1	The waves were activated and deactivated randomly. The simulation started with the waves turned off.
5.2.4	51	120°	0.28	$10^{-4} \dots 5 \cdot 10^{-1}$	5000	5	0.1	1	The waves were activated and deactivated randomly. The simulation started with the waves turned off. The amplitude values refer to 25 logarithmic steps. The different steps in amplitude represent to individual runs of the simulation. Instead of 500 particles each run of the simulation was conducted with 1000 test particles.
5.2.4	52	90°...180° (30 steps)	0.28	0.1	2500	5	0.1	1	The waves were activated and deactivated randomly. The simulation started with the waves turned off. The different steps in pitch angle refer to individual runs of the simulation.
5.2.4	53	120°	0.28	0.1	2500	5	0.1	0.1...32	The waves were activated and deactivated randomly. The simulation started with the waves turned off. The given values for fade times refer to 5 logarithmic steps in the range of 0.1 to 1 and to 10 logarithmic steps in the range of 1 to 32. The different steps in fade time refer to individual runs of the simulation.
5.2.4	54	120°	0.28	0.1	2500	5	0.1	1...32	The waves were activated and deactivated randomly. The simulation started with the waves turned off. The given values of the fade time represent 10 logarithmic steps. The different steps in fade time refer to individual runs of the simulation. In this simulation fade-in and fade-out time are decoupled from each other. So the steps in fade time were once run through to variate fade-in time and once to variate fade-out time. When fade-in time was not varied, it was set to 1 wave cycle. The same applies for fade-out time.
5.2.4	55	120°	3.0...10	0.1	2500	5	0.1	1	The waves were activated and deactivated randomly. The simulation started with the waves turned off. The given frequency values represent 10 logarithmic steps in the range of 0.05 to 0.1, 40 logarithmic steps in the range of 0.1 to 3.0 and 10 logarithmic steps in the range of 3 to 10. The different steps in frequency refer to individual runs of the simulation.

**Key to the table** ch: chapter, fig: figure(s), which show results of the simulation,  $\alpha_0$ : initial pitch angle , $\omega_w$ : wave frequency,  $\delta B$ : wave

amplitude,T: total simulated time (in wave cycles),  $t_{on}$  mean time, that the wave is turned on (in wave cycles),  $t_{off}$  mean time, that the wave is turned off (in wave cycles), a time, that the wave needs to fade in or out (in wave cycles).

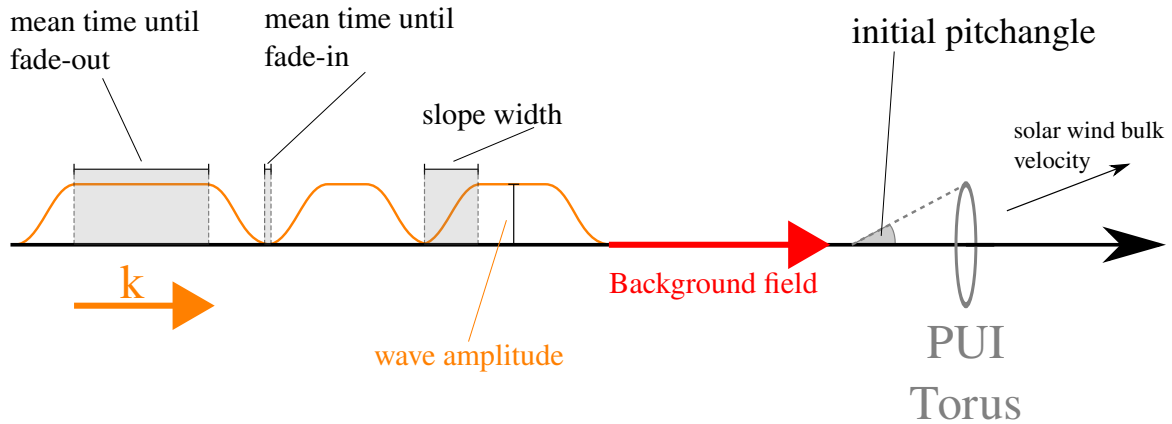


Figure 24: Sketch to provide an illustration of the quantities relevant for this work's simulation of intermittent wave fields. As an example for the intermittent wave fields three wave packages are shown, which propagate with a wave vector of  $\vec{k}$  along the background magnetic field. The wave packages are activated and deactivated by random. The mean time between two wave packages and the mean time that the wave package is active determine this process. A constant slope width determines, how long an activation or deactivation of a wave will take. The waves influence test particles distributed on a torus in velocity space, whereas the initial solar wind velocity and the initial pitch angle of the particles determine the initial velocities. The simulation works in the coordinate system provided by chapter 3.2.3.

In order to illustrate the boundary conditions for our simulations with intermittent waves a sketch of the situation and the relevant quantities is provided in fig. 24.

---

## 5 Results and discussion

In the following the results of the simulation of the interaction between waves and particles are presented in an iterative way: At first the interactions of an oxygen PUI torus with mono frequent continuous alfvén-cyclotron waves are investigated with a focus on the stationarity of this process. That section will then be followed by the results of simulations, which seek to break the stationarity by allowing the wave to turn on and off randomly.

### 5.1 Interactions of oxygen PUIs with a continuous, single frequency wave

This first section of this work's results is focused on exhibiting principles of wave particle interactions at a level, which is as basic as possible: The interactions of a single, continuous and mono frequent wave with a distribution of particles, where initially all particles possess the same pitch angle, namely a torus distribution.

Generally the behavior of the particles (as will be evident from the results provided in chapter 5.1.4) can roughly be divided into three different time scales dependent on the wave's Doppler shifted frequency  $\omega_d$  at the beginning of the simulation : low frequency ( $\omega_d \ll \omega_c$ ), near-resonance ( $\omega_d \approx \omega_c$ ) and high frequency ( $\omega_d \gg \omega_c$ ). Hence in the following the wave's frequency will be given in units of a singly-charged oxygen ion's gyro frequency, which is at a background field of  $B_0 = 5$  nT given by  $\omega_{c,O} = e \cdot B_0 / 16 u = 30.151 \cdot 10^{-3}$  s<sup>-1</sup>.

#### 5.1.1 Trajectories of selected torus particles

As chapter 5.1.4 will show, the effect of a single wave on a whole distribution of particles is complex to understand. Therefore, the exhibition of the wave-particle interactions will start investigating the evolution of single particles in a wave field instead of looking at whole distributions.

Evidently the reaction of a particle to a cyclotron-wave is not only dependent on the particle's parallel and perpendicular velocity (which constitute the pitch angle), but also on where the particle is located on its cyclotron-orbit with respect to the orientation of the wave-elongation. In other words, when the cyclotron orbit of a charged particle is interpreted as an oscillation, the phase difference between particle motion and wave elongation is a controlling parameter, on how the particle reacts to the wave.

In the following the reaction of 4 particles out of a torus of 120° pitch angle to a 0.1 nT wave at a frequency of  $0.28\omega_{c,O}$  (which is in the near-resonance regime) is investigated. The total simulation time is equal to the time needed for 25 wave cycles to pass the particles at their initial velocity. The particles are selected in such a way, that their phase differences are 0,  $\pi/2$ ,  $\pi$  and  $3\pi/2$  as sketched in fig. 25. For further visualization of the dynamic behavior of the particles' velocities the velocity space trajectories of the particles with initial phase differences of 0 and  $\pi/2$  have been animated. The animation can be accessed via the compact disc appended to this work (see appendix F for further information).

Fig. 26 provides an overview of the evolution of the particles' pitch angles over time. All particles exhibit a periodic behavior, at least in the short frame of time, that the simulation covers. That's why chapter 5.1.3 will investigate long-term effects of this wave to the particles, which will result in the conclusion, that the pitch angle's oscillatory behavior remains in fact stationary. So the oscillations shown in fig. 26 are an example for the particles' behavior during continuous wave activity, at least at that wave frequency.

Interestingly the selected particles' oscillations in pitch angle space are qualitatively different from each other. The two top particles perform oscillations at similar frequencies and ampli-

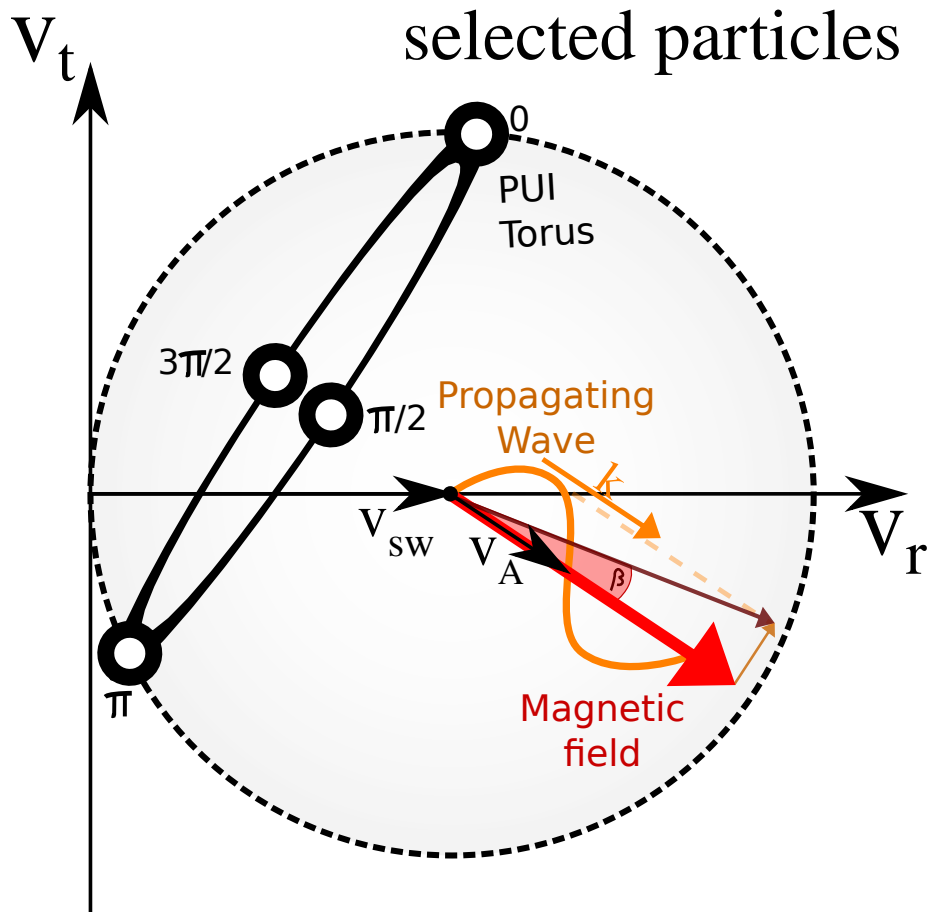


Figure 25: Sketch of the simulation's boundary conditions in velocity space. The particles are initially distributed on a torus distribution. The example torus was sketched perspectively tilted versus the  $(v_t, v_r)$ -layer to display the four selected particles' positions in a better way.  $v_r$  is the radial velocity with respect to the solar wind's expansion, whereas  $v_t$  is tangential to it. The background magnetic field is represented through the red arrow, along which the Alfvénic wave propagates with the wave vector  $\vec{k}$ . Therefore the total magnetic field (dark red arrow) is a superposition of the background field and the wave field.

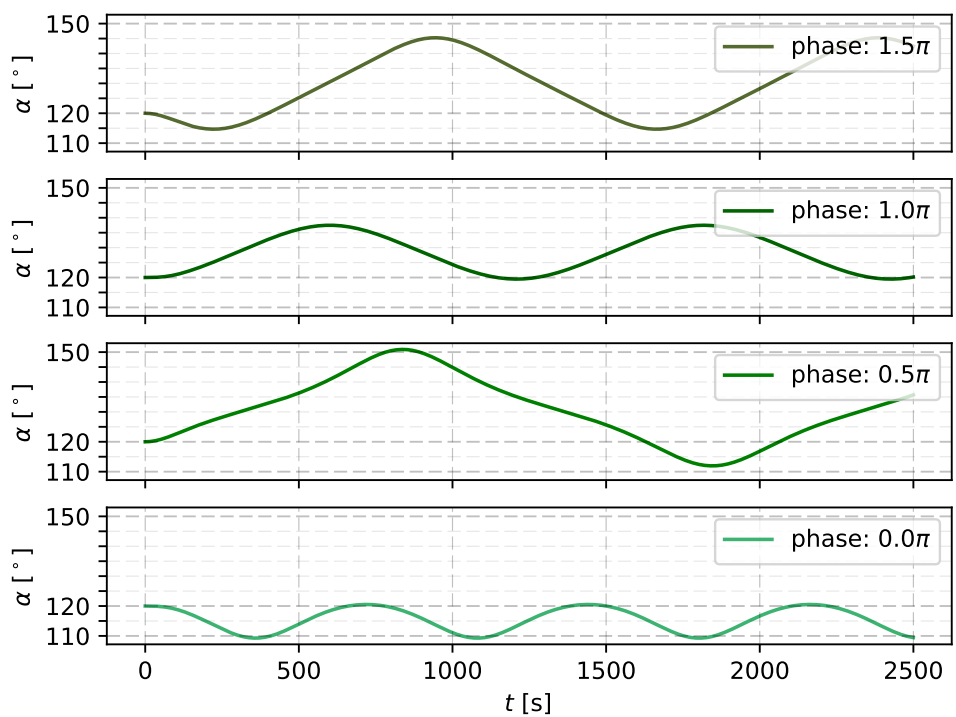


Figure 26: Plot of the time evolution of the pitch angle of four selected particles taken from a torus of 120° initial pitch angle. The labels describe the initial phase difference between the particles' respective gyro motion and the wave. The particles feature an oscillatory behavior dependent on this phase difference.

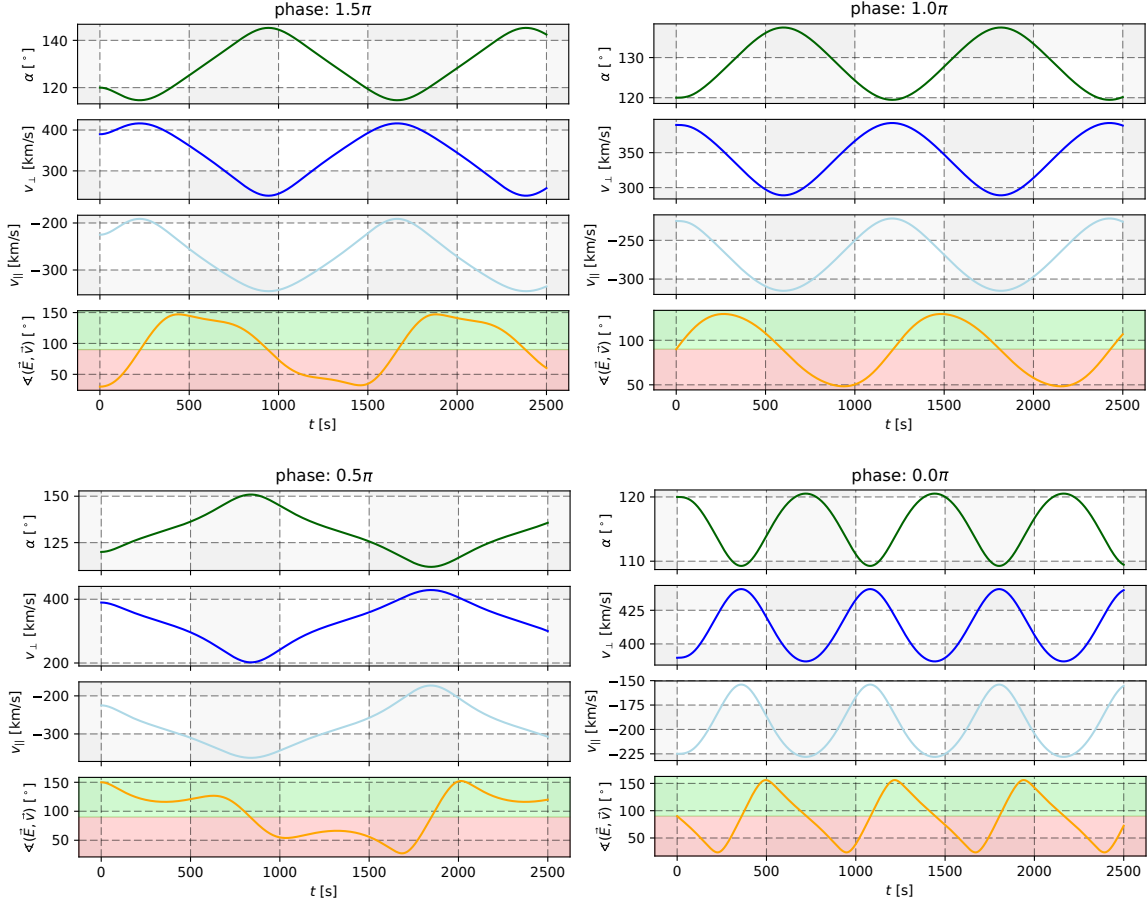


Figure 27: Depiction of the time-evolution of the four particles' (each group of plots represents one particle) pitch angle, perpendicular velocity, parallel velocity and angle between electric field and velocity (from top to bottom). The particles are identified through their initial phase difference to the wave.

tudes, but at the beginning the particle shown in the top panel initially decreases its pitch angle, whereas the particle shown in the second top panel initially increases its pitch angle. This shifts the phase of both oscillations. The  $0.5\pi$ -particle however, has a qualitatively different trajectory in pitch angle space, which is (with an initially increasing pitch angle) rather zig-zag shaped and has the largest amplitude of all shown particles. The bottom particle finally is observed with the smallest oscillation of the shown particles concerning amplitude, but the largest frequency. It performs a sinusoidal oscillation of only several degrees.

We now want to investigate these trajectories further. Therefore in fig. 27 each particle's perpendicular and parallel velocity components are plotted over time as well as the angle between the orientation of the particle's velocity and the wave electric field vector. Since the wave electric field (induced by the magnetic wave) drives the change of the particle's velocity this should reveal, how much the particle's motion is coupled to the wave. By taking a close look the following becomes evident:

Increasing parallel velocities are connected to angles lower than  $90^\circ$  and conversely decreasing parallel velocities are connected to angles larger than  $90^\circ$ . Therefore extrema of the particles' motion are connected to angles of exactly  $90^\circ$ .

The particles with initial phase differences of  $0$  and  $\pi$  both start with angles between electric field and velocity of  $90^\circ$  and perform sinusoidal trajectories. Here the electric field points in a direction perpendicular to a particle's motion, which causes a slow rotation of its velocity.

---

For the other two particles the angle between electric field and particle velocity starts either at a very high or very low value meaning, that the electric force can increase or decrease the perpendicular velocity component directly. This causes in the case of the  $0.5\pi$ -particle an almost linear decrease in perpendicular velocity at first. But since the particle's energy is always conserved in the wave frame, this must increase the difference between wave phase velocity and the particles parallel velocity component. So even though the particle would experience resonant conditions, it changes its parallel velocity, when the perpendicular component is modified, causing the particle to run out of resonance. In the evolution of the angle to the electric field of the  $0.5\pi$ -particle it can be seen, that as the parallel velocity is increased, the wave moves faster with respect to the particle and the electric field angle reaches a local maximum at  $\sim 700$  s before decreasing again. However, afterwards the angle between electric field and velocity is smaller than  $90^\circ$  and the perpendicular velocity is therefore increased. This, in turn increases parallel velocity (in order to diminish the difference between parallel and phase velocity), so that the particle will eventually return to its boundary conditions. The zig-zag shape together with the large amplitude of pitch angle oscillation is obviously triggered by the different angle between velocity and electric field at the beginning. The particle at  $1.5\pi$  shows an oscillation of similar amplitude, but with less zig-zag shaped. It is also evident, that the time-evolution of the angle between electrical field and velocity is qualitatively different for zig-zag-shaped pitch angle trajectories than for sinusoidal trajectories. Instead of swinging between an absolute minimum and an absolute maximum, the angle reaches (e.g. for the  $0.5\pi$ -particle) an absolute maximum, from which it decreases only briefly in order to increase again and arrive at a second local maximum before decreasing below  $90^\circ$ . As fig. 27 shows, this is the general difference between the particle trajectories. We will see later on, when investigating, how the trajectories are influenced by the choice of wave amplitude and frequency, that this follows a general principle.

In conclusion we see, that the particles perform oscillatory trajectories in pitch angle space when exposed to a singular mono frequent wave. Similar results to fig. 27 have been obtained at different wave frequencies, whereas at frequencies close to resonance trajectories, that are similar to deformed sinuses have been found as well as non-deformed sinuses. In the other frequency-regimes, however the qualitative behavior of the trajectories remains sinusoidal. In fig. 28 for example the evolution of four selected particles is shown in analogy to fig. 26, but for a simulation featuring 25 cycles of a  $0.1$  nT wave with a frequency of  $0.1\omega_{c,O}$ . The main qualitative difference between the trajectories is, whether the particles initially increase or decrease their pitch angle, which is clearly due to phase difference to the wave. We also see, that all pitch angle oscillations are at the same frequency in this situation, which is roughly the same as the wave's frequency, since 25 cycles of pitch angle oscillation are seen in fig. 28. This indicates, that at this low frequency the particle samples the perturbed magnetic field as background field. Therefore the particle trajectory is more similar to a cyclotron orbit, but rotating together with the wave-influenced field. This will be evident with the results displayed in chapter 5.1.4.

An example taken from the high-frequency regime is given in fig. 29 featuring the time evolution of particles exposed to a  $0.1$  nT wave of  $5\omega_{c,O}$  frequency. There we see very small high frequent oscillations showing, that the particle is only slightly affected by the wave. Here the time scale of the change in wave elongation is much quicker than the time scale of the particle's velocity change caused by the wave.

Altogether this section has provided a first glance on pitch angle change due to exposition to a continuous wave field. We have seen, that in a wave perturbed magnetic field the pitch angle generally performs oscillations. We have observed when exposing the particles to a wave with a frequency close to the time scale of the particles' gyro motion (fig. 26), that the qualitative shape of these oscillations is dependent of the particles' initial position on the torus, which can be interpreted as the beginning phase of the gyro motion. This effect was not observed,

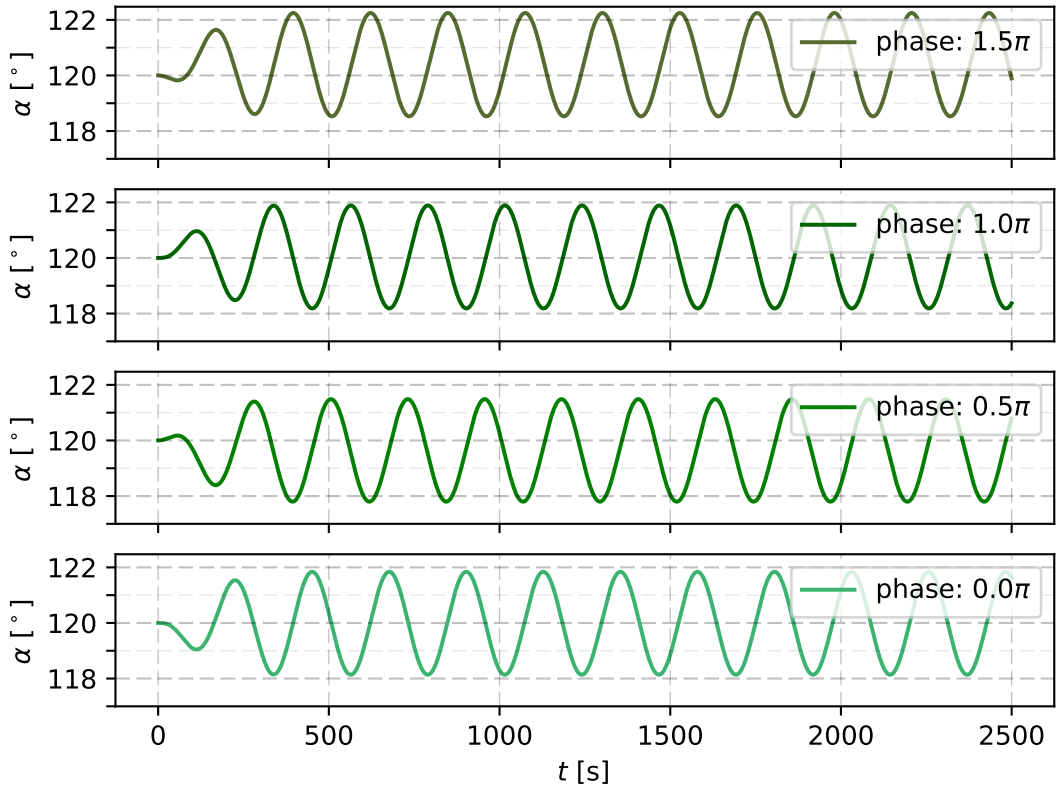


Figure 28: Time evolution of the pitch angle of particles exposed to a wave of  $0.1\omega_{c,O}$  frequency in analogy to fig. 26.

when exposing the particles to waves of lower frequencies (fig. 28) or much higher frequencies (fig. 29). We will see with the studies of the following chapters, that this is due to a general dependency on the initial phase difference between gyro motion and wave elongation, the wave amplitude and the wave frequency compared to the particles' gyro frequency.

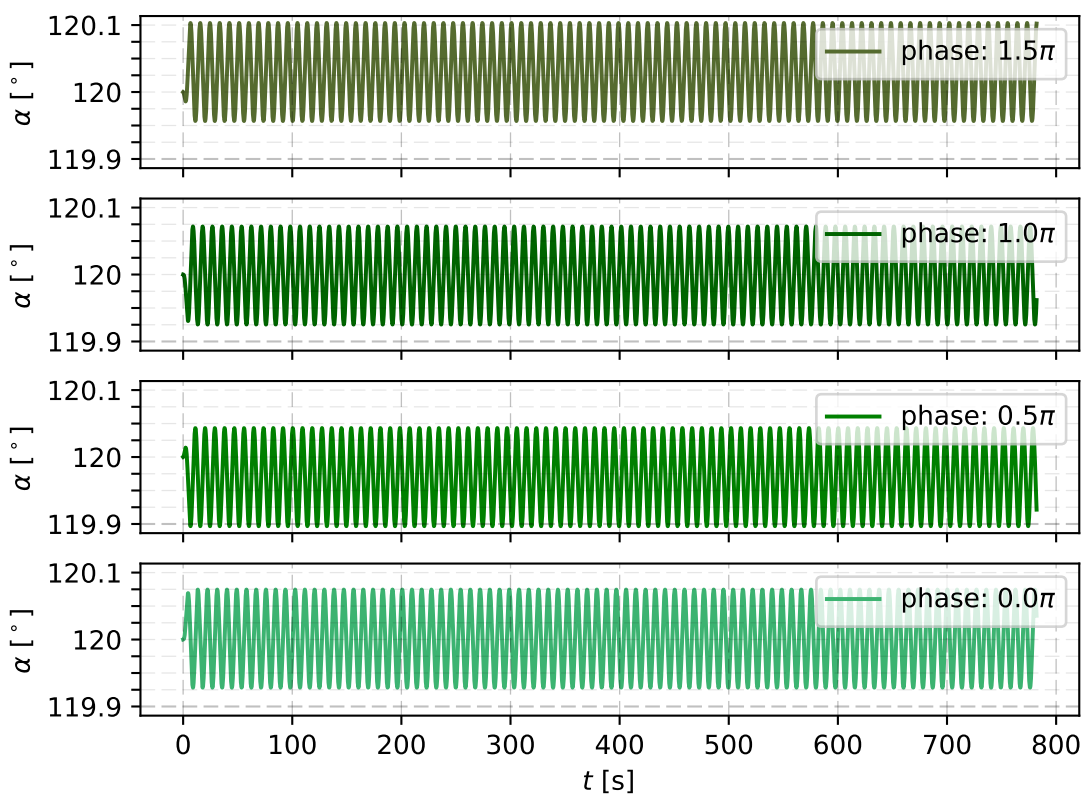


Figure 29: Time evolution of the pitch angle of particles exposed to a wave of  $5.0\omega_{c,O}$  frequency in analogy to fig. 26.

---

### 5.1.2 Study of the case of first-order resonance: perpendicular acceleration -and deceleration

Before taking the results of the last section to the next level by investigating pitch angle distributions instead of single particles' pitch angles, we want to investigate the special case of first order resonance in order to validate the simulation algorithm. Therefore a simulation of a single particle is set up, which has an initial velocity of 100 km/s in  $x$ -direction and a velocity of half alfvénic speed in  $z$ -direction. A continuous alfvénic wave is fed into the simulation with a frequency equal to half the oxygen cyclotron frequency, at which, as chapter 2.3.4 shows, its dispersion relation can be simplified to  $\omega = v_A k$ , which was done for this test simulation. The wave's amplitude is 0.5 pT and the background field is 5 nT pointing in  $z$ -direction, which also is the direction of the alfvénic wave's propagation.

This simple example is constructed in such a way, that first order resonance should arise (compare chapter 2.4.2) causing parallel acceleration or deceleration (depending on the phase difference between wave elongation and particle gyro motion). Therefore the simulation was conducted for an initial wave phase of  $0^\circ$  and  $180^\circ$ . The top plots of fig. 30 (labeled with Dynamic parallel velocity) show the evolution of the particle's pitch angle, perpendicular and parallel velocity. As we see, the particle is at first accelerated (decelerated) in perpendicular velocity only to be at the same time accelerated (decelerated) in the parallel component, which slowly moves the particle out of resonance. Coming out of resonance the particle will eventually sample different phases of the wave, which are connected to reversed angular configurations between particle velocity and wave electric field vector. Therefore the trend in parallel velocity is reverted and the particle is moved into resonance once again. Thus we see an oscillation in pitch angle similar to the observation of the previous chapter.

However, this is contrary to the concepts of chapter 2.4.2, where steady acceleration (deceleration) in the perpendicular component was expected in the resonant case. Actually this prediction was fulfilled in the first  $\sim 2000$  s of the simulation, but since the particle's energy in the wave frame is conserved the particle moves out of resonance. That's why in order to validate the simulation's algorithm in terms of resonance conditions the simulation was conducted once again, but this time with a constraint keeping the parallel velocity constantly at a resonant value. The results of that can be seen in the bottom plots of fig. 30 (labeled with Fixed parallel velocity). There a steady acceleration (deceleration) is shown, which matches the expectations in terms of resonant behavior. Once again we observe, that the phase difference between particle gyro motion and wave elongation controls, whether an increase or a decrease in pitch angle takes place.

With this small study of first order resonance we were able to observe steady perpendicular acceleration or deceleration, when wave and particle were resonant to each other, but only when the parallel velocity was fixed. When changes of the parallel velocity were allowed, the particles move out of resonance quickly. Therefore the interaction of charged particles with a wave field shows nonlinear characteristics, where the qualitative behavior of following time steps is strongly dependent on the previous time step.

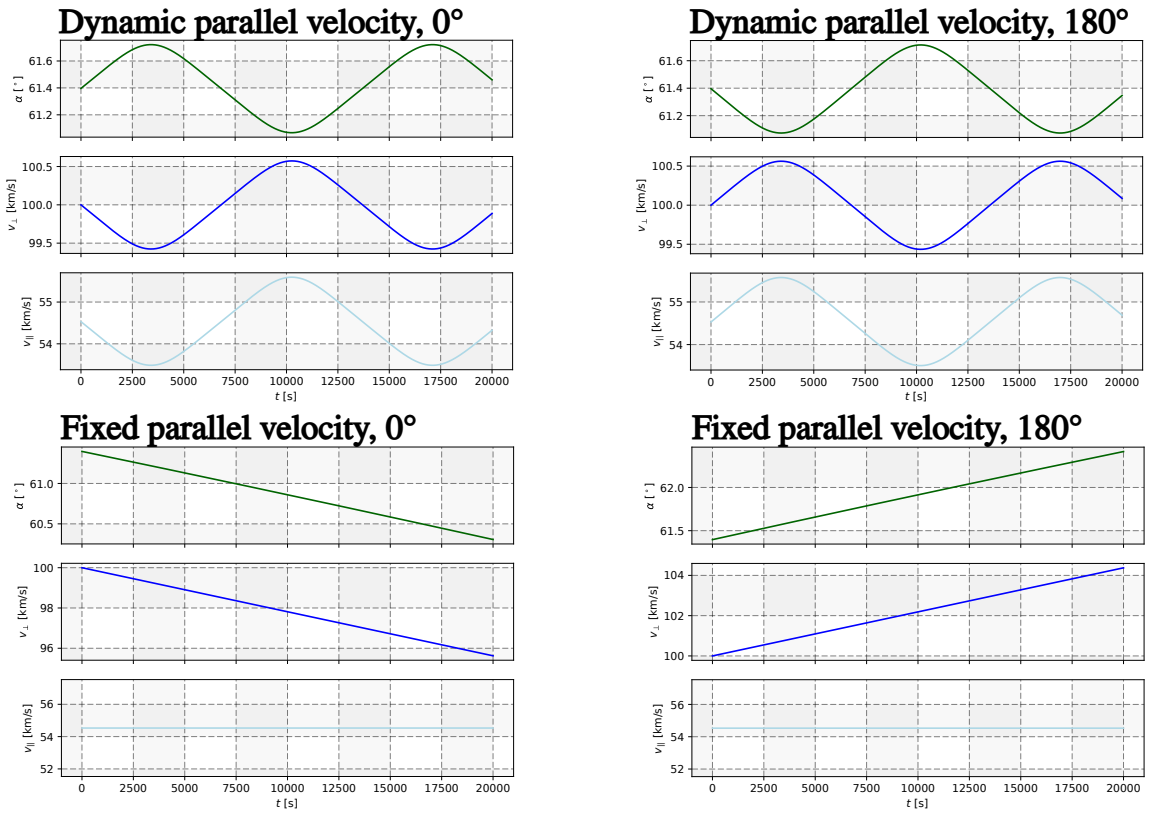


Figure 30: Time evolution of an initially cyclotron resonant particle's pitch angle, perpendicular and parallel velocity. In the bottom panels the particle's parallel velocity was fixed. The left plots show the time evolution for a wave starting at an initial phase of  $0^\circ$  and the right plots show the time evolution for the wave starting at a phase of  $180^\circ$ . The bottom plots correspond to a simulation, where the particle parallel velocity is kept on a fixed value. The top plots correspond to a simulation, where the parallel velocity is allowed to change during simulation.

---

### 5.1.3 Time-evolution of the pitch angle distribution of an initial torus

We now display the effect of a mono frequent wave to a torus distribution using the simulation setup used to obtain fig. 27 of chapter 5.1.1, but with the modification, that this time 500 test particles distributed randomly on a  $120^\circ$  PUI torus are sampled.

Fig. 31 shows the resulting time-evolution of the pitch angle distribution taken from three simulations featuring 5, 25 and 1000 wave cycles. In the top and middle panel the time resolution allows to observe distributions revealing pitch angle oscillations similar to those observed in chapter 5.1.1 with single particles. However, since the torus distribution is a conglomerate of various phase differences, the distribution consists of the superposition of different oscillations at different amplitudes, frequencies and starting phases attributed to the different initial locations on the torus in velocity space (compare chapter 5.1.1). That's why the particles are swiftly separated from each other.

The middle panel already suggests, that the oscillatory behavior of the pitch angle is stationary, although due to the varying frequencies of pitch angle oscillation the overall distribution seems to become smoother. That's why in the bottom panel the pitch angle evolution during 1000 wave cycles is shown. There it can be seen, that after an initial condition of starting the oscillation the individual pitch angle trajectories, which contribute to the distribution, oscillate stationary and create a pitch angle distribution constant in time.

The bottom panel also shows, that an average of the wave-influenced pitch angle distribution over time appears significantly broadened versus the initial condition (which is a delta peak in pitch angle space). However, the broadness of the pitch angle distribution remains constant after a short period of time, where the particles start reacting to the wave, since the time average of the particles' pitch angle distribution is reflecting the observed oscillations in pitch angle.

In such a time average the most prominent pitch angles will be those, where many particles are during a comparatively long period of time. As evident from fig. 31, the most prominent pitch angle is the initial pitch angle ( $120^\circ$ ), because it is an extremum of all trajectories in pitch angle or at least of those observable in the middle panel fig. 31. Two other pitch angles, which should also be observed with most time averaged particle densities are the extrema of the pitch angle oscillations of the most prominent trajectories in pitch angle space given in the middle panel (at  $\sim 137^\circ$  and  $\sim 110^\circ$ ).

Since the observations of chapter 5.1.1 already suggested, that the qualitative behavior of pitch angle trajectories is a function of the initial phase difference between particle gyration and wave elongation, we select 20 particles of the PUI torus at equidistant initial phases and plot their pitch angle trajectories marked by the initial phase, which is shown in fig. 32. It can be seen there, that the time evolution of the pitch angle distribution is caused by particles at different phases being scattered differently. Particles with initial phases close to 0 (or  $2\pi$ , respectively) are oscillating most strongly in pitch angle, where particles close to  $\pi/2$  are oscillating with lower amplitudes in pitch angle. This behavior can be explained by the calculations done in appendix B, where it is shown, that the time derivative of the particles' velocity components is dependent on the sine of the phase (please note, that the initial value of the phase difference is offset in the simulation versus the calculated values by a constant phase). We will discuss this behavior further in the next chapters.

As for the results of this chapter we denote, that when considering the periodic motion of all particles, it is valid to use a time-average of the pitch angle distribution for a sufficiently long simulation as a measure of the particle's behavior, since the particles' pitch angles perform stationary oscillations. Then it needs to be interpreted as a projection of the various periodic motions and also as a measure for the probability to meet a particle at that pitch angle when not knowing the time, when the wave started affecting the distribution. Therefore in the next chapter time-averaged pitch-angle distributions are used to investigate, how the behavior of the pitch angle of a torus distribution in a continuous wave field is influenced by the wave's

---

frequency.

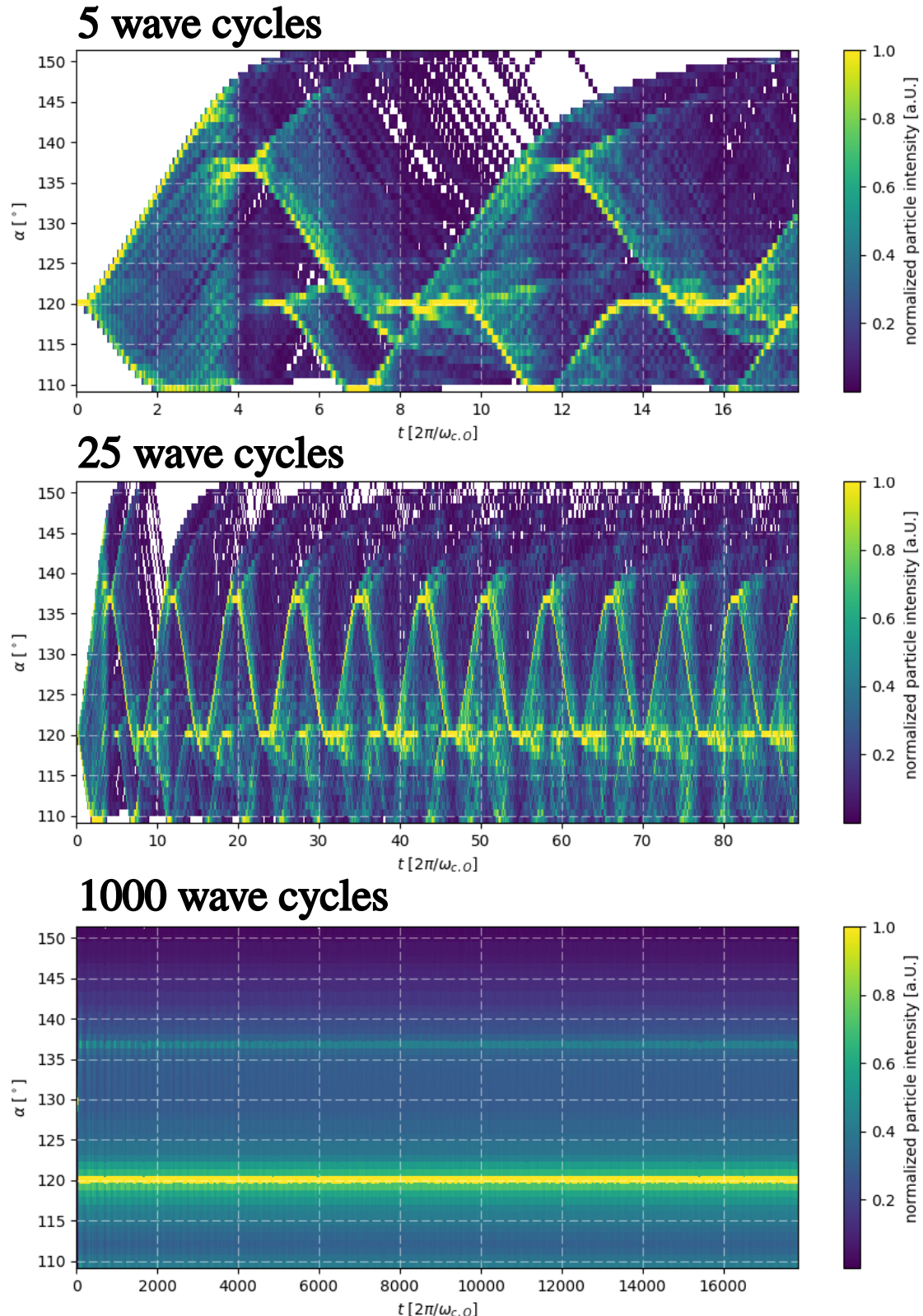


Figure 31: Color coded contour plots to show the time evolution of the pitch angle distribution of 500 test particles. The colors represent particle density in arbitrary units normalized to the respective maximum density of each time bin. The top plot shows the time evolution of the pitch angle distribution during the time needed for 5 wave cycles to pass. The center plot shows the time evolution during a time period of 25 wave cycles and the bottom plot for 1000 wave cycles.

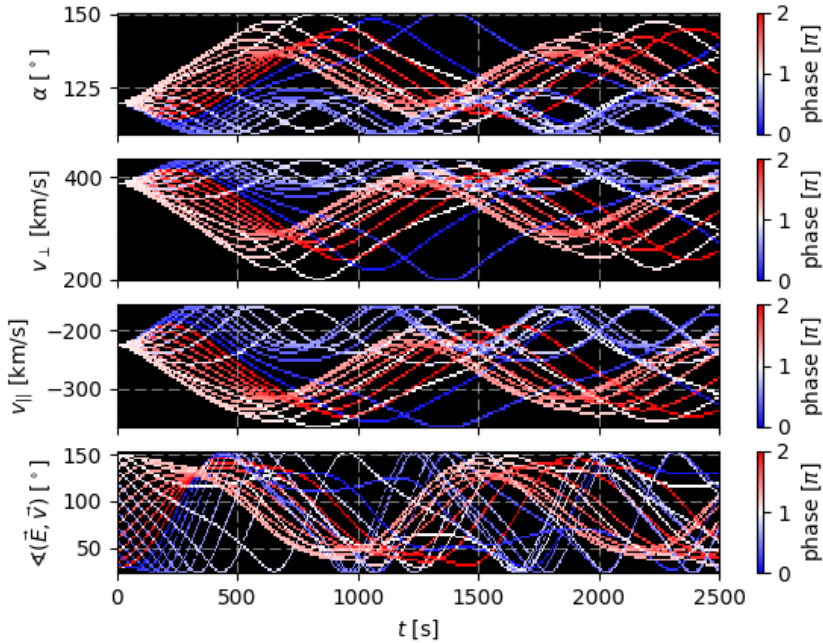


Figure 32: Plot of the particles' pitch angle, parallel and perpendicular velocities and angle between electrical field and particle velocity for 20 particles selected from a torus of  $120^\circ$  initial pitch angle exposed to a wave of a frequency of  $0.28\omega_{c,O}$  with an amplitude of 0.1 nT. The colors are coded by the initial phase difference between particle gyration and wave elongation.

#### 5.1.4 Time-averaged pitch angle distributions as a function of the wave frequency

After chapter 5.1.3 discussed the periodic behavior of a PUI torus distribution under the influence of one selected frequency this chapter will focus on discussing, how the wave frequency influences that behavior. Therefore the simulation setup used to obtain the results of chapter 5.1.3 was used to run individual simulations featuring 25 cycles of mono frequent waves with different frequencies.

Fig. 33 shows time-averaged pitch angle distributions as a function of the Doppler shifted wave frequency for a torus distribution of an initial pitch angle of  $120^\circ$ . The Doppler shifted frequencies always refer to the particles' initial velocities. The pitch angle was measured with respect to the background magnetic field. As a comparison fig. 34 shows the analogue with pitch angles measured with respect to the total magnetic field (background and wave, compare chapter 3.3).

As already introduced at the beginning of section 5.1 and now evident from figs. 33 and 34 the overall behavior of the pitch angle distribution can be qualitatively divided into the three regimes of low frequency, high frequency and near-resonance frequency. As expected a strong modification of the pitch angle distribution only takes place in the near-resonance regime (around  $\omega_d \approx \omega_{c,O}$ ). There the averaged pitch angle distribution splits up into branches, which converge at the first order resonance frequency. For frequencies around that point it can be seen, that the distribution is governed by a branch staying at the initial value of  $120^\circ$  and a branch diverging from the initial pitch angle with increasing distance to the first order resonance. For Doppler-shifted frequencies higher than the first order resonance the branch diverges towards smaller pitch angles. For Doppler-shifted frequencies lower than the first order resonance we see this branch diverging towards higher pitch angles. Keeping the results of chapter 5.1.3 and chapter 5.1.1 in mind, these branches can be interpreted as the extrema of the oscillating motion of the particles in pitch angle space. Whether one particle is distributed on one or the other

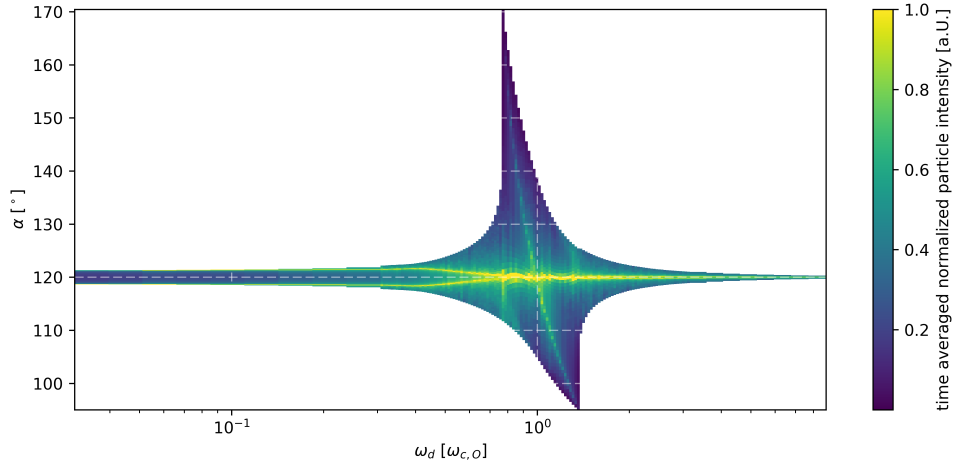


Figure 33: Contour showing time-averaged pitch angle distributions with respect to the background magnetic field as a function of the Doppler-shifted wave frequency. Each y-slice of the histogram was normalized to its respective maximum.

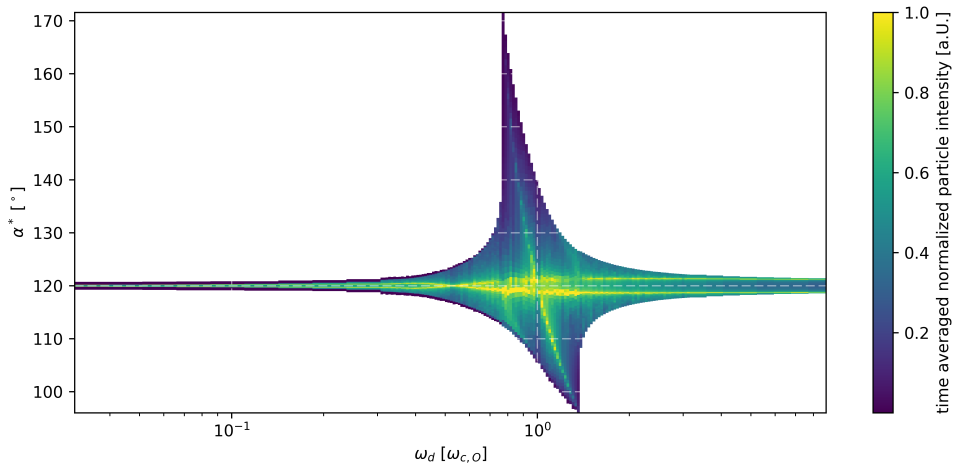


Figure 34: The analogue to fig. 33, but with a pitch angle measured versus the total magnetic field.

---

branch is therefore controlled by its initial phase difference to the wave. One may now ask, why these branches point for higher frequencies (with respect to the cyclotron-resonant frequency) towards lower pitch angles and for lower frequencies to higher pitch angles.

A working theory (which will be investigated further in chapter 5.1.5) is, that the strongest interaction between particle and wave is the interaction, that synchronizes particle and wave. This is also something, one would expect from the theory of resonant wave particle interactions (compare chapter 2.4.2). An increasing parallel velocity (increasing pitch angle) means to a particle at a frequency slightly lower than the resonance frequency, that the Doppler shifted frequency of the wave with respect to the particle increases. Hence an increasing pitch angle seeks to synchronize particle and wave here. Therefore the outer branches diverge more from the initial pitch angle as the frequency difference to the resonant frequency increases.

Yet, at Doppler shifted frequencies larger than  $\sim 1.2\omega_{c,O}$  or lower than  $\sim 0.8\omega_{c,O}$  the outer branches cease to exist. Further discussion of this will be given in chapter 5.1.5.

Let's now consider the regime of low frequencies, where we see from the pitch angle measured with respect to the background magnetic field (fig. 33), that the averaged pitch angle distribution splits up into two pronounced branches at constant pitch angles located at  $\sim \pm 1^\circ$  around the initial pitch angle. Since the particles' gyro motion is much faster than the change of the wave magnetic field the particles have enough time in this frequency regime to adapt to the changing magnetic field making the total magnetic field qualitatively the background magnetic field. Therefore a rotation of the torus distribution takes place given by the angle between background and total magnetic field as depicted in fig. 35. The effective pitch angle change can therefore be estimated by the amount of rotation, namely  $2 \cdot \beta = 2 \cdot \arctan(\delta B/B_0) = 2.28$ , which matches the observations.

Hence it is better to observe the pitch angle with respect to the total magnetic field (fig. 34) in this frequency regime, which effectively shows no significant modification of the pitch angle distribution at low frequencies. However, in the high frequency regime we see the pitch angle with respect to the total magnetic field splitting up the same way, the pitch angle with respect to the background field did at low frequencies. The split up seen in the pitch angle with respect to the total field is merely caused by the frame of reference rotating with the wave, which causes an apparent rotation of the torus by again  $2 \cdot \beta = 2 \cdot \arctan(\delta B/B_0) = 2.28$ .

During this study similar simulations to those of fig. 33 and 34 have been performed for pitch angles different from  $120^\circ$ . They show comparable results, that are compiled in appendix A

Lastly it is pointed out, that the time averaged distributions look especially in the near resonant regime, as if a heating of the particles has taken place. Knowing the results of the foregoing chapters it can be pointed out, that this is not the case. Still, when looking at pitch angle distributions with a spacecraft, always time-averaged distributions are taken. It is impossible to obtain data with a time resolution sufficient to resolve the small scaled motions in pitch angle space seen in the previous chapters, so that spacecraft data would always suggest apparent heating in this situation.

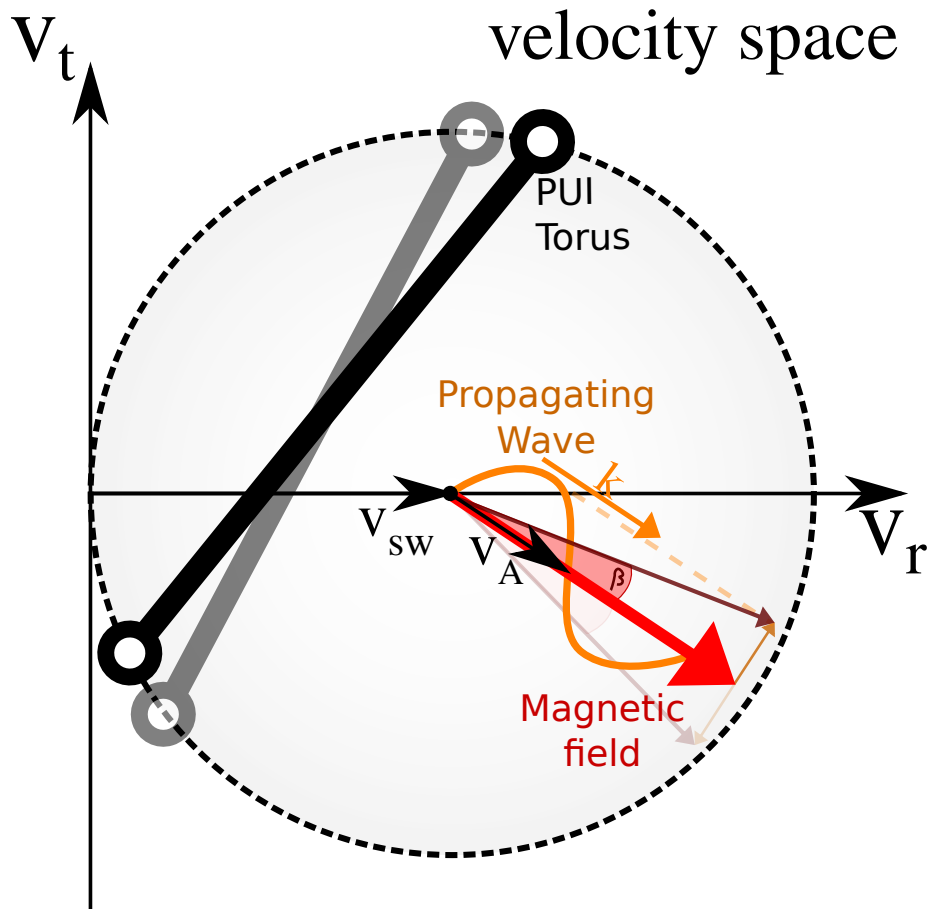


Figure 35: Sketch in analogy to fig. 25 showing the background, wave and total magnetic field, in which the torus distribution is situated. When slow waves (compared to the oxygen cyclotron frequency) pass the particles, the torus is rotated by a maximum angle of  $2 \cdot \beta$ .

---

### 5.1.5 Study of wave particle interactions as a function of the wave amplitude

After our survey of how the wave frequency controls wave particle interactions we now focus on looking at wave particle interactions as a function of the wave amplitude. Generally it is expected, that the overall effect on pitch angle distributions increases with wave amplitude, since the force applied to a particle during one time step is linearly dependent on the wave amplitude (the electric field caused by the wave scales linearly with the magnetic wave amplitude and the Lorentz force is proportional to the total magnetic field). But since generally a change in pitch angle is also effected by the particles' hysteresis, that expectation may be wrong.

Fig. 36 shows time-averaged pitch angle distributions as a function of the wave amplitude for a simulation setup similar to the one used to obtain the results of chapter 5.1.4. The initial pitch angle of the particles is  $120^\circ$  and the wave frequency was chosen in such a way, that first order resonance occurs, which is  $0.323\omega_{c,O}$  (compare fig. 9 of chapter 2.3.4). As expected the effect to the pitch angle distribution increases with the wave's amplitude. The standard deviation is increasing with amplitude while the mean value is shifting by an insignificant value. So in general the expectation is matched.

However, the exact behavior of the pitch angle distribution as a function of the amplitude is also dependent on the wave frequency, as fig. 37 shows. There time-averaged pitch angle distributions are to be seen as a function of wave frequency, which is basically the study of chapter 5.1.4 performed for several amplitudes. These plots acknowledge the expected general trend, that fig. 36 showed. They also show, that the evolution of the pitch angle distribution with the wave amplitude is dependent on the wave frequency. The branch structure of the time averaged pitch angle distribution (compare chapter 5.1.4) in the resonant frequency regime ( $\omega_d \approx \omega_{c,O}$ ) is present in the distributions corresponding to wave amplitudes of 0.5 nT, 0.1 nT and 1.0 pT. In the plot featuring an amplitude of 0.1 pT the frequency resolution is not sufficient enough to identify the structure. The extent of the branch structure in pitch angle space is increasing with increasing wave amplitudes. It also increases its extent in frequency space, when larger wave amplitudes are applied. The first is not surprising, but the fact, that the structures increase in width on the frequency axis, when the amplitude is increased, needs discussion.

Therefore we investigate the time evolution of the pitch angle distribution of a  $120^\circ$  torus for several amplitudes at a wave frequency of  $0.28\omega_{c,O}$ , which is a Doppler shifted frequency of  $0.865\omega_{c,O}$ . The result is depicted in fig. 38. We see, that for decreasing amplitudes on the one hand the extrema of the pitch angle trajectories move narrower together and on the other hand the extrema of the trajectories resemble more and more an undeformed sine, which is a sign for trajectories, that are only influenced by the torus rotating together with the wave magnetic field. Trajectories that go further than the displayed sine trajectories are only present for higher amplitudes, which evidently creates the observed branch-structure of time averaged pitch angle distributions as a function of the frequency. It is worth investigating, what causes this branch structure. Therefore in fig. 39 the trajectories of two selected particles with initial phases of  $\pi$  and  $2\pi$  are plotted over time for a wave frequency of  $0.28\omega_{c,O}$  and two different wave amplitudes. It can be seen, that at both amplitudes the particle with a phase of  $\pi$  oscillates sinusoidally with a small amplitude. But the particle with a phase of  $2\pi$  shows a different behavior dependent on the wave amplitude. In the case of a lower amplitude the particle performs a slow oscillation in pitch angle. This oscillation is mainly sinusoidal, but with a lower amplitude and higher frequency at pitch angles smaller than the initial values. At pitch angles larger than the initial value it has a higher amplitude and lower frequency. This is caused by an acceleration in the parallel component followed by a deceleration. Whenever the angle between velocity and electric field is larger than  $90^\circ$  the particle gains parallel velocity. We see, that the angle changes slower as the parallel velocity increases. But it still reaches  $90^\circ$  coming from higher angles. Therefore the parallel component is not modified anymore, but since the particle gyro motion and the wave are not synchronous, the particle will wander to different wave phases. Therefore the angle

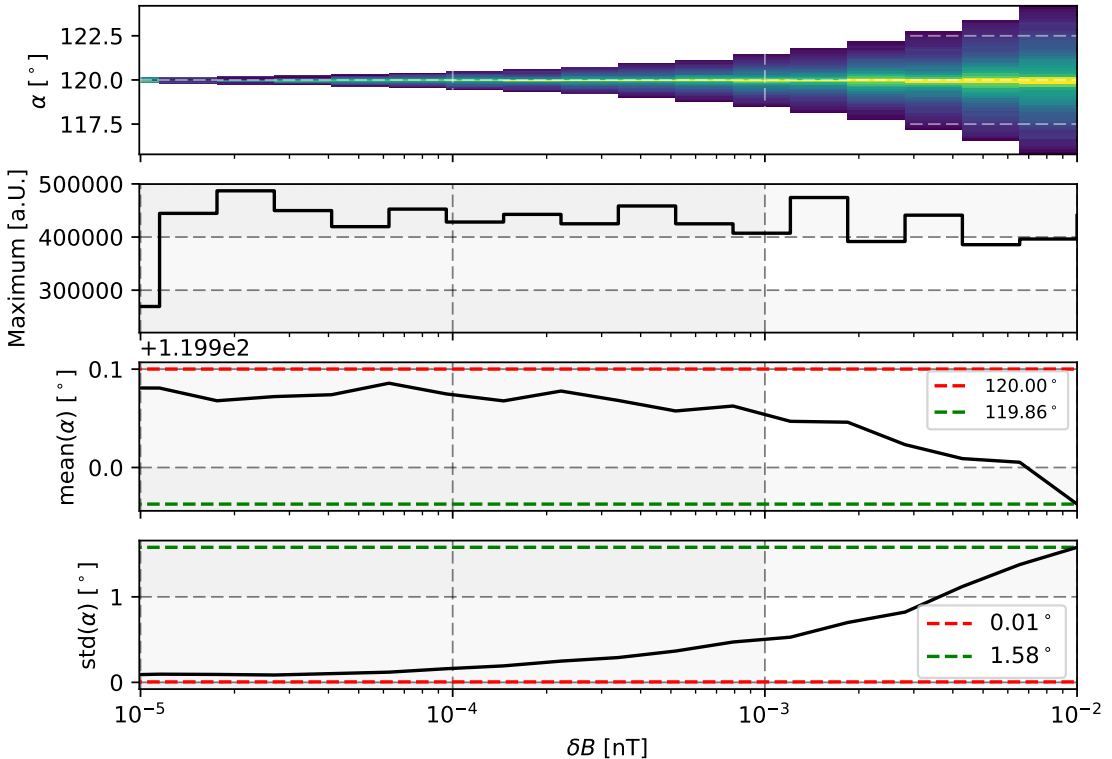


Figure 36: Top panel: Time-averaged pitch angle distributions as a function of the wave amplitude (Each y-slice of the histogram was normalized to its respective maximum). Second top panel: Maximum particle density of each y-slice of the top plot, before it was normalized. The two bottom panels show the mean value and standard deviation of the distributions. The dashed lines in the third top panel represent the maximum (red) and minimum (green) occurred mean pitch angle. The dashed lines in the bottom plot represent the standard deviations of the pitch angle at the wave amplitudes, where the maximum or minimum mean pitch angles occurred. Of the whole range of simulated wave amplitudes ( $10^{-11}$  nT to  $10^{-2}$  nT) only the relevant part is shown. In the area of lower amplitudes than the shown ones the mean pitch angle approaches  $120^\circ$  and the standard deviation  $\sim 0^\circ$ .

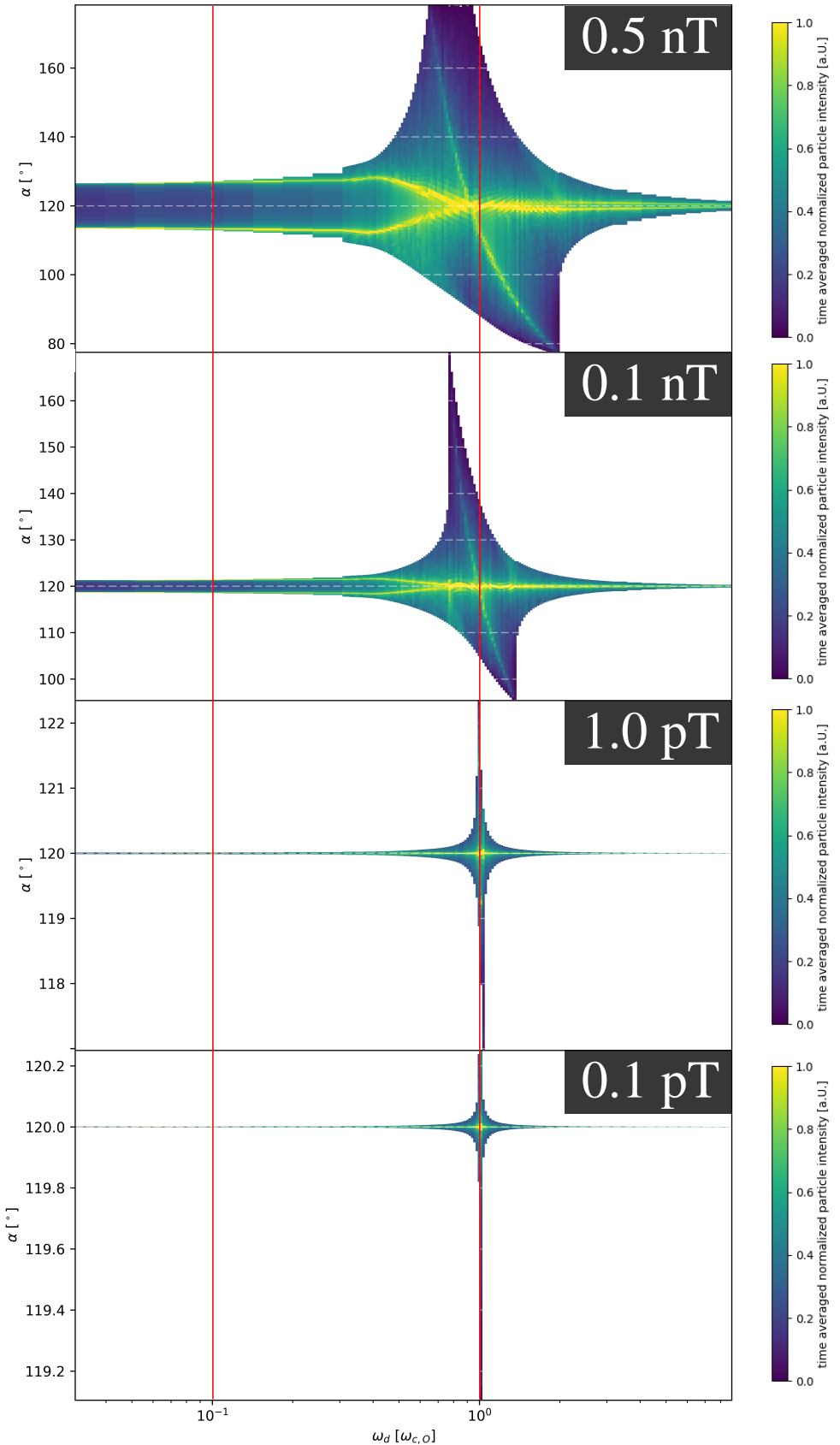


Figure 37: Analogue plots to fig. 33 for wave amplitudes of 0.5 nT, 0.1 nT, 1.0 pT and 0.1 pT (from top to bottom). The test particles were initially distributed on a torus distribution of  $120^\circ$  initial pitch angle. The vertical red lines mark a Doppler shifted wave frequency of  $0.1 \omega_{c,O}$  and of  $1 \omega_{c,O}$ . The respective  $y$ -scale of each plot was chosen individually, so that the characteristic behavior of the pitch angle distributions is resolved in a better way.

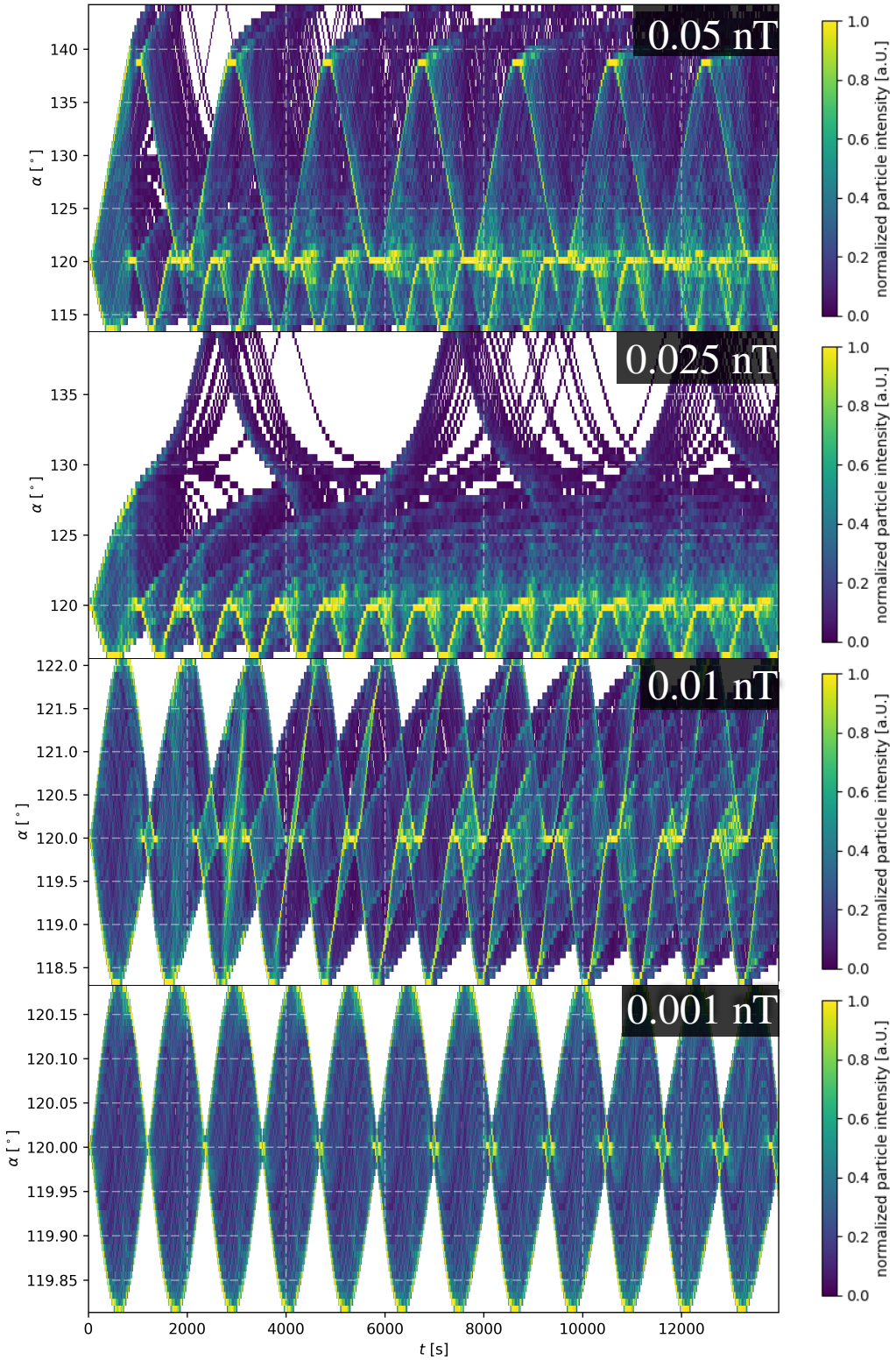


Figure 38: Time evolution of the pitch angle distribution of an initial  $120^\circ$  torus for several amplitudes. The amplitude of the  $0.28\omega_{c,O}$ -wave is labeled in each panel. The respective  $y$  scale of the panels was chosen differently for each panel, so that each time evolution can be resolved well.

---

decreases as the wave propagates with respect to the particle's oscillation. Thus the parallel component is decelerated and the angle reaches a minimum, where the parallel velocity is much slower than before causing the angle to change swifter as the wave is more non-synchronous with the particle oscillation. All in all this behavior looks like the particle going through wave elongations directed in favor of positive parallel velocity change and the opposite, as the wave comes through. While this happens the phase difference between particle and wave changes at a varying speed dependent on the difference between cyclotron motion and Doppler shifted wave frequency. So at one phase of the pitch angle oscillation the particle acts more synchronous than at another phase.

We see, that this behavior is dependent on the particle's initial phase, which can be explained by the fact, that at low amplitudes (or frequencies sufficiently far away from resonance) the only interaction between particle and wave is seen to be a rotation of the torus caused by the varying magnetic field. Therefore particles are drawn towards higher or lower parallel velocities dependent on their position on the torus making particles more or less synchronous with the wave caused by Doppler shift.

Let's now consider the particles of fig. 39 exposed to a slightly higher wave amplitude. There the  $2\pi$  particle performs a pitch angle oscillation of significantly higher amplitude, which would effectively contribute to the branch structure. Its trajectory in pitch angle shows a distinct saddle point between its outer extrema. At that point the angle between electric field and particle velocity has a dip, but stays at values higher than  $90^\circ$  after coming from a local maximum. It then goes to a local maximum once again, which is the main qualitative difference in the particle's behavior compared to the case of the lower amplitude. We explain that behavior by the Doppler shifted wave oscillation overtaking the particle gyration, since (taken from the time evolution of the angle between electric field and particle velocity) the particle is seeing the same phase difference between gyro motion and wave elongation once again. When that happens, the angle stays larger than  $90^\circ$  for a longer time, than in the case of a lower amplitude. So the parallel acceleration can be maintained over a longer period in time. Later the regime of angles lower than  $90^\circ$  is reached, where the particle is decelerated. This decreases the Doppler-shifted wave frequency, so that the particle gyro motion will overtake the perceived wave elongation and the particle returns to its initial conditions.

As a criterion for this overtaking we note, that the Doppler shifted wave (compare chapter 2.4.2) frequency needs to exceed the particle cyclotron frequency, namely  $\omega_{c,O} < \omega_d = \omega + k|v_\parallel|$ . This can be rewritten into

$$|v_\parallel| > \left| \frac{\omega_{c,O} - \omega}{k} \right| \quad (40)$$

and yields a minimum absolute parallel velocity required for overtaking, which in the case of fig. 39 is  $\sim 277$  km/s. That's where the saddle point in the  $2\pi$  particle's trajectory is found. For further visualization of this overtaking one may watch the animation accessible via the compact disc appended to this work (further information to the disc is given in appendix F). There the trajectories in velocity space of two selected particles from fig. 26 of chapter 5.1.1 have been animated.

We now want to give further proof to the theory, that the branch structure observed in the frequency dependent behavior of time averaged pitch angle distributions is caused by the particle gyration overtaking the wave propagation and reversed using the system of differential equations for the particle's motion provided in appendix B. Fig. 40 shows the results of integrating these equations using Euler's approach with the same boundary conditions as for fig. 39. The slight deviations in velocities result from numerical errors. The different initial phase differences of the particles correspond to a differently chosen coordinate system. Overall they show the same behavior of the particle in terms of parallel velocity. The wave phase shows, that in the case of a lower amplitude the particle advances further in the system of a resting wave, but bounces

---

from maximum to minimum in the case of a higher amplitude. The difference between Doppler shifted frequency and cyclotron frequency is always larger than 0 at the lower amplitude, but changes its sign at the extrema of the phase's time evolution at the higher amplitude.

To further illustrate the importance of a particle's starting phase the simulation yielding the higher amplitude panels of fig. 39 has been conducted with 1000 particles over a time of 5 wave cycles to obtain time-averaged pitch angle distributions as a function of the particle's initial phase shown in fig. 41. The left panels show these distributions for a wave of  $0.28\omega_{c,O}$  frequency, which is below cyclotron resonance for a pickup ion torus of  $120^\circ$ . As expected a strong dependency of the spread in pitch angle of the initial phase is to be seen. At phases below 0 a small spread in pitch angle is to be seen, which corresponds to the  $\pi$ -particles of fig. 39, which oscillate at a low pitch angle amplitude (the position of zero phase on the torus was chosen differently in fig. 39). Around a phase of  $\sim -0.5\pi$  the apparent spread in pitch angle increases with distance to that pitch angle until it reaches a point, where the criterion of overtaking is met. We especially see, that the pitch angle spread increases only towards higher pitch angles. Where the criterion of overtaking is met (approximately at positive phases) the apparent pitch angle spread increases strongly. The lower extremum of the pitch angle distributions resembles a sine function. The upper extremum of the pitch angle distribution also resembles a sine function, but only where the overtaking criterion is not met. Where the criterion is met the upper extremum varies around  $135^\circ$  and  $140^\circ$ .

In the right panels of fig. 41, where the same experiment was conducted with a wave frequency of  $0.38\omega_{c,O}$  a similar behavior can be seen, but reversed in pitch angle. This matches the observations of chapter 5.1.3, where a branch of the pitch angle distribution went to lower pitch angles when the frequency is set to values above the resonance frequency.

All in all this explains the origin of the observed branch structure around the resonance frequency. What is not explained is the fact, that the branch structure shows branches in the pitch angle distribution increasing their pitch angle distance to the initial value with increasing frequency distance to the resonance frequency up to a frequency distance, where they suddenly vanish. Therefore we discuss the time derivative of the perpendicular velocity component derived in appendix B (equation 50) further. It reads

$$\dot{v}_\perp = \frac{q\delta B}{m} \sin(\Delta\varphi) (v_{||} - v_\varphi).$$

So the modification of  $v_\perp$  is generally proportional to the velocity difference between parallel and phase velocity, which explains the increasing distance of the branches to the starting pitch angle when the wave frequency deviates more from the resonance frequency. Considering the conservation of the particle's energy in the wave frame the direction of the modification of the perpendicular velocity decreases the difference between parallel and phase velocity. Yet a modification of the parallel velocity changes the rate, with which the phase difference  $\Delta\varphi$  increases or decreases over time and that is the key to understanding, why the branch structure diminishes, when the difference between gyro and Doppler shifted wave frequency is too high. As explained in appendix B (equation 51) the time derivative of the phase difference can be written as

$$\frac{d}{dt} \Delta\varphi = \omega_c - \omega + kv_{||}.$$

Not considering  $kv_{||}$  the phase difference changes with a rate given by  $\omega_c - \omega$ , which is the difference between particle gyro frequency and wave frequency. Without loss of generality we now assume a wave frequency below resonance, so that  $\omega_c - \omega > 0$  applies. Therefore at a torus of pitch angles larger than  $90^\circ$  (for smaller pitch angles the particles overtake the wave and therefore see the wave polarized in the wrong direction for resonances)  $kv_{||}$  is negative. So we interpret it as working against the constant phase change caused by the difference in gyro and wave frequency. When it outweighs this constant change, the particle overtakes the wave.

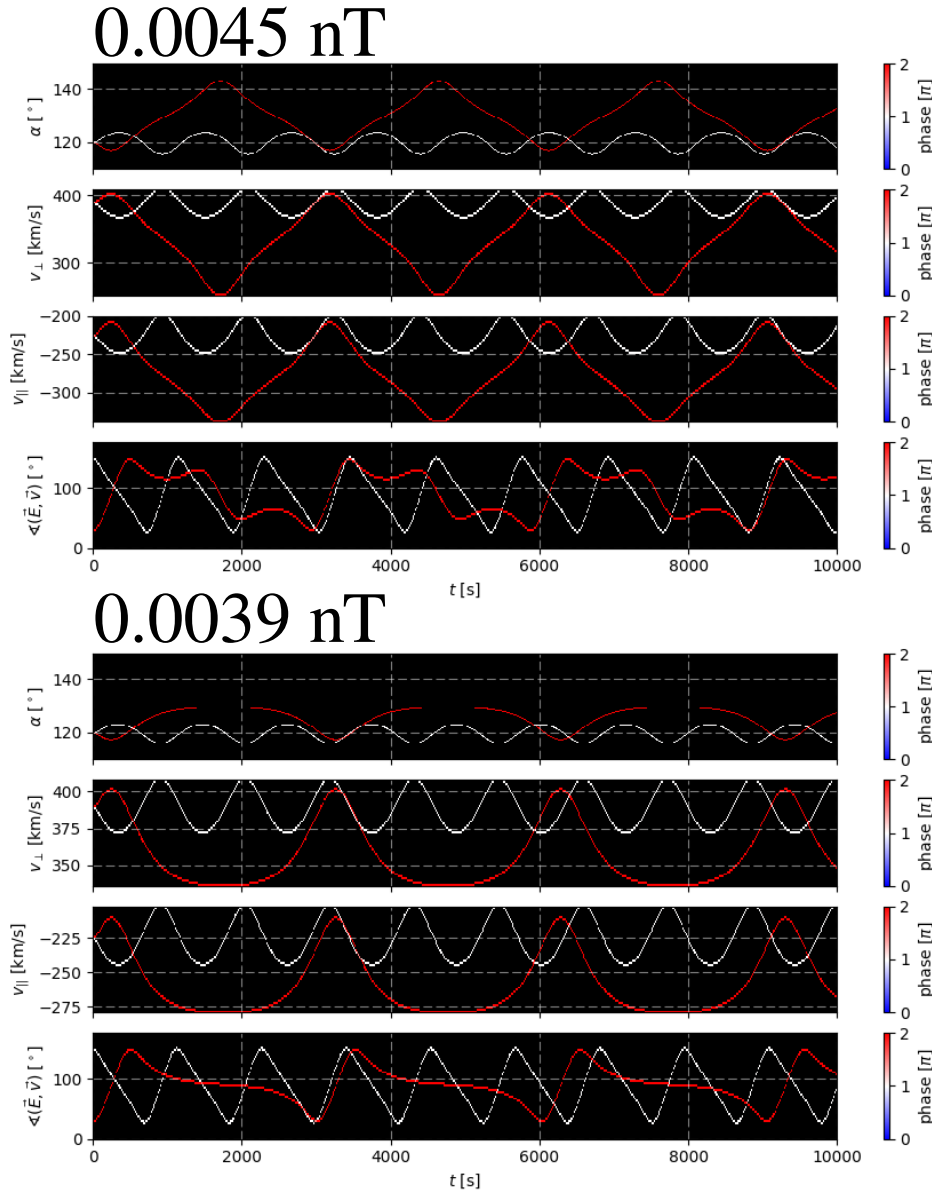


Figure 39: Plots of two selected particles' trajectories in pitch angle, parallel and perpendicular velocity and angle between velocity and electric field over time. The top panels refer to a simulation run with a wave of 0.0045 nT amplitude. The bottom panels refer to a slightly lower amplitude (0.0039 nT). The colors of the plotted trajectories represent the respective initial phase difference of the particles' gyro motion to the wave. The white plotted trajectories correspond to an initial phase difference of  $\pi$  and the red plotted ones correspond to  $2\pi$ .

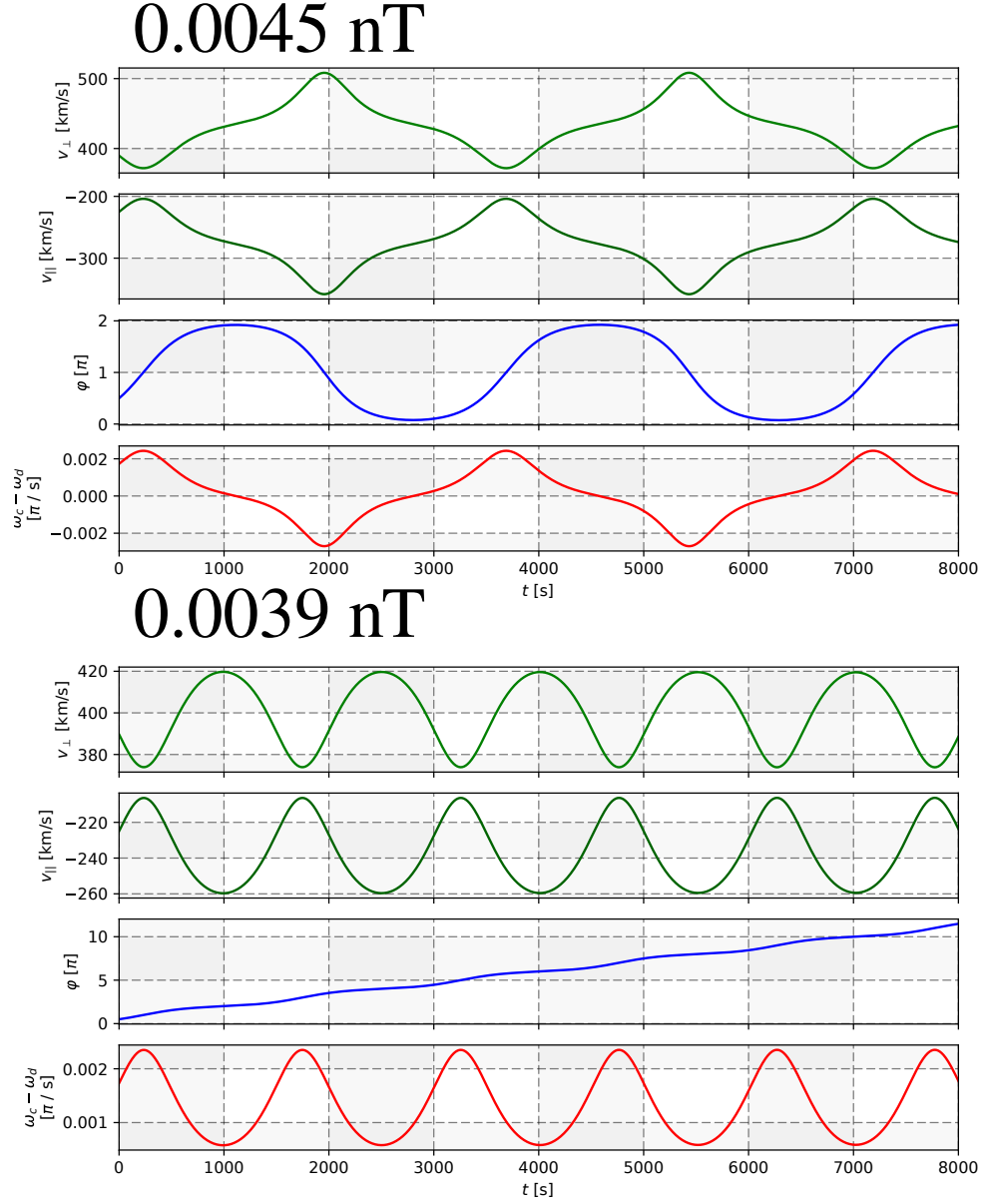


Figure 40: Plots of a selected particle's trajectory in parallel and perpendicular velocity, phase difference between wave and particle and difference between Doppler shifted wave frequency and particle cyclotron frequency over time. The top panels refer to a simulation run with a wave of 0.0045 nT amplitude. The bottom panels refer to a slightly lower amplitude (0.0039 nT). The plots are not the result of a simulation using the usual algorithm. They are an integration of the differential equations of Appendix B, obtained from Euler's method.

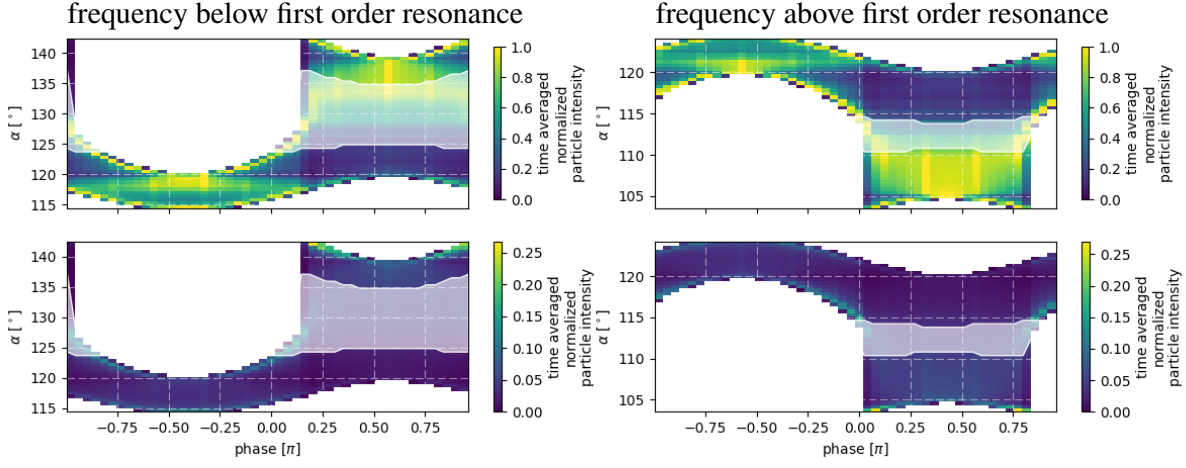


Figure 41: Time-averaged pitch angle distributions as a function of the particles' initial phase. The upper panels show the distributions normed to their respective maximum, the lower show them normed to their sum. The left panels correspond to a simulation conducted with a wave of  $0.28\omega_{c,O}$  frequency, the right panels to  $0.38\omega_{c,O}$ . The areas, where a white shade superimposes the distributions, show the pitch angle corresponding to the (tentative) parallel velocity required for the criterion of particle gyration overtaking the wave propagation (the solid white areas correspond to combinations of pitch angle and phase, where no particle has been observed). The spread and variation of this angle is due to the variation of the total velocity of the particles contributing to a bin of the distributions. The phase coordinate system was chosen different from fig. 37, so that the phase takes values in the range of  $[-\pi, \pi]$ .

Setting the time derivative of  $\Delta\varphi$  to 0 also yields equation 40. From fig. 40 we have seen, that particles overtaking the wave do so, before the phase difference reaches  $2\pi$  and then bounce back and forth around the same position in the wave frame. Particles not overtaking the wave reach phases of  $2\pi$  and beyond. Considering, that the modification of the perpendicular velocity is proportional to the sine of the phase, this makes sense, since at  $2\pi$  the sine reaches 0. So in general for a particle overtaking the wave and thus contributing to the branch structure it needs to meet the overtaking criterion  $k|v_{||}| > |\omega_c - \omega|$ , before  $\Delta\varphi$  reaches  $2\pi$ .

We will now derive a qualitative trend of the minimum wave amplitude that is required to create the branch structure as a function of the Doppler shifted wave frequency. This is also the required wave amplitude to meet the condition of overtaking. We therefore assume (in approximation)  $v_{||}$  to be a linear function over time with  $v_{||} = v_{||,0} + \vartheta \cdot t$ . The linear increase  $\vartheta$  is maximum, when the phase is  $\pi/2$ . Therefore  $\vartheta$  is approximated by eq. 49 (appendix B) through the increase of  $v_{||}$  at the first time step at a phase of  $\pi/2$ , which yields

$$\vartheta := \dot{v}_{||}(t=0) = \frac{q\delta B}{m} \sqrt{\varepsilon - (v_{||} - v_\varphi)^2}, \text{ where} \quad (41)$$

the conservation of  $\varepsilon$  has been used to obtain  $\dot{v}_{||}$ . The overtaking criterion is met, as soon as  $kv_{||} = \omega_c - \omega$  applies, so that we may write

$$\omega_c - \omega = kv_{||,0} + k\vartheta t. \quad (42)$$

This should equate at latest, when  $2\pi = \Delta\varphi$  applies. We simplify the approach further, by not considering the  $k\vartheta t$  in the velocity-driven change of phase (as an approximation) to obtain the time  $t$ , when  $2\pi = \Delta\varphi$  applies, so that we obtain

$$t = \frac{2\pi}{\omega_c - \omega + kv_{||,0}}. \quad (43)$$

---

Putting this into eq. 42 we find

$$\delta B = \frac{m}{q} \cdot \frac{(\frac{\omega_c - \omega}{k} - v_{||,0}) \cdot \frac{\omega_c - \omega + kv_{||,0}}{2\pi}}{\sqrt{\varepsilon - (v_{||,0} - v_\varphi)^2}}. \quad (44)$$

With boundary conditions matching the previous simulation this is plotted in fig. 42. It also predicts the behavior for frequencies above the resonance, since similar deliberations apply there. We see, that the amplitude does not match the observed values. Still from this simplified approach the qualitative behavior of the required amplitude as a function of the wave frequency explains the observations. The further away the frequency is from the resonance frequency, the higher is the required amplitude for overtaking. When the frequency difference is too high, the wave does not match the required amplitude and the particle won't overtake the wave and no branch structure is observed. This explains, why the branches vanish at a certain frequency distance to the resonance frequency. It also explains, why the frequency margin for the branches increases with an increasing wave amplitude.

Before proceeding to the conclusions regarding the interactions with continuous waves, it is noteworthy, that there is a caveat to the theory presented here, since a close look at the highest amplitude case of fig. 36 shows, that the branch structure intersects the starting pitch angle of  $120^\circ$  already at a Doppler shifted frequency of  $\sim 0.92\omega_{c,O}$ . The required parallel velocity for first order resonance is  $-233$  km/s at this wave frequency. In comparison to that the particles sampled in that simulation had an initial parallel velocity of  $-225$  km/s with a pitch angle of  $120^\circ$ . Using the conservation of  $\varepsilon = (v_{||} - v_\varphi)^2 + v_\perp^2$  and  $v_\perp = v_{||} \tan(\alpha)$  we obtain, that the a particle would have changed its pitch angle to  $\sim 115^\circ$  with these boundary conditions in order to reach a parallel velocity of  $-233$  km/s, which is a change of  $\sim 5^\circ$ . Since  $\delta B/B_0 = 0.1$  is very high, it can be expected, that the particles react to the wave field, as if it were a part of the background field. This is supported by the fact, that the pitch angle sampled with respect to the total magnetic field has a point of maximum intensity at  $120^\circ$  at exactly the oxygen cyclotron frequency (compare fig. 61) From earlier considerations it is known, that the pitch angle is tilted by the rotating magnetic field by an angle of  $\arctan(\delta B/B_0) \approx 5^\circ$ , if the particle samples the wave field as a part of the background field, which is the pitch angle, by which the center of the resonant behavior deviates. This once again points out, that one must take caution, when describing the particle's behavior as a function of the initial Doppler shifted frequency, since the particle velocities change dynamically during the simulation.

Similar slight deviations of the point, where the observed branch structure intersects the initial pitch angle, can be observed at pitch angles larger than  $120^\circ$  already for an amplitude of  $0.1$  nT (compare fig. 60) So obviously the theory presented here can only be considered as a first order approximation of the qualitative particle behavior. The deviations from that behavior, as observed here, increase with the wave amplitude (which is due to the fact, that the particle sample stronger fields more and more like the background field and the tilt in pitch angle caused by that increases with the wave amplitude). The deviations also seem to be dependent of the initial pitch angle. However, for the moment there is not enough data available to investigate that dependency further.

### 5.1.6 Conclusions

In conclusion we have observed the behavior of a pickup ion torus in the field of a single continuous wave. The particles initially contributing to the torus perform stationary oscillations in pitch angle space, so that when time-averaging over a wave-influenced pitch angle distribution one observes apparent heating of the distribution. However, the trajectories remain stationary, so that there is no systematic broadening of the pitch angle distribution over time.

We have seen, that the particles do not interact with the wave most strongly at the resonance points predicted by the resonance condition of chapter 2.4.2, because even when a particle is

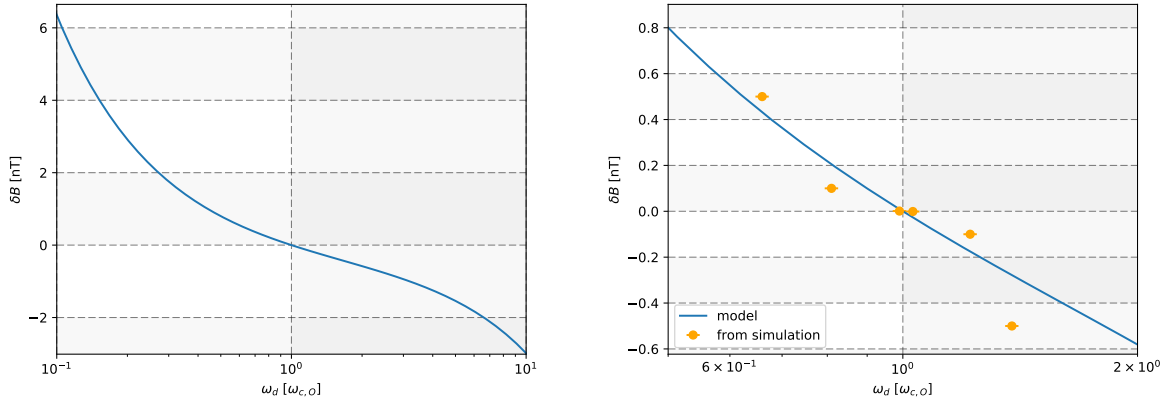


Figure 42: Left: Plot of a qualitative estimation of the required wave amplitude for phase overtaking to take place as a function of the wave frequency according to eq. 44. This is a first-order approach to determining the minimum wave amplitude necessary to create the branch structure as a function of the Doppler shifted wave frequency. Negative values for the amplitude are mathematical artifacts, that correspond to the fact, that the absolute parallel velocity needs to be changed into an opposite direction for  $\omega_d > \omega_{c,O}$  than for  $\omega_d < \omega_{c,O}$  to make particles fulfill the overtaking criterion. Generally the required absolute wave amplitude increases, when the Doppler shifted frequency deviates further from  $\omega_{c,O}$ . When the wave amplitude is smaller than the required amplitude at a given Doppler shifted frequency, the branch structure is not observed. The right plot shows the same function, but in comparison to the observations of the simulation (orange dots (taken from fig. 33 by finding for each panel the maximum and minimum wave frequency, where the branch structure exists)). Since this is only a first order approximation, the given values for the required wave amplitude significantly deviate from the observations. But the qualitative trend of model and simulation are similar to each other (The sign of the amplitudes taken from fig. 33 was inverted for  $\omega_d > \omega_{c,O}$ ).

initialized with a resonant parallel velocity, it is swiftly driven to a non-resonant velocity. Therefore - as a proof of concept - a simulation was conducted, where the parallel velocity is fixed to the resonant value, which resulted in systematic perpendicular acceleration/deceleration.

In general cases the first order resonant frequency still plays an important role, since it determines the time scale, on which a particle's phase difference to the wave changes. Therefore on time scales far away from the resonance frequency weak interactions between particle and wave have been observed, which scale with the wave's amplitude and are due to the fact, that the torus is rotated by the rotating wave influenced magnetic field. At wave frequencies close to meeting first order resonance the time averaged pitch angle distribution consists of two qualitatively different behaving particle populations. One is performing again small oscillations in pitch angle, which are caused by the torus being rotated in the wave field. The other is interacting strongly with the wave and forms a branch in pitch angle space, which deviates further from the initial pitch angle, the further the Doppler shifted wave frequency is away from the first order resonance. When the frequency is too far away from the first order resonance, this branch vanishes. The size of this branch in both pitch angle and frequency scale with the wave amplitude.

Altogether, no systematic time-dependent broadening of the pitch angle distribution was observed in the sense of pitch angle scattering, which leads to the conclusion, that shear interaction with a single continuous wave does broaden the pitch angle distribution systematically over large periods of time.

---

## 5.2 Interactions of oxygen PUIs with an intermittent, single frequency wave

The studies of the interaction of continuous, single frequency waves with test particles showed a stationary and oscillatory behavior of the particles' pitch angle. Yet, the usage of continuous waves is a simplification. Under more realistic conditions we would not expect waves to be continuous. Wave packages passing the observer randomly are more likely expected. We model this by waves fading in and out and present the results of that in this chapter. Since it is generally believed, that wave particle interactions broaden pitch angle distributions over time [Heerikhuisen et al. (2010)] (which, however, was not observed in chapter 5.1), it is of special interest, whether breaking the stationarity of the waves can cause the pitch angle distributions to become broader over time.

### 5.2.1 Convoluting continuous waves with an activation function

We will start our study of the interaction with intermittent waves by investigating, which effect fading a wave in has on the time evolution of pitch angle distributions. Thus the simulation setup of chapter 5.1.3 was modified: The continuous waves of that setup start at zero amplitude at the beginning and are then faded in over various time periods. This approach is shown in figs. 43 and 44.

Fig. 43 shows, that the activation of the wave produces insignificant differences between the pitch angle distributions when fading-in over time periods smaller than one wave cycle. They are similar to the result, when a wave is instantly turned on (top panel of fig. 43). This gives further justification to the approach of chapter 5.1 to fade the waves in over one quarter period, since it was deemed to investigate the interaction with continuous waves and not with waves in the process of activation.

That convoluting the waves with an activation function over longer time periods than one wave cycle can significantly modify the behavior of the pitch angle distribution, is seen in fig. 44, where the time evolution of pitch angle distributions is shown, which are exposed to waves being faded in over 0 wave cycles, 2 wave cycles, 4 wave cycles, and 8 wave cycles. At the beginning the particles behave differently than for waves activated quickly. Still, after the wave has faded in, the pitch angle distribution is once again dominated by stationary oscillations in pitch angle space.

Seemingly the particles behave, when the convolution with an activation function takes a sufficient amount of time, like they were exposed to a lower-amplitude wave and interact weakly with the wave. Their pitch angle oscillations are similar to those observed in chapter 5.1 for lower amplitudes (compare chapter 5.1.5). In that interpretation the trajectories are modified strongly, when the amplitude reaches a critical value, since the wave frequency is at  $0.28\omega_{c,O}$ , which is for a sufficiently high amplitude in the frequency area, where chapter 5.1.4 and chapter 5.1.5 observed the strongest interactions with continuous waves. This can be observed well in the bottom panel of fig. 44. At the beginning the particles perform small oscillations in pitch angle, but then suddenly jump into a different behavior with significantly stronger oscillations in pitch angle.

We study this further by fading the wave in over much larger periods of time. Fig. 45 shows the time evolution of pitch angle distributions exposed to wave fields faded in over 12.5 and 25 wave periods. Together with fig. 43 and fig. 44 it shows, that (as expected) the time, when the stronger modified behavior starts, is correlated to the time needed to activate the wave.

This gives rise to a threshold wave amplitude, that has to exist during a wave cycle for the particle to be swept into stronger modified trajectories, which would belong to the branch structure observed in chapter 5.1.4. This is something also observed in chapter 5.1.5.

This simple study already showed, that fading the wave in produces additional complexity to the time dependent modification of the pitch angle. Still, after the process of fading in the wave, the particles react to it, as if it were a continuous wave by once again performing station-

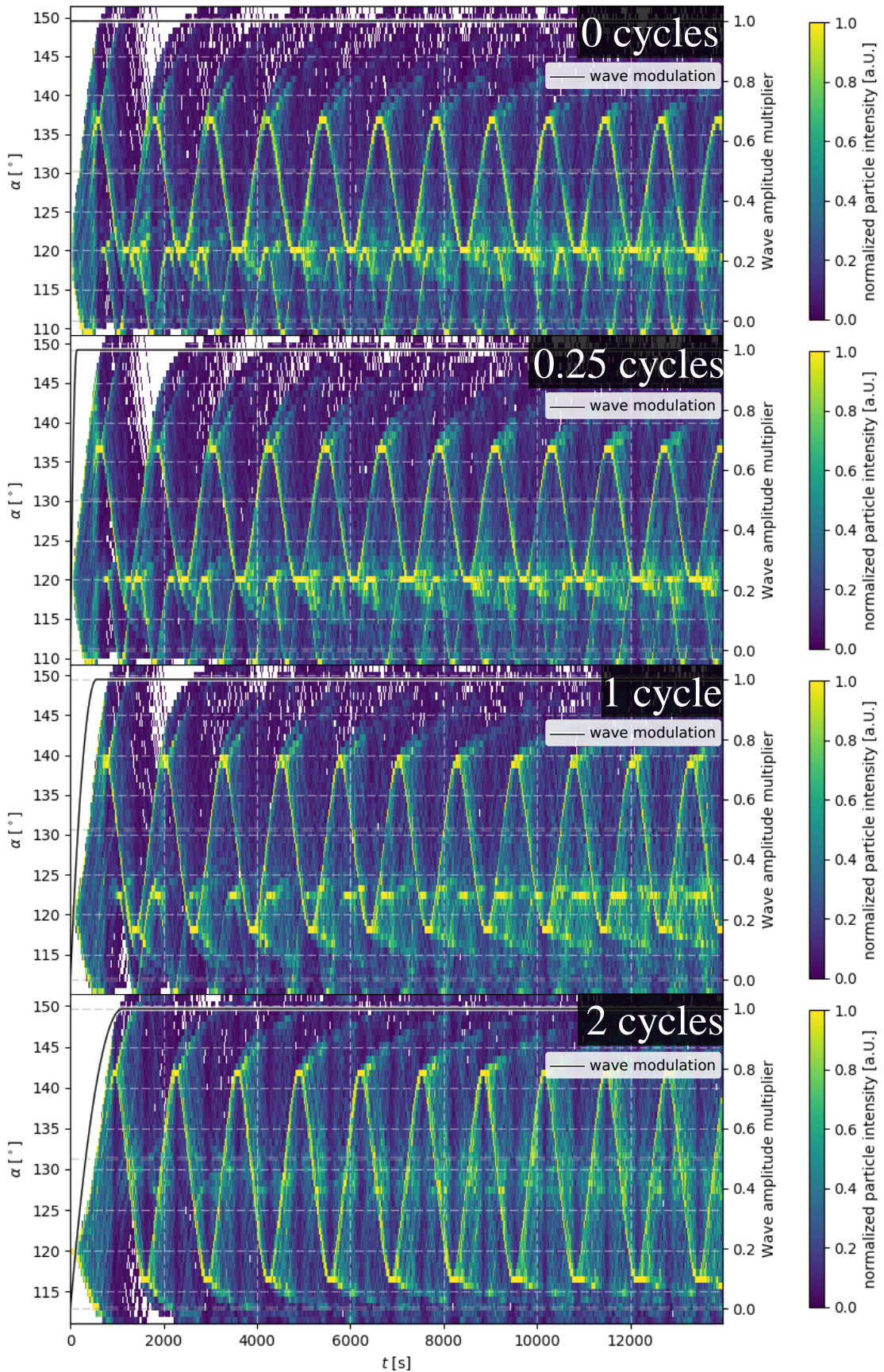


Figure 43: Time evolution of the pitch angle distribution for various time periods of the wave fading in. The time, which the activation of the wave took, is labeled on each panel as number of wave cycles. To illustrate the process of wave activation further, the black line with white edges depicts the function, with which the wave has been modulated.

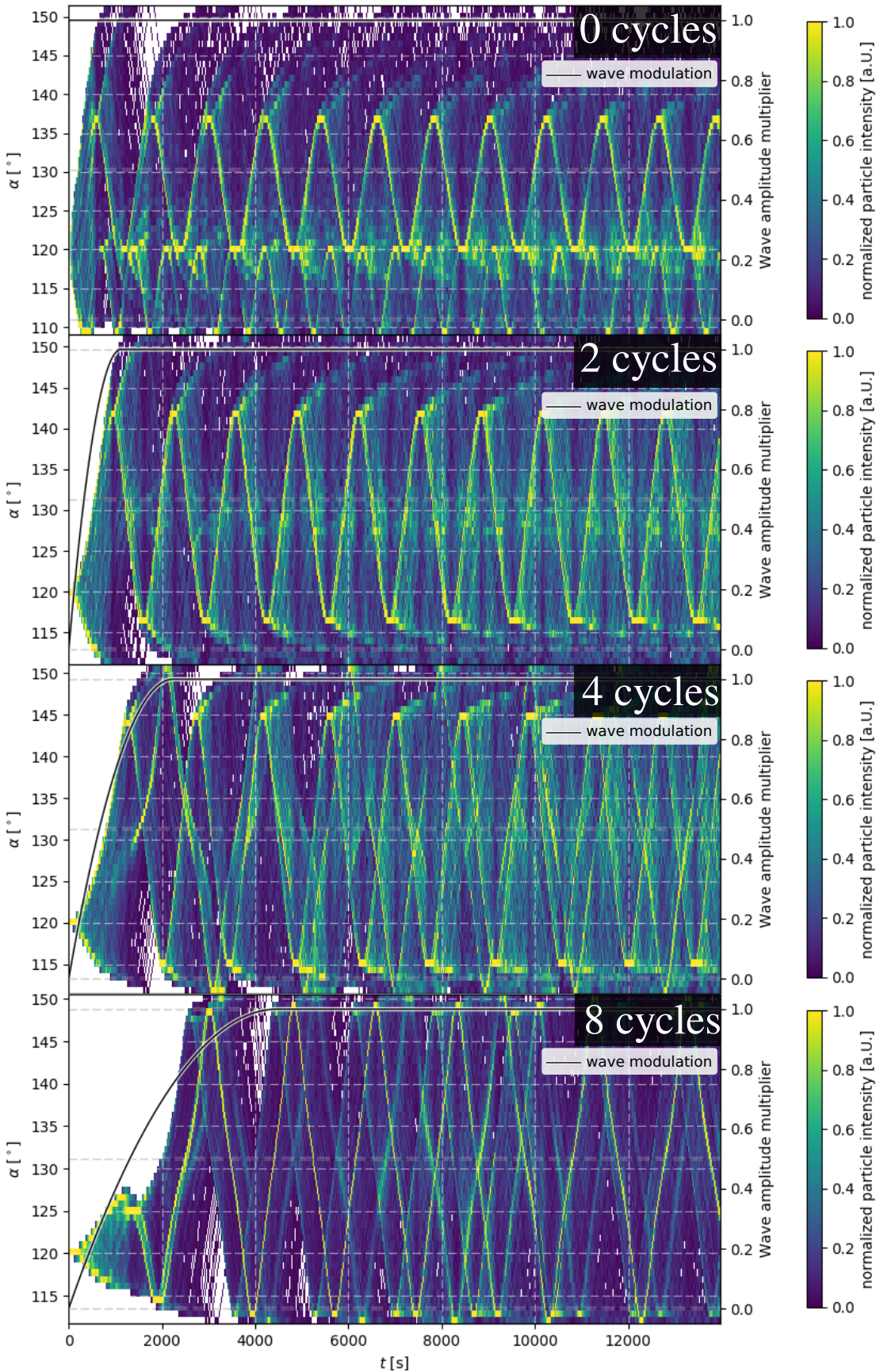


Figure 44: Time evolution of the pitch angle distribution for various time periods of the wave fading in. The time, which the activation of the wave took, is labeled on each panel as number of wave cycles. To illustrate the process of wave activation further, the black line with white edges depicts the function, with which the wave has been modulated.

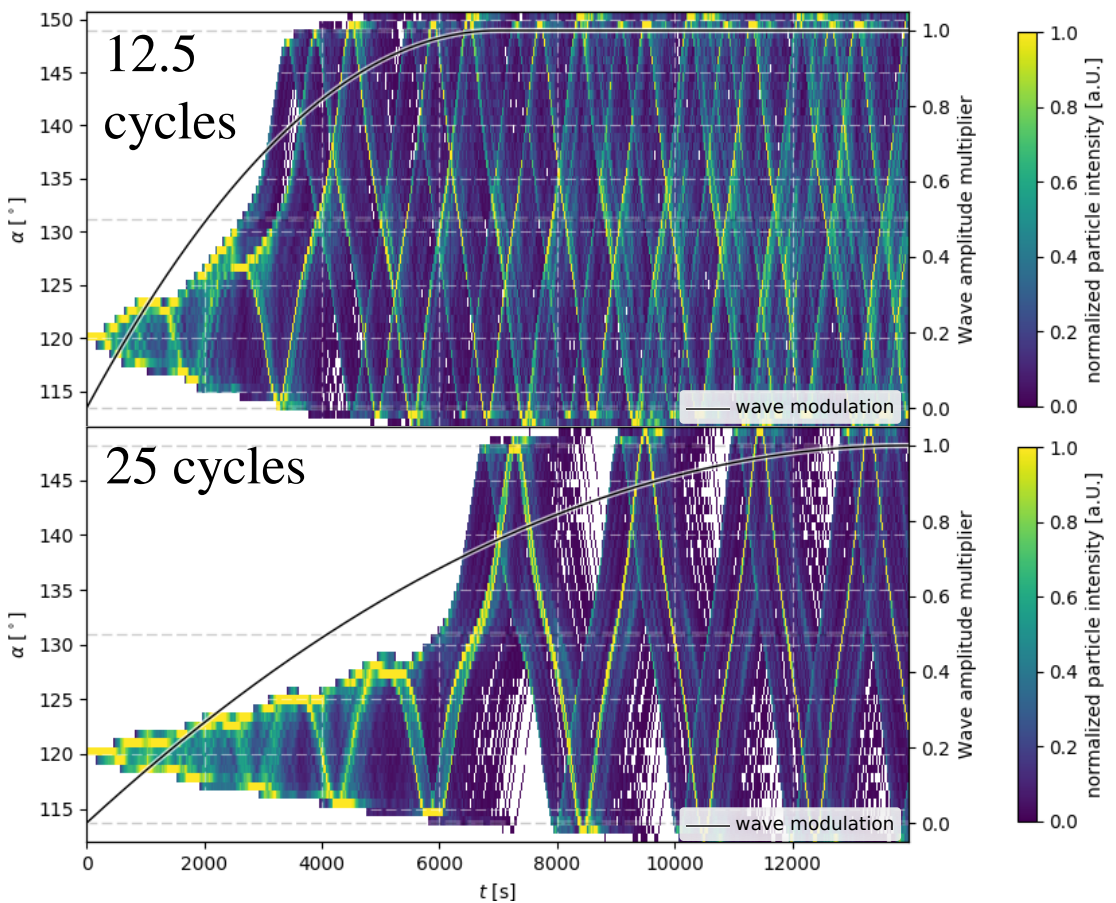


Figure 45: Time evolution of the pitch angle distribution for two time periods of the wave fading in. The time, over which the wave was faded in, is labeled on each panel in the number of wave cycles, that the fading function needed to fade the wave amplitude in. To illustrate the process of wave activation further, the black line with white edges depicts the function, with which the wave has been modulated.

---

ary oscillations in pitch angle space. Hence in the next step the effect of a wave fading out is investigated.

### 5.2.2 Convoluting continuous waves with a deactivation function

To this point, this work focused on, how pitch angle distributions evolve over time under consideration of wave activity. This chapter investigates, how these modified distributions react, when the waves are turned off again.

The simplest (but unrealistic) example for this is, that the wave amplitude suddenly jumps to zero. An example for this can be seen in fig. 46, which depicts the time evolution of a pitch angle distribution exposed to such a wave field. We see, that the pitch angle distribution freezes, after the wave's influence has vanished. This was expected, since the trajectories in pitch angle space during wave activity are a projection of disturbed gyro motions. When the wave has vanished, these disturbances are gone. Thus, regardless of their position in pitch angle space, the particles will continue on undisturbed gyro orbits, which represent a constant pitch angle. So the particles' pitch angle distribution is frozen into a momentary picture of the distribution at the time, when the wave is deactivated. Therefore the distribution observed after the wave has been deactivated is a nonlinear and periodic function of the time, when the wave is turned off.

Similar results are observed, when the process of deactivating the wave takes finite periods of time: Fig. 47 shows pitch angle distributions affected by such waves. Again the pitch angle distributions after the wave has vanished are similar to a momentary picture of the distribution of the moment, when the wave was faded out, but with the modification, that - compared to when the wave is convoluted with a deactivating step function - the most prominent pitch angles in the end pitch angle distribution appear less distinct. In fig. 46 the pitch angles corresponding to the most prominent trajectories at the moment of deactivation are represented through maxima in the particle intensity, which become smoother, when the deactivation of the wave takes significantly longer.

Also, when the process of convoluting the wave with a deactivation function takes longer periods of time, the distribution is modified by pitch angle focusing (compare chapter 2.3.1), since the particles experience a decreasing total magnetic field. Hence the pitch angle distributions become narrower, while the wave decreases in amplitude.

This narrowing of the distribution may also be explained by the fact, that the particles' time-dependent behavior is transitioning smoothly into the state of frozen pitch angles by performing pitch angle distributions of decreasing frequencies and amplitudes, while the wave is fading. When the wave fades over sufficiently long periods of time (like shown in fig. 47 for 8 or 16 wave cycles), the time scale of fading is long enough to effectively make the particles sample the wave as a lower amplitude wave.

In conclusion we have seen, that a wave being shut down mainly causes a pitch angle distribution to freeze to a momentary picture of the distribution of the moment, when the wave is deactivated, but with the modification of pitch angle focusing, since the particles experience a decreasing total magnetic field. The shape of the distribution after wave activity has passed is a nonlinear function of the period in time, during which the wave interacts with the particle. When the process of deactivation takes (compared to one wave cycle) low amounts of time, the end pitch angle distribution is an accurate description of the pitch angle distribution of the moment, when the wave is deactivated, but when the deactivation takes longer periods in time (compared to one wave cycle) the momentary picture becomes more similar to a superposition of the pitch angle distributions integrated over the period in time, when the wave is fading out.

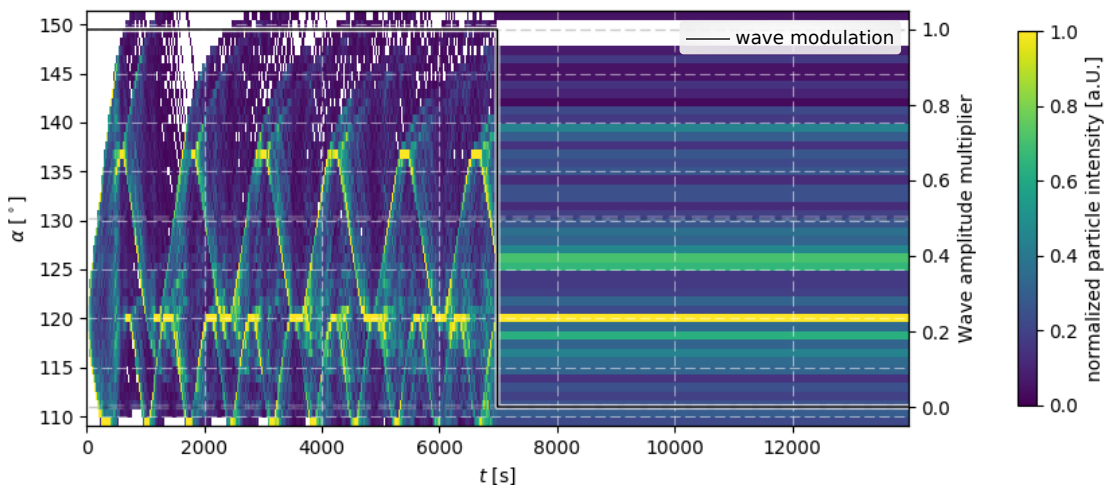


Figure 46: Time evolution of a wave-influenced torus distribution with an initial pitch angle of  $120^\circ$  for a wave turned off instantly during the simulation. The black and white shaded curve represents the factor, with which the wave field was multiplied before being superimposed to the background field (compare chapter 3.2.2).

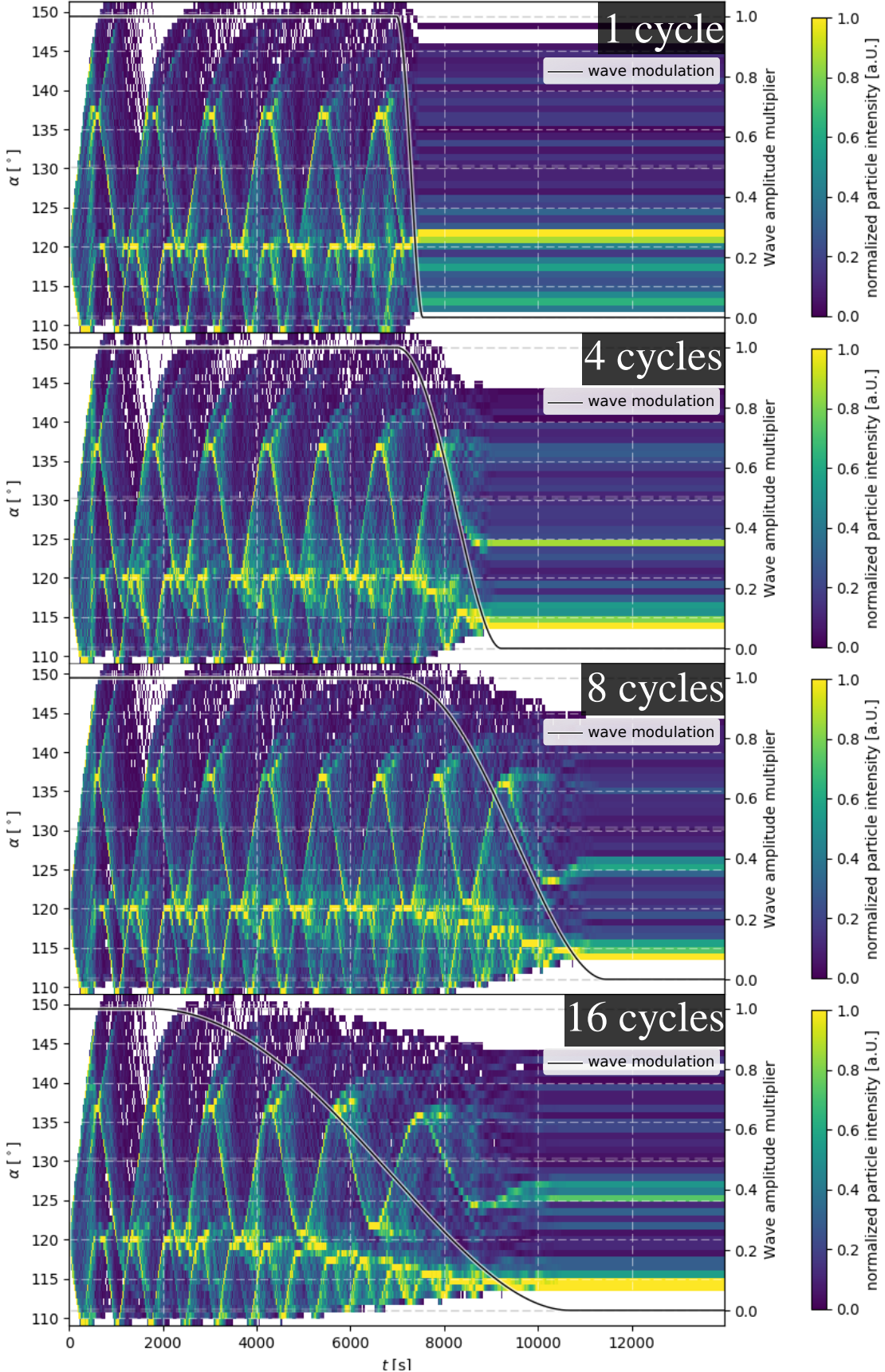


Figure 47: Time evolution of pitch angle distributions exposed to wave fields faded out over various periods of time. The time periods that the deactivation of the wave has needed are labeled in each panel. To illustrate the process of wave deactivation further, the black line with white edges depicts the function, with which the wave has been modulated.

---

### 5.2.3 Intermittent wave fields

Now, that the effects of a wave being activated and deactivated to a pitch angle distribution have been studied separately, we proceed with investigating the modification by wave packages passing the particles. This is modeled by turning the waves on and off randomly. We focus on the question, whether this breaks the stationarity of the particles' trajectories in pitch angle space enough to cause pitch angle scattering.

We now present the results of a simulation being run with a wave with an amplitude of 0.121 nT and a frequency of 0.28  $\omega_{c,O}$  affecting a torus distribution of 120° initial pitch angle over a time of 5000 wave cycles. The pitch angle distribution's time evolution over the first 50 wave cycles is depicted in fig. 48, which shows, that the pitch angle distribution is becoming broader over time. In the time periods, when the wave is remaining turned on, we see the particles performing stationary oscillations in pitch angle space similar to those observed in chapter 5.1. Now when the wave activity pauses the particle distribution is frozen (consistent with chapter 5.2.2), so that the next time, when the wave is turned on again (the wave starting phase is chosen randomly every time the wave starts to fade in), the frozen pitch angle distribution is the boundary condition for interaction with the next wave. So each new wave being faded in interacts with a different mix of torus distributions. That mix is created nonlinearly and randomly, since the time, each wave remains active, is chosen randomly. A wave interacting with particles distributed on different torus distributions also means, that all particles act upon different initial Doppler shifted wave frequencies. Therefore each time the wave pauses and continues the pitch angle distribution broadens, because a lot of different behaviors are mixed, which on their own are the stationary oscillations in pitch angle similar to chapter 5.1.

The broadening effect of the intermittent waves can be seen more impressively in fig. 49, where the pitch angle distribution is depicted over the full run of the simulation. Yet, the timescale, on which the broadening of the distribution happens, is comparatively small. At the last bin of fig. 49 a time of  $\sim 180 \cdot 100 \cdot 2\pi / \omega_{c,O} = 3.75 \cdot 10^6$  s ( $\sim 43$  days) has passed. In comparison to that a solar wind package moving constantly at 450 km/s has traveled  $\sim 11.3$  AU during that time. So the time scales, on which the observed broadening in pitch angle occurs, is relatively slow: Studies, that observed a torus distribution of He<sup>+</sup> PUIs [e.g. Drews et al. (2015)] measured a significantly broadened pitch angle distribution at 1 AU. For oxygen PUIs no direct measurement of a PUI torus exists. It is generally assumed, that pitch angle scattering from wave particle interactions can broaden pitch angle distributions on swift time scales compared to the transport of the solar wind from the Sun to 1 AU [e.g. Drews et al. (2015)]. However, the boundary conditions were also set to ab-initio values and only the passing of mono frequent waves was observed, which makes this study a qualitative approach to wave particle interactions.

Since the standard approach to wave particle interactions is a description by diffusion processes in pitch angle cosine  $\mu$  space (compare chapter 2.4.3), the pitch angle diffusion coefficient  $\langle (\Delta\mu)^2 \rangle / \Delta t$  has been calculated from every  $y$ -slice of fig. 49. Its time evolution is depicted in fig. 50, where it can be seen, that the coefficient starts at high values, but quickly decreases, as time progresses in the first 2000 gyro periods. The general trend is similar to a hyperbola, so that it seems to reach a value close to 0 asymptotically. This fits the evolution of fig. 49, where the distribution first broadens swiftly and then changes slower, as the average pitch angle approaches 90°. Yet the time evolution of the calculated diffusion coefficient also shows, that it is problematic to compare this study to the diffusion approach of quasi-linear theory. The average pitch angle changes over time and quasi-linear theory (compare chapter 2.4.3) predicts, that the diffusion coefficient is a function of the pitch angle, which may have influenced the time evolution of the calculated diffusion coefficient. So in conclusion this parameter is inadequate for the purpose of this study.

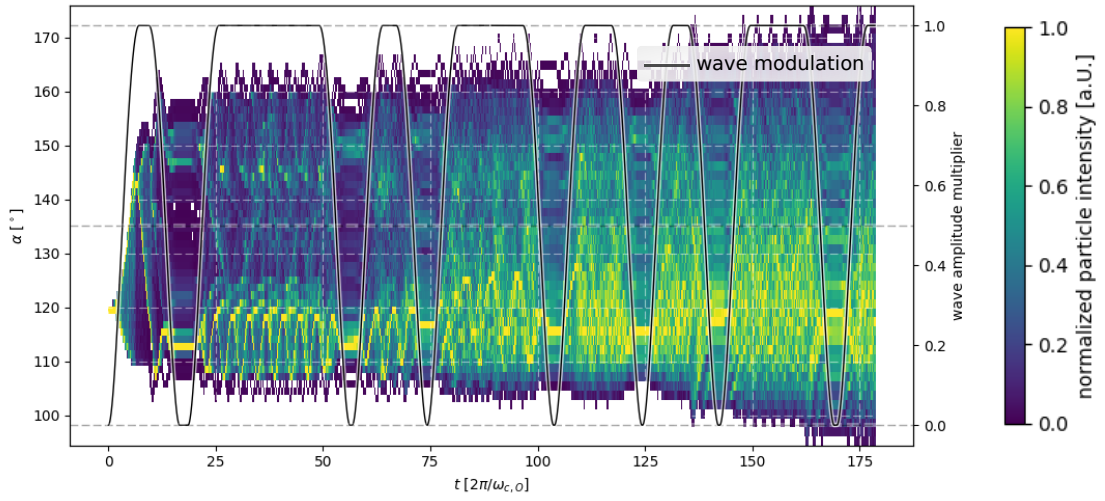


Figure 48: Time development of the pitch angle distribution under the influence of an intermittent wave. The first 50 wave cycles of the simulation are plotted. The left y-axis corresponds to the particles' pitch angle, while the right y-axis corresponds to the solid black line and denotes the modulation of the wave amplitude.

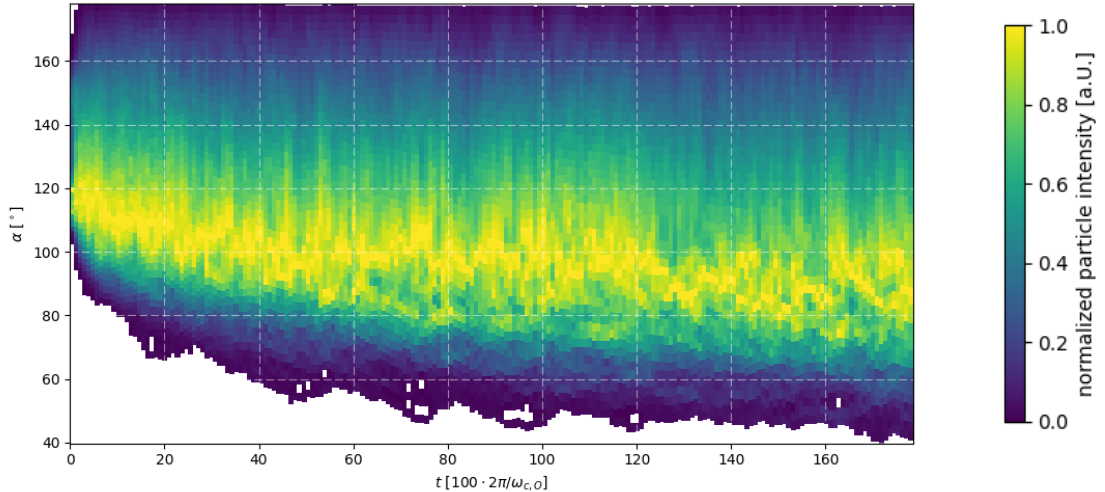


Figure 49: Time development of the pitch angle distribution under the influence of an intermittent wave. We observe the pitch angle distribution to broaden significantly over time.

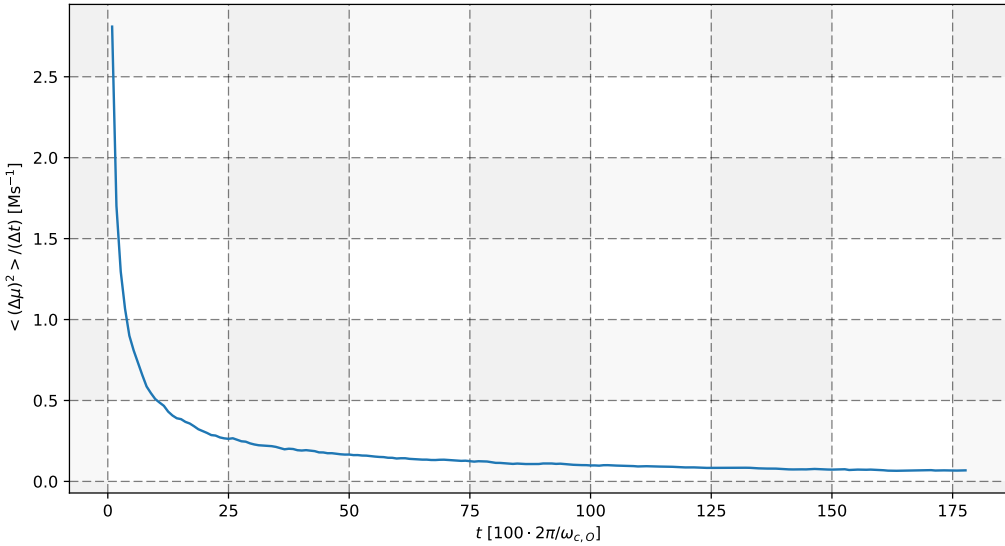


Figure 50: Time evolution of the pitch angle diffusion coefficient calculated from fig. 49. The diffusion coefficient decreases quickly at first and then seems to approach 0 asymptotically for  $t \rightarrow \infty$ .

#### 5.2.4 Parameter studies for intermittent wave fields

This section aims to investigate, how the broadening of the pitch angle distribution is affected by the wave amplitude, the initial pitch angle, the time period, during which the wave packages are activated or deactivated and the wave frequency.

##### Wave amplitude

We start the parameter study with the wave amplitude. Therefore the simulation from chapter 5.2.3 was performed multiple times featuring a different wave amplitude each time. The pitch angle distribution of the last respective 25 wave cycles of each of these simulation runs is then investigated (the start distribution is once again a torus distribution of  $120^\circ$  initial pitch angle). Fig. 51 shows the standard deviation of these end pitch angle distributions as a function of the applied wave amplitude. As expected the standard deviation increases, when the wave amplitude increases. This is also consistent with the results of chapter 5.1.5, where the amplitude-dependent effect of continuous waves on a torus distribution was investigated. The overall reaction of the particles to the wave is stronger, when the wave-inflicted force to the particles (which is through coupling of electric and magnetic field directly proportional to the wave amplitude) is increased.



Figure 51: Standard deviation of the pitch angle distribution of the last 25 wave cycles of simulations run through 5000 wave cycles as a function of the wave amplitude. The standard deviation increases with wave amplitude.

---

## Starting pitch angle

So far this study has only considered an initial pitch angle of  $120^\circ$ . Therefore, as a measure for the end pitch angle distribution of a series of simulations featuring 2500 wave cycles of a wave with an amplitude of 0.1 nT, the time averaged pitch angle distribution of the last 25 wave cycles is investigated, where the initial pitch angle of the test particles is varied on linear bins between  $90^\circ$  and  $180^\circ$ . The result of this is depicted in fig. 52. There the end pitch angle distribution varies insignificantly as a function of the start pitch angle. There are fluctuations in the end pitch angle distributions, but because of the random nature of the simulation setup, more data would be needed in order to attribute these fluctuations to systematic effects. But for now it can be denoted, that the qualitative behavior of the distributions remains the same for varying pitch angles.

Yet it is interesting, that the end pitch angle distributions shown in the plot tend to collect most particles near a pitch angle of  $90^\circ$ . This is consistent with quasi-linear theory of wave particle interactions, which predicts that pitch angle diffusion is weakest for particles at  $90^\circ$ , so that particles at  $90^\circ$  pitch angle are trapped at this angle (compare chapter 2.4.3).

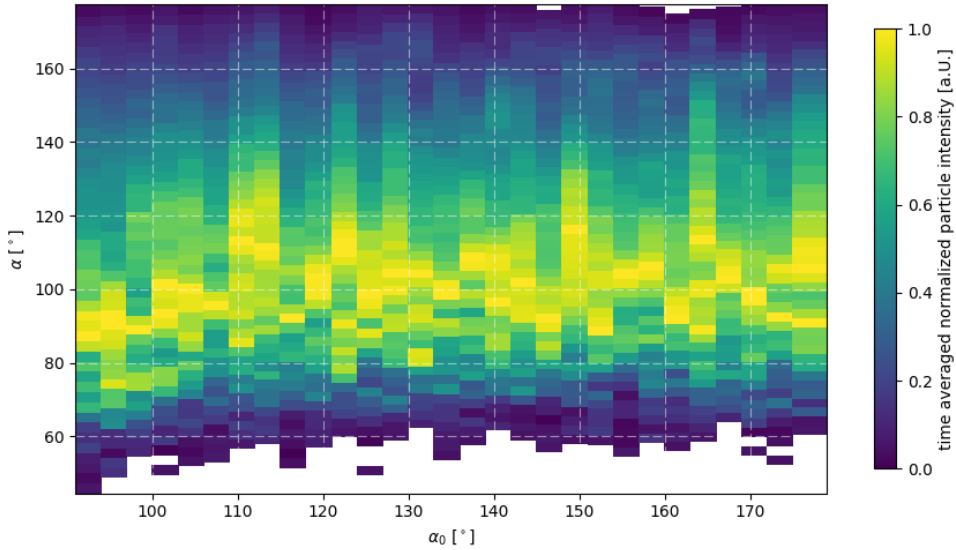


Figure 52: Time averaged pitch angle distribution of simulations of 2500 wave cycles as a function of the initial pitch angle. Each different initial pitch angle represents a new run of the simulation. The time average has been taken from the last 25 wave cycles of each simulation in order to acquire a measure for the end pitch angle distribution of each simulation.

#### Time, during which the wave is faded in or faded out

Now the time period, during which the waves are faded in or out, respectively, is investigated. Again, the end pitch angle distribution after 2500 wave cycles (modeled by a time average of the pitch angle distributions of the last 25 wave cycles of the simulation) is investigated. It is plotted as a function of the length of the time period, that fading the wave in and out takes, in fig. 53. We see, that the pitch angle distribution decreases in width, when the duration of the time period, during which the wave is activated or deactivated, increases. This is due to two effects: On the one hand (as seen in chapter 5.2.1) the particles sample a lower-amplitude wave, when the wave is activated over longer time periods. Therefore they interact less time with a full-amplitude wave. On the other hand the results of chapter 5.2.2 showed, that when convolving the wave with a deactivation function over longer time periods, the pitch angle distribution is focused and therefore decreased in broadness. Both effects may create the trend seen in fig. 53. Still it might be useful to see, which of these dominates.

Hence in a second series of simulations the time, that it takes to activate the wave, is decoupled from the time, that it takes to deactivate the wave. Fig. 54 shows the resulting end pitch angle distributions (modeled by a time average of the pitch angle distributions of the last 25 wave cycles of the simulation) as a function of both time periods. The top panel shows the end pitch angle distribution as a function of the fading-in time (the fading-out time was left at the constant value of 1 wave cycle) and the bottom panel shows the analogue for the fading-out time. The trend seen in fig. 53 is less pronounced in both panels of fig. 54. Still it can be observed (especially when considering fading times beyond  $\sim 3$  wave cycles), that the broadness of the end pitch angle distribution decreases, when the activation or deactivation of the waves takes longer. It can also be seen, that the magnitudes, by which the pitch angle distributions are broadened, are very similar to each other in both panels of fig. 54.

Therefore it can be noted, that the broadening effect, which intermittent waves have towards

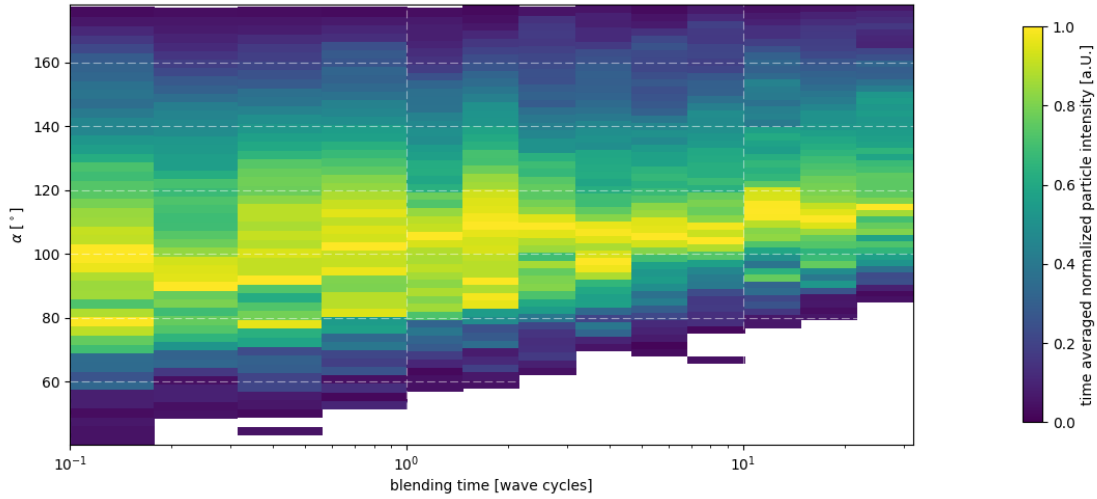


Figure 53: Time averaged pitch angle distribution of the last 25 wave cycles of simulations of 2500 wave cycles as a function of the duration of the time period (called blending time in the plot), during which the wave is convoluted with an activation -or deactivation function. The width of the end pitch angle distribution decreases in width, when the blending time increases.

pitch angle distributions is weaker, the longer it takes to activate or deactivate the wave.

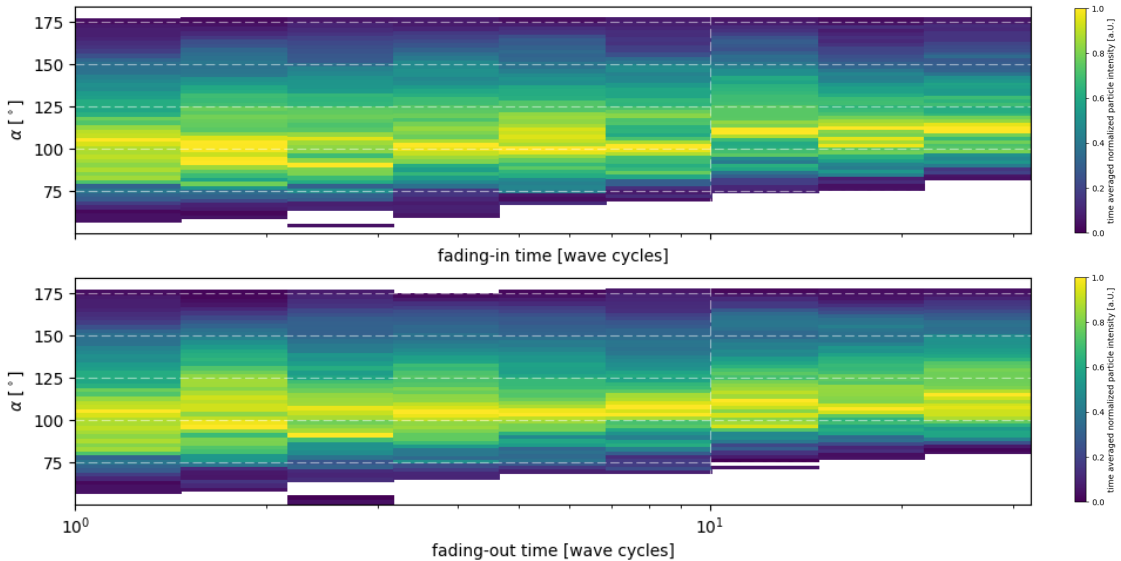


Figure 54: Time averaged pitch angle distributions of the last 25 wave cycles of simulations run through 2500 wave cycles as a function of the time, that (top panel) it takes to fade the wave in, and of the time, that (bottom panel) it takes to fade the wave out. The fading-out time was chosen to be 1 wave cycle for all distributions depicted in the top panel and the fading-in time was set to 1 wave cycle for all distributions shown in the bottom panel. The pitch angle distributions of both plots show a similar trend to fig. 53.

## Wave frequency

The last parameter to be studied here is the frequency of the waves fed into the simulation. Following the approach used to study the other parameters simulations were run with different frequencies to obtain end pitch angle distributions. These were obtained by averaging the pitch angle distributions observed in the last 25 wave cycles of 2500 simulated wave cycles over time. Fig. 55 shows these distributions as a function of the Doppler shifted wave frequency (The Doppler shifted frequency is calculated with respect to the particles' initial velocity). For Doppler-shifted frequencies higher than the particle's gyro frequency the pitch angle distribution reacts less to the wave with increasing distance to the the gyro frequency. The pitch angle distribution becomes smaller in width and is centered around the initial pitch angle of  $120^\circ$  at that frequency regime.

However, in the regime of lower frequencies ( $\omega_d \ll \omega_{c,O}$ ) the end pitch angle distribution is seemingly reaching a state of constant broadness with decreasing frequencies, which can be explained with the results of chapter 5.1.4: In that frequency regime the pitch angle distribution also reached a constant broadness. It was caused by the wave changing the magnetic field slow enough to let the torus distribution adapt to the wave field, as if it were a background field, which means that the torus rotates slowly and together with the wave magnetic field. The maximum absolute pitch angle change caused by that is given by  $\delta\alpha = \arctan(\delta B/B)$ . From chapter 5.2.2 it is known, that the pitch angle distribution is frozen in time, when the wave is faded out. So after the first time the wave is faded in, the particles are at maximum apart by  $2\delta\alpha$  in pitch angle space. When then the wave is faded out this state is (apart from focusing of the distribution) frozen until the next wave comes through. This means, that in total the particles are scattered in pitch angle space by a frequency-independent magnitude, since the spread in pitch angle caused by a continuous wave is in this frequency regime  $2\delta\alpha$ .

---

We now consider frequencies close to the cyclotron frequency. There the pitch angle distribution wanders from average pitch angles of  $\sim 120^\circ$  at a frequency of  $\sim 0.6\omega_{c,O}$  down to average pitch angles in the range of  $80^\circ \dots 90^\circ$  at a frequency of  $\sim 1.2\omega_{c,O}$ . At exactly the cyclotron frequency the average pitch angle is  $\sim 90^\circ$ . At the same time the broadness of the distribution remains nearly constant.

Particles scattered towards values of  $90^\circ$  is something, that quasi-linear theory would expect, since there pitch angle diffusion reaches a minimum and particles at  $90^\circ$  are trapped (compare chapter 2.4.3). Considering a pitch angle of  $90^\circ$  from a kinetic point of view we find, that the parallel velocity vanishes there and all a particle's energy is in the perpendicular component. This also means, that the particle is far away from first order resonance (the absolute wave frequency would need to be exactly  $\omega_{c,O}$ ).

Still it is interesting from a kinetic point of view, why the particles seem to gather around  $\sim 90^\circ$  at this frequency regime. That the average pitch angles for  $\omega_d$  between  $\sim 1\omega_{c,O}$  and  $\sim 1.2\omega_{c,O}$  are lower than  $120^\circ$  corresponds to the branch structure observed in chapter 5.1.4 and further investigated in chapter 5.1.5, where a large fraction of the particles performed trajectories, which went considerably lower than  $120^\circ$  at these frequencies. From the relation between pitch angle and the Doppler shifted frequency derived in appendix D we know, that the frequency decreases, when the pitch angle is decreased during the interaction between wave and particle. So when the wave is faded out and back in again all particles scattered to lower pitch angles sample the wave at lower frequencies than before. There the relation between pitch angle and Doppler shifted frequency is less curved and steeper (compare fig. 63 of appendix D), so that a smaller change in pitch angle causes a bigger change in the Doppler-shifted frequency. Still the studies of chapter 5.1.4 predict, that a particle sampling frequencies slightly lower than the resonance frequency would (probably) be increased in pitch angle, but once the particle is put towards higher pitch angles (e.g.  $160^\circ$ ) the relation between pitch angle and Doppler shifted frequency is more curved and less steep, so that at these pitch angles one needs to increase the pitch angle considerably to get the particle out of the branch structure in the direction of higher frequencies. This may also explain, why the particles are scattered towards lower pitch angles for  $\omega_d$  between  $\sim 0.6\omega_{c,O}$  and  $\sim 1\omega_{c,O}$ , which is contrary to the observations of chapter 5.1.4.

However, this is more a working theory, than an explanation. The phenomenological observation is, that particles in the frequency regime of  $\omega_d$  close to  $\omega_{c,O}$  are lowered in pitch angle and seem to reach an average pitch angle of  $\sim 90^\circ$ , when the waves are turned on and off randomly. There seems to be a selective effect, when turning the waves on and off, that dampens pitch angle scattering towards higher pitch angles. But this effect is yet to be identified.

### 5.2.5 Scattering of the particle energy

So far the interactions of the pickup ions with waves have always been observed in pitch angle space. However, the fact, that the particles are scattered in pitch angle space, raises the question, whether this is connected to an individual energy gain or loss of the particles. The absolute particle energy in the wave frame is conserved (compare chapter 2.4), but the particle energy in the solar wind bulk frame is therefore not necessarily conserved.

Fig. 56 shows the evolution of the particle energy distribution over time for the simulation presented in chapter 5.2.3. It can be seen, that the particle energy is scattered to energies ranging from 0.8 to 1.8 of the particles' initial energy. Towards energies higher than the initial energy the resulting end distribution fades out smoothly. Yet, towards lower energies a distinct cutoff of the observed particle energies is observed at  $\sim 0.8$  of the particles' initial energy. This is explainable by the deliberations made in appendix C, where it has been stated, that the particle energy is a monotonic function of the momentary particle's pitch angle, determined by the particle's initial pitch angle and energy. Fig. 62 plots this function for selected initial pitch angles. In the situation leading to fig. 56 the initial pitch angle is  $120^\circ$ . For that angle the curve

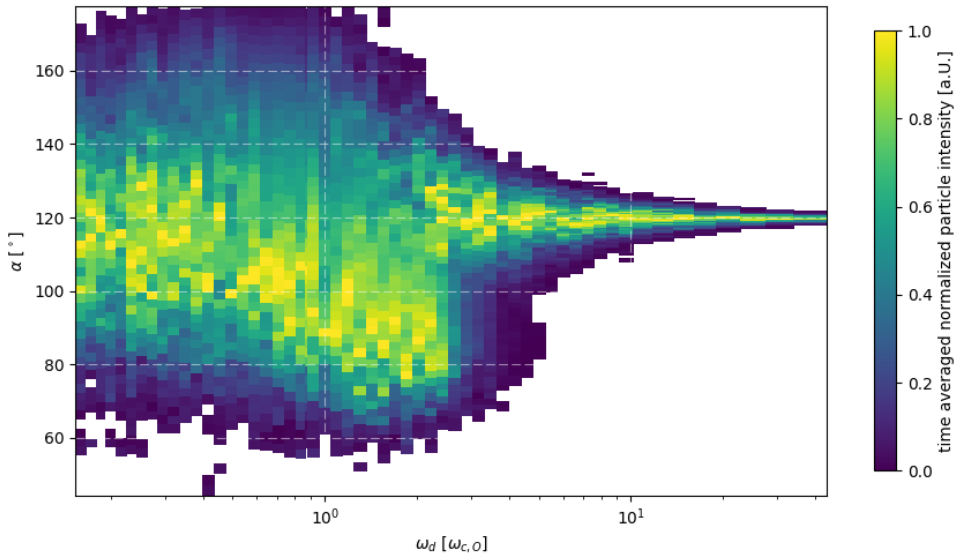


Figure 55: Time averaged pitch angle distribution of the last 25 wave cycles of simulations of 2500 wave cycles as a function of the wave frequency. Each wave frequency represents a single run of a simulation.

of energy depicted in fig. 62 decreases with increasing pitch angle, but becomes less steep and finally reaches a value close to 0.8 asymptotically, which explains the energy cutoff.

Also toward higher energies a cutoff can be found in the curve (in the case of  $\alpha \rightarrow 0^\circ$  the curve reaches  $\sim 1.9$  asymptotically) of energy, but the particles of fig. 56 do not reach such a high energy, which is why this cutoff is not observed. With  $120^\circ$  the particles start at an energy much closer to the lower energy cutoff.

It is evident, that the lowest energies correspond to very high pitch angles, which then correspond to a high fraction of parallel velocity versus perpendicular velocity. So at these energies almost all energy is mapped into the parallel velocity, which means, that particles at these energies have parallel velocities, that map the Doppler shifted frequency towards very high frequencies, where the particles interact weakly with the wave. So once the particles have reached these energies, they are unlikely to be scattered much, which means, that they likely remain at these energies.

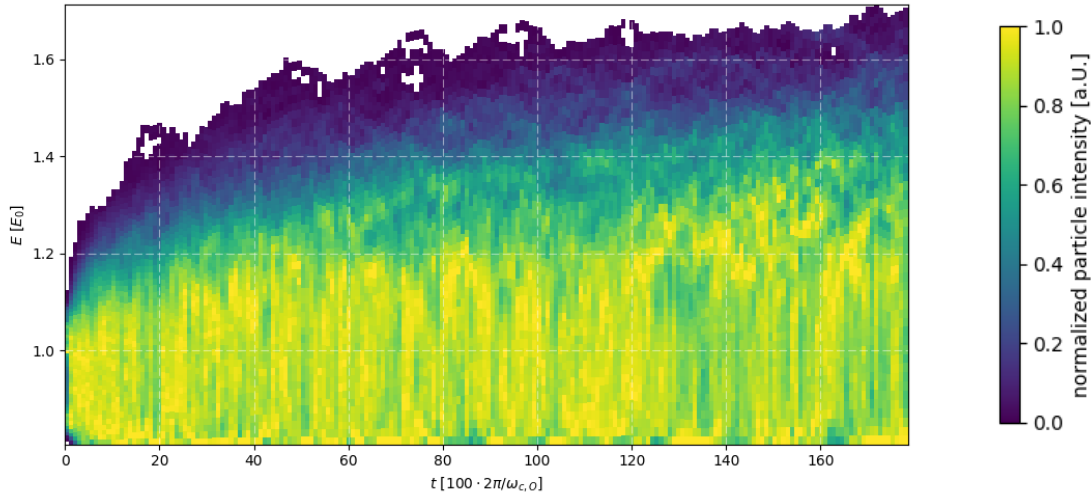


Figure 56: Time evolution of the energy distribution of the particles from chapter 5.2.3 in units of a particle's initial energy. The time evolution of the corresponding pitch angle distribution can be seen in fig. 49.

## 6 Conclusions

In this work a qualitative numerical study has been performed to gain a basic understanding of wave particle interactions between pickup ions and alfvénic waves on a microscopic level and on timescales, where the trajectories of single particles can be observed. This has been done with special focus to the questions, whether pitch angle scattering can be observed with this approach and which is the minimal condition necessary to observe pitch angle scattering.

It has been observed, that the interactions of particles with single continuous mono frequent waves do not cause pitch angle scattering in the sense of a systematic broadening of the pitch angle distribution over time. The particles are forced onto stationary oscillatory trajectories in pitch angle space. The qualitative behavior of these trajectories (pitch angle amplitude, oscillation frequency, shape) is generally a nonlinear and highly-complex function of the boundary conditions, especially of the wave amplitude, Doppler shifted wave frequency and initial phase difference between particle gyration and wave oscillation. By picking example situations the qualitative influence of these parameters has been disentangled.

Yet, in a real situation it is not expected to observe continuous waves [e.g. Tu and Marsch (1995)]. So as a second study the reaction of pickup ions to intermittent wave fields has been investigated, where systematic pitch angle scattering has been observed. This scattering becomes stronger with increasing wave amplitude. In agreement with quasi-linear theory the end pitch angle distributions (after being exposed to intermittent waves over a long time) seem to reach a state with a mean value of  $90^\circ$  preferredly, that is, at least, when the Doppler shifted wave frequency is chosen at values close to the particles' gyro frequency. For very high wave frequencies the particles generally react weakly to the waves and at lower wave frequencies, they seem to reach a behavior independent of the wave frequency, where the pitch angle is distributed with a fixed broadness around the initial pitch angle. In order to prove this claim and the thesis, that the particles seem to preferentially scatter towards  $90^\circ$ , a more systematic investigation is needed.

Lastly it is noteworthy, that the timescales, during which the pitch angles are scattered, are too high compared to what one would expect from real pickup ion data. Studies, which observed PUI velocity space distributions [e.g Drews et al. (2015), Drews et al. (2016)], observed significantly broadened pitch angle distributions at 1 AU and it is generally assumed, that the

---

time scale for pitch angle scattering through wave particle interactions is very fast compared to the transport of the solar wind from the Sun to 1 AU [e.g. Drews et al. (2015)]. That this study observed pitch angle scattering on larger time scales may be due to the fact, that in a real situation the investigated wave particle interactions are superimposed to other effects like stochastic collisions with solar wind particles [e.g. Fahr and Fichtner (2011)]. It is also due to the fact, that many of the boundary conditions for the performed simulations were chosen as ab-initio values, which is sometimes due to a lack of an experimental value and sometimes in order to resolve the observed effects properly.

Still the qualitative study of wave particle interactions between alfvénic waves and pickup ions and especially the approach to investigate the interactions in systems as simple as possible has revealed interesting effects and is also a foundation for future studies, which may disentangle in detail, which processes in the solar wind are responsible for scattering of pitch angle distributions.

---

## 7 Outlook

In the solar wind several effects are superimposed, that may systematically broaden pitch angle distributions over time, to those studied in this work [e.g. Drews et al. (2015)]. The main result of this work is, that continuous mono frequent waves alone can not broaden a typical PUI pitch angle distribution over time. They need to appear in combination with other effects. The effect studied in this work, was the passing of wave packages by activating and deactivating the waves randomly. Still, in the real solar wind other effects may significantly broaden the pitch angle distribution in combination with waves.

E.g. collisions of the pickup ions with solar wind particles introduce a stochastic modification of the particles' velocities and may therefore already broaden the pitch angle distribution without wave activity [e.g. Fahr and Fichtner (2011)]. It may be interesting to investigate with this work as a foundation, whether wave activity accelerates the collision-caused broadening of the pitch angle distribution.

As the particles are transported by the solar wind, they gain radial distance to the Sun. So the background magnetic field, that the particles experience, is expected to change slowly over time in strength and direction (compare chapter 2.1). In this study it has been observed, that when the magnetic field conditions, which the particles experience, change very slowly compared to the particles' gyro frequency, the particles will just adapt slowly to the new conditions, while keeping their respective pitch angle to the total magnetic field. A combination of that effect together with faster wave activity (at a timescale similar to the particles' gyro frequency) may prove to be an interesting study.

In the approximation of the Parker spiral (compare chapter 2.1) a curvature and a radial field gradient are dominating the heliospheric magnetic field. Such a gradient may also influence the observations of this study significantly, since, as the test particles move through simulation space, the particles' gyro frequency (compare chapter 2.4.1) and the alfvénic speed (compare chapter 2.3.3) change. It also means, that an additional magnetic mirror force (compare chapter 2.4.1) is introduced, so that the particle's motion becomes more complex. Both effects can be combined by modeling the background magnetic field through the approximation of the Parker spiral (compare chapter 2.1). Appendix E contains work-in-progress notes on how to implement alfvénic waves, that propagate along such a field configuration. However, first test runs, where the Parker spiral and alfvénic waves have been implemented on global scales (particles propagating around  $\sim 1$  AU distance from the Sun) have shown great numerical imprecisions, since a comparatively small change in particle location is added to the distance from the Sun. Therefore different approaches to this problem may be necessary like rotating the magnetic field in dependency of the particle position locally, so that the particle positions do not need to start at values in the magnitude of 1 AU.

Finally, the introduction of the superposition of different wave frequencies might have a broadening effect on the particles, since the more frequencies are fed into the simulation at the same time, the more random the field will appear to the particle. First studies have been conducted in the context of this work, where instead of a whole spectrum of waves, two different wave frequencies have been fed into the simulation. Fig. 57 shows the time-dependent behavior of four particles of an initial  $120^\circ$  torus exposed to two waves of an amplitude of 50 pT and frequencies of  $0.28 \omega_{c,O}$  (slightly below first order resonance) and  $0.38 \omega_{c,O}$  (slightly above first order resonance) simultaneously. The solar wind speed is 450 km/s and the background field is 5 nT. We now see trajectories, which are not quite stationary anymore. However, in the particles' trajectories patterns can be identified, which repeat themselves randomly, which is a typical behavior for nonlinear systems.

It is interesting, that when looking at the behavior of the same particles exposed to either of

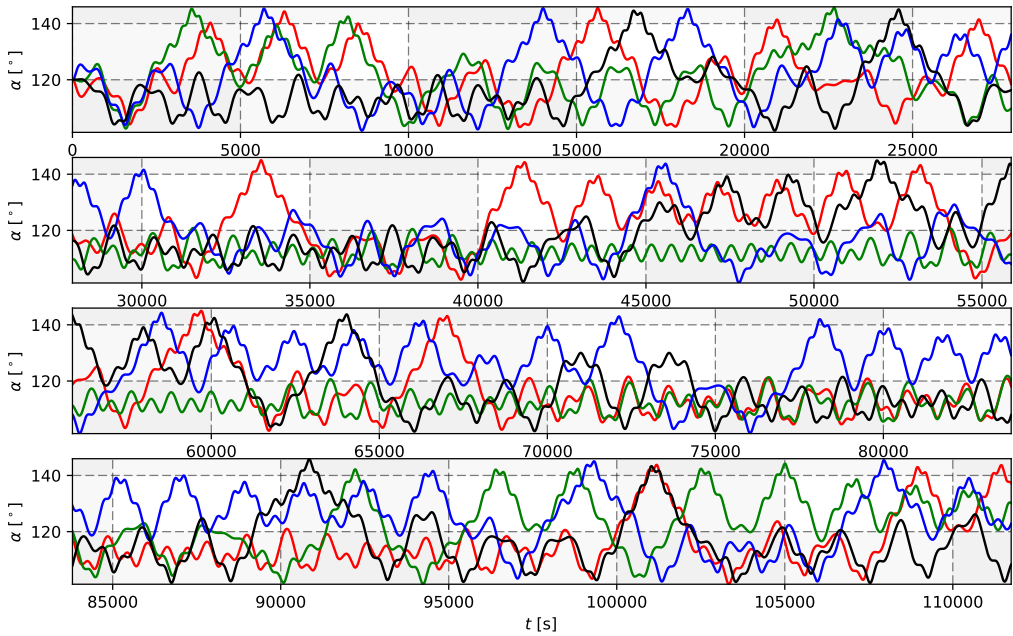


Figure 57: Pitch angle trajectories of four particles initially distributed on a  $120^\circ$  torus distribution exposed to two alfvénic waves with frequencies of  $0.28 \omega_{c,O}$  and  $0.38 \omega_{c,O}$  at the same time.

the frequencies individually (fig. 58 for  $0.28 \omega_{c,O}$  and fig. 59 for  $0.38 \omega_{c,O}$ ), these patterns can be interpreted as arising from the particles randomly changing their behavior from reacting to one frequency to reacting to the other frequency. This once again reveals the nonlinear behavior of wave particle interactions, but as with the results from continuous single-frequency waves, it is not expected, that on longer terms the example two-frequency setup would not increase the broadness of the pitch angle distribution systematically over time. However, the complexity of the trajectories has grown significantly and it is expected, that the behavior of the particles would change drastically, when using different frequency combinations.

All in all the discussed effects would certainly add more realism to the simulation, when superimposed. Yet, they would also produce pitch angle distributions, which are under the influence of such a big parameter space, that similar to real pickup ion data, it would be impossible to disentangle the influence of single effects.

Therefore the qualitative approach of this work, to study possible causes of pitch angle scattering separately, may produce interesting results and probably reveal general trends, that might help understanding real pickup ion velocity distributions in a better way.

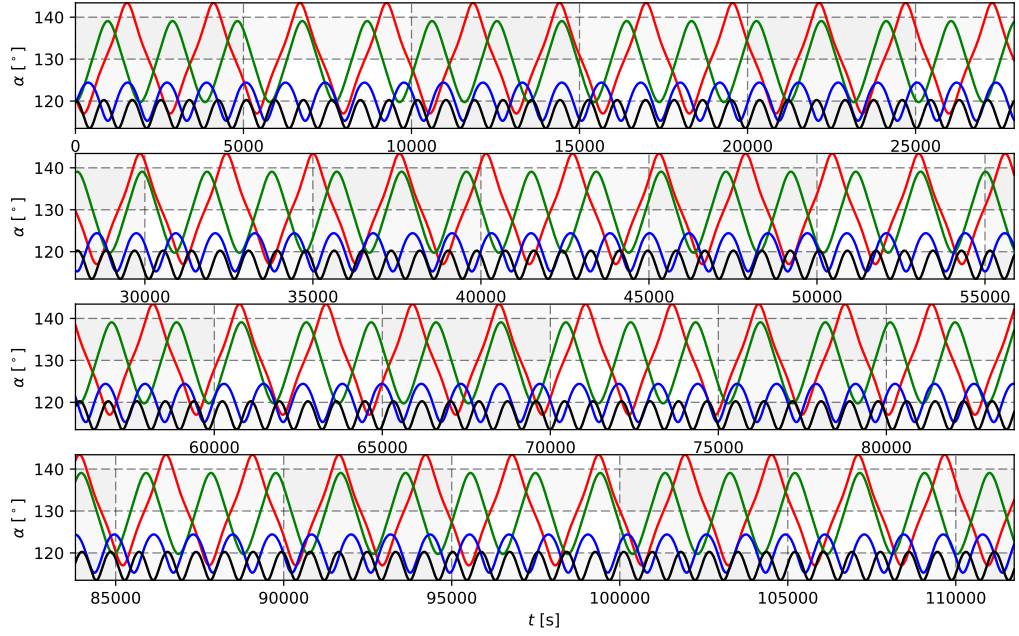


Figure 58: Pitch angle trajectories of four particles initially distributed on a  $120^\circ$  torus distribution exposed to one alfvénic waves with a frequency of  $0.28 \omega_{c,O}$ .

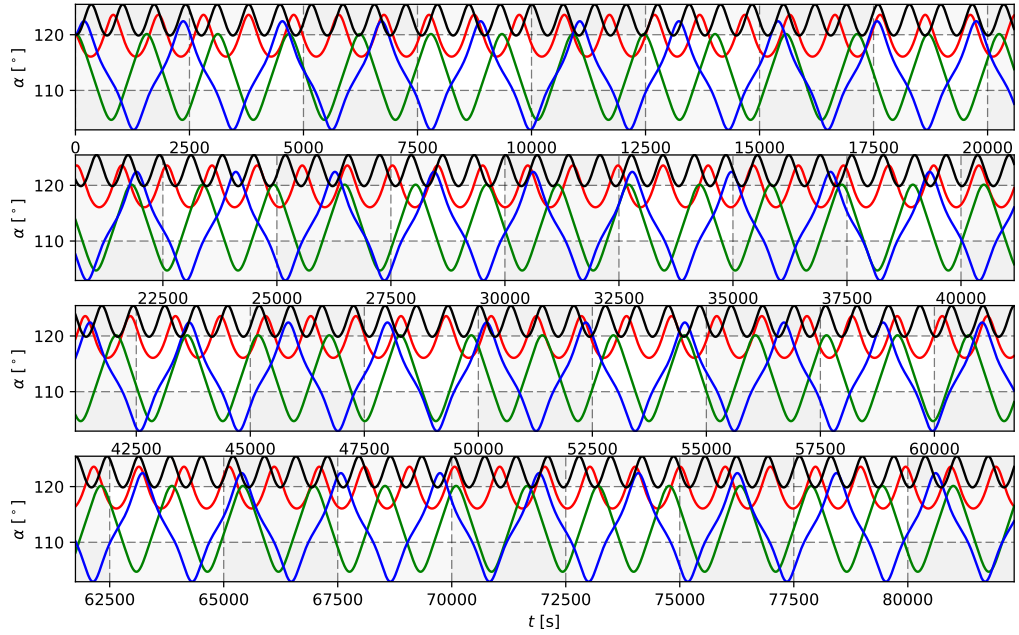


Figure 59: Pitch angle trajectories of four particles initially distributed on a  $120^\circ$  torus distribution exposed to one alfvénic waves with a frequency of  $0.38 \omega_{c,O}$ .

---

## 8 Bibliography

### References

- Alfvén, H., Oct. 1942. Existence of Electromagnetic-Hydrodynamic Waves. *Nature*150, 405–406.
- Bärwolff, G., 2015. Numerik für Ingenieure, Physiker und Informatiker. Springer Berlin Heidelberg.
- URL <https://books.google.de/books?id=EwGkCgAAQBAJ>
- Baumjohann, W., Treumann, R., 1997. Basic Space Plasma Physics. Imperial College Press.
- URL <https://books.google.de/books?id=e4yupc0zJxkC>
- Beeck, J., Wibberenz, G., Dec. 1986. Pitch angle distributions of solar energetic particles and the local scattering properties of the interplanetary medium. *ApJ*311, 437–450.
- Belcher, J. W., Davis, Jr., L., 1971. Large-amplitude Alfvén waves in the interplanetary medium, 2. *J. Geophys. Res.*76, 3534.
- Birdsall, C., Langdon, A., 2004. Plasma Physics via Computer Simulation. Series in Plasma Physics and Fluid Dynamics. Taylor & Francis.
- URL <https://books.google.de/books?id=S2lqgDTm6a4C>
- Bochsler, P., Kucharek, H., Möbius, E., Bzowski, M., Sokół, J. M., Didkovsky, L., Wieman, S., Jan. 2014. Solar Photoionization Rates for Interstellar Neutrals in the Inner Heliosphere: H, He, O, and Ne. *ApJS*210, 12.
- Bronštejn, I., Musiol, G., Mühlig, H., Semendjaev, K., 2012. Taschenbuch der Mathematik. Deutsch.
- URL <https://books.google.de/books?id=A7B1nAEACAAJ>
- Burlaga, L. F., Ness, N. F., Acuña, M. H., Lepping, R. P., Connerney, J. E. P., Richardson, J. D., Jul. 2008. Magnetic fields at the solar wind termination shock. *Nature*454, 75–77.
- Butz, T., 2013. Fouriertransformation für Fußgänger. Vieweg+Teubner Verlag.
- URL <https://books.google.de/books?id=VX-eBgaAQBAJ>
- Chalov, S. V., Sep. 2014. Helium pickup ion focusing cone as an indicator of the interstellar flow direction. *MNRAS*443, L25–L28.
- Chalov, S. V., Fahr, H. J., Jul. 1998. Phase space diffusion and anisotropic pick-up ion distributions in the solar wind: an injection study. *A&A*335, 746–756.
- Cummings, A. C., Stone, E. C., Steenberg, C. D., Oct. 2002. Composition of Anomalous Cosmic Rays and Other Heliospheric Ions. *ApJ*578, 194–210.
- Drews, C., Berger, L., Taut, A., Peleikis, T., Wimmer-Schweingruber, R. F., Mar. 2015. 2D  $\text{He}^+$  pickup ion velocity distribution functions: STEREO PLASTIC observations. *A&A*575, A97.
- Drews, C., Berger, L., Taut, A., Wimmer-Schweingruber, R. F., Apr. 2016. Anisotropy of the  $\text{He}^+$ ,  $\text{C}^+$ ,  $\text{N}^+$ ,  $\text{O}^+$ , and  $\text{Ne}^+$  pickup ion velocity distribution functions. *A&A*588, A12.
- Drews, C., Berger, L., Wimmer-Schweingruber, R. F., Galvin, A. B., Apr. 2013. Interstellar  $\text{He}^+$  ring-beam distributions: Observations and implications. *Geophys. Res. Lett.*40, 1468–1473.
- Fahr, H. J., Fichtner, H., Sep. 2011. Pick-up ion transport under conservation of particle invariants: how important are velocity diffusion and cooling processes? *A&A*533, A92.

- 
- Florinski, V., Zank, G. P., Heerikhuisen, J., Hu, Q., Khazanov, I., Aug. 2010. Stability of a Pickup Ion Ring-beam Population in the Outer Heliosheath: Implications for the IBEX Ribbon. *ApJ*719, 1097–1103.
- Gurnett, D. A., Kurth, W. S., Burlaga, L. F., Ness, N. F., Sep. 2013. In Situ Observations of Interstellar Plasma with Voyager 1. *Science* 341, 1489–1492.
- Hasselmann, K., Wibberenz, G., Dec. 1970. A Note on the Parallel Diffusion Coefficient. *ApJ*162, 1049.
- Heerikhuisen, J., Pogorelov, N. V., Zank, G. P., Crew, G. B., Frisch, P. C., Funsten, H. O., Janzen, P. H., McComas, D. J., Reisenfeld, D. B., Schwadron, N. A., Jan. 2010. Pick-Up Ions in the Outer Heliosheath: A Possible Mechanism for the Interstellar Boundary EXplorer Ribbon. *ApJ*708, L126–L130.
- Isenberg, P. A., Apr. 2005. Turbulence-driven Solar Wind Heating and Energization of Pickup Protons in the Outer Heliosphere. *ApJ*623, 502–510.
- Jokipii, J. R., Nov. 1966. Cosmic-Ray Propagation. I. Charged Particles in a Random Magnetic Field. *ApJ*146, 480.
- Kallenbach, R., Geiss, J., Gloeckler, G., von Steiger, R., Oct. 2000. Pick-up Ion Measurements in the Heliosphere - A Review. *Ap&SS*274, 97–114.
- Keilbach, D., 2015. Verschiebung des Focusing-Cones von He + -Pickup-Ionen anhand von Transporteffekten in der Heliosphäre: STEREO PLASTIC Beobachtungen. B.Sc. thesis.
- Kennel, C. F., Engelmann, F., Dec. 1966. Velocity Space Diffusion from Weak Plasma Turbulence in a Magnetic Field. *Physics of Fluids* 9, 2377–2388.
- Lehe, R., Parrish, I. J., Quataert, E., Dec. 2009. The Heating of Test Particles in Numerical Simulations of Alfvénic Turbulence. *ApJ*707, 404–419.
- McComas, D. J., Alexashov, D., Bzowski, M., Fahr, H., Heerikhuisen, J., Izmodenov, V., Lee, M. A., Möbius, E., Pogorelov, N., Schwadron, N. A., Zank, G. P., Jun. 2012. The Heliosphere's Interstellar Interaction: No Bow Shock. *Science* 336, 1291.
- McComas, D. J., Barraclough, B. L., Funsten, H. O., Gosling, J. T., Santiago-Muñoz, E., Skoug, R. M., Goldstein, B. E., Neugebauer, M., Riley, P., Balogh, A., May 2000. Solar wind observations over Ulysses' first full polar orbit. *J. Geophys. Res.*105, 10419–10434.
- McComas, D. J., Bzowski, M., Fuselier, S. A., Frisch, P. C., Galli, A., Izmodenov, V. V., Katushkina, O. A., Kubiak, M. A., Lee, M. A., Leonard, T. W., Möbius, E., Park, J., Schwadron, N. A., Sokół, J. M., Swaczyna, P., Wood, B. E., Wurz, P., Oct. 2015. Local Interstellar Medium: Six Years of Direct Sampling by IBEX. *ApJS*220, 22.
- Möbius, E., Bzowski, M., Chalov, S., Fahr, H.-J., Gloeckler, G., Izmodenov, V., Kallenbach, R., Lallement, R., McMullin, D., Noda, H., Oka, M., Pauluhn, A., Raymond, J., Ruciński, D., Skoug, R., Terasawa, T., Thompson, W., Vallerga, J., von Steiger, R., Witte, M., Nov. 2004. Synopsis of the interstellar He parameters from combined neutral gas, pickup ion and UV scattering observations and related consequences. *A&A*426, 897–907.
- Möbius, E., Lee, M. A., Drews, C., Dec. 2015. Interstellar Flow Longitude from the Symmetry of the Pickup Ion Cut-off at 1 AU. *ApJ*815, 20.
- Möbius, E., Lee, M. A., Gloeckler, G., Drews, C., Keilbach, D., Nov. 2016. Interstellar flow longitude from pickup ion cut-off observations at 1 AU with STEREO and ACE. In: *Journal of Physics Conference Series*. Vol. 767 of *Journal of Physics Conference Series*. p. 012017.

- 
- Moebius, E., Hovestadt, D., Klecker, B., Scholer, M., Gloeckler, G., Dec. 1985. Direct observation of He(+) pick-up ions of interstellar origin in the solar wind. *Nature* 318, 426–429.
- Moebius, E., Rucinski, D., Hovestadt, D., Klecker, B., Dec. 1995. The helium parameters of the very local interstellar medium as derived from the distribution of  $\text{He}^{++}$  pickup ions in the solar wind. *A&A* 304, 505.
- Parker, E. N., Nov. 1958. Dynamics of the Interplanetary Gas and Magnetic Fields. *ApJ* 128, 664.
- Piel, A., 2010. Plasma Physics: An Introduction to Laboratory, Space, and Fusion Plasmas. Springer Berlin Heidelberg.  
URL <https://books.google.de/books?id=wWlQ4Qz5hcwC>
- Prölls, G., 2003. Physik Des Erdnahen Weltraums: Eine Einführung. Physics and astronomy online library. Springer Berlin Heidelberg.  
URL <https://books.google.de/books?id=HQFczuPMqtUC>
- Roelof, E. C., 1969. Propagation of Solar Cosmic Rays in the Interplanetary Magnetic Field. In: Ögelman, H., Wayland, J. R. (Eds.), *Lectures in High-Energy Astrophysics*. p. 111.
- Ruciński, D., Cummings, A. C., Gloeckler, G., Lazarus, A. J., Möbius, E., Witte, M., Oct. 1996. Ionization processes in the heliosphere - Rates and methods of their determination. *Space Sci. Rev.* 78, 73–84.
- Schatten, K. H., Wilcox, J. M., Ness, N. F., Mar. 1969. A model of interplanetary and coronal magnetic fields. *Sol. Phys.* 6, 442–455.
- Scherer, K., Fichtner, H., Marsch, E., 2000. The Outer Heliosphere: Beyond the Planets. Copernicus Gesellschaft, e.V., Katlenburg, Lindau.
- Schlickeiser, R., Jan. 1989. Cosmic-ray transport and acceleration. I - Derivation of the kinetic equation and application to cosmic rays in static cold media. II - Cosmic rays in moving cold media with application to diffusive shock wave acceleration. *ApJ* 336, 243–293.
- Schlickeiser, R., Feb. 1994. Cosmic-ray transport and acceleration. *ApJS* 90, 929–936.
- Schlickeiser, R., Miller, J. A., Jan. 1998. Quasi-linear Theory of Cosmic-Ray Transport and Acceleration: The Role of Oblique Magnetohydrodynamic Waves and Transit-Time Damping. *ApJ* 492, 352–378.
- Sokół, J. M., Bzowski, M., Kubiak, M. A., Möbius, E., Jun. 2016. Solar cycle variation of interstellar neutral He, Ne, O density and pick-up ions along the Earth's orbit. *MNRAS* 458, 3691–3704.
- Stix, T., 1992. Waves in Plasmas. American Inst. of Physics.  
URL <https://books.google.de/books?id=OsOWJ8iHpmMC>
- Stone, E. C., Cummings, A. C., McDonald, F. B., Heikkila, B. C., Lal, N., Webber, W. R., Sep. 2005. Voyager 1 Explores the Termination Shock Region and the Heliosheath Beyond. *Science* 309, 2017–2020.
- Tsurutani, B. T., Lakhina, G. S., 1997. Some basic concepts of wave-particle interactions in collisionless plasmas. *Reviews of Geophysics* 35, 491–501.
- Tu, C.-Y., Marsch, E., Jul. 1995. MHD structures, waves and turbulence in the solar wind: Observations and theories. *Space Sci. Rev.* 73, 1–210.

---

Vasyliunas, V. M., Siscoe, G. L., Mar. 1976. On the flux and the energy spectrum of interstellar ions in the solar system. *J. Geophys. Res.* 81, 1247–1252.

Verscharen, D., Marsch, E., May 2011. Apparent temperature anisotropies due to wave activity in the solar wind. *Annales Geophysicae* 29, 909–917.

## 9 Tools and utilities

For this work the following tools were used.

- Python: <https://www.python.org/>
- numpy: <http://www.numpy.org/>
- pylab: <http://scipy.github.io/old-wiki/pages/PyLab>
- matplotlib: <https://matplotlib.org/>
- scipy: <http://www.scipy.org/>
- lmfit <https://lmfit.github.io/lmfit-py/>
- Inkscape: <https://inkscape.org/de/>
- Texmaker: <http://www.xm1math.net/texmaker/>

In addition to the listed tools the following programs were also needed to create the video of appendix F.

- GIMP: <https://www.gimp.org/>
- Windows Movie Maker: <https://support.microsoft.com/de-de/help/18614/windows-essentials>

The provided web links were last accessed on the 19<sup>th</sup> of July, 2017.

---

## 10 Acknowledgments

I wish to thank Christian Drews, Lars Berger and Robert Wimmer-Schweingruber for their guidance and helpful discussions. I also want to thank Eckart Marsch for his helpful suggestions and insights about wave activity in the solar wind. Great thanks also go to the whole work group of extraterrestrial physics at the Kiel University for providing a friendly work climate and making me feel welcome. I also want to thank my parents and the whole family for supporting me throughout the whole time. Thanks also go to everyone, who has encouraged me to study physics - especially my physics teacher Andre Streicher. Without the great physics teaching at school I might not have started studying physics. Finally I want to thank everyone, who has put new coffee into the coffee room.

---

# Appendices

## A Time averaged pitch angle distributions as a function of the wave frequency for initial pitch angles of $105^\circ$ , $120^\circ$ , $150^\circ$ and $175^\circ$ exposed to continuous waves of 0.1 nT amplitude

In addition to the results presented in chapter 5.1.4 the frequency-dependent behavior of initial torus distributions has been investigated for initial pitch angles of  $105^\circ$ ,  $150^\circ$  and  $175^\circ$ . Besides the respective initial pitch angle the boundary conditions are the same as for figs. 33 and 34 of chapter 5.1.4 (consider chapter 4.2 for a detailed presentation of the boundary conditions). The four plots shown in fig. 60 show the frequency-dependent evolution of the time-averaged pitch angle distribution measured with respect to the background field (analogous to fig. 33) and the four plots in fig. 61 depict the pitch angle distribution measured with respect to the total magnetic field (analogous to fig. 34).

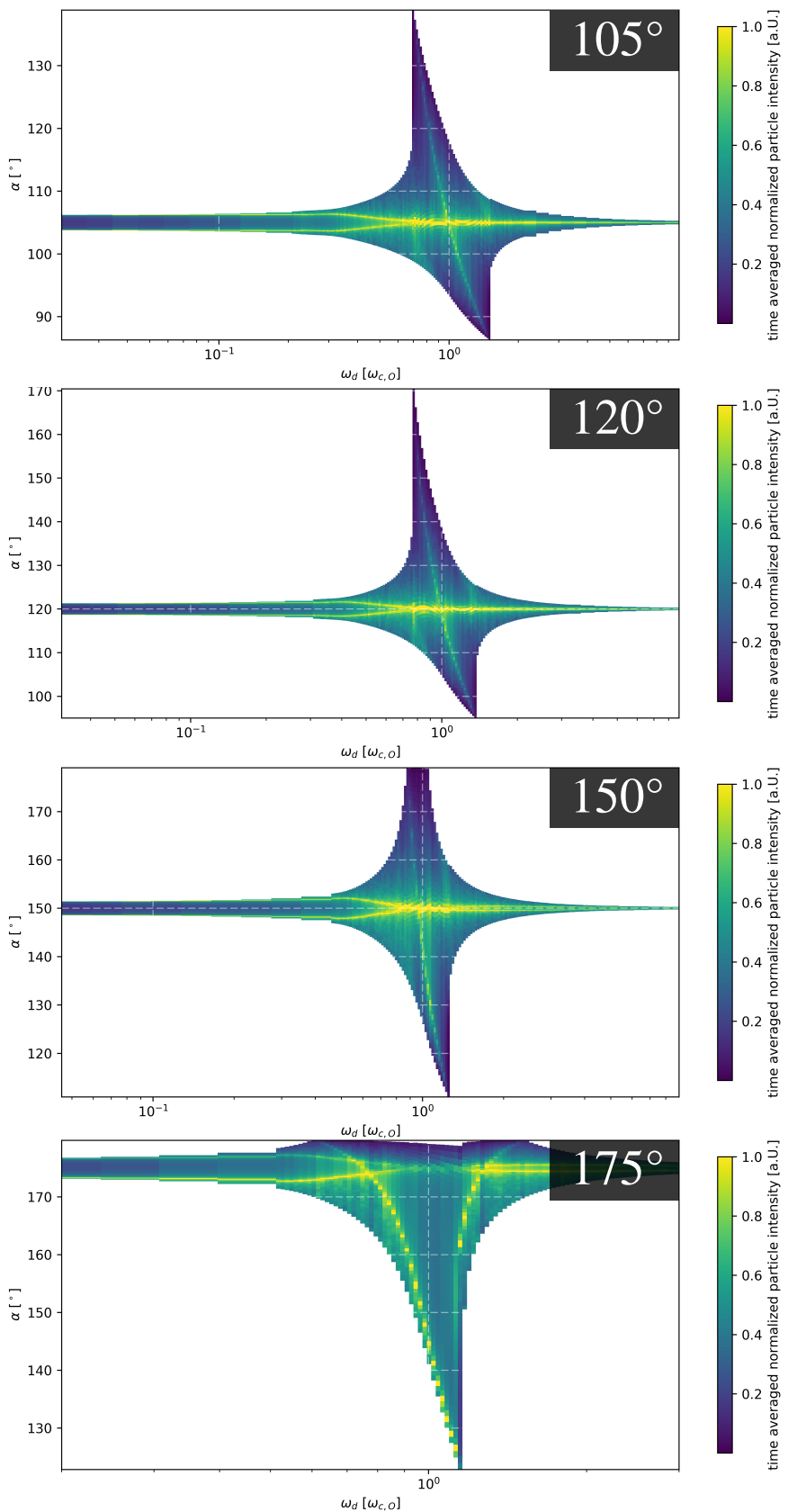


Figure 60: The four plots are analogous to fig. 33, but for pitch angles of  $105^\circ$ ,  $120^\circ$ ,  $150^\circ$  and  $175^\circ$ .

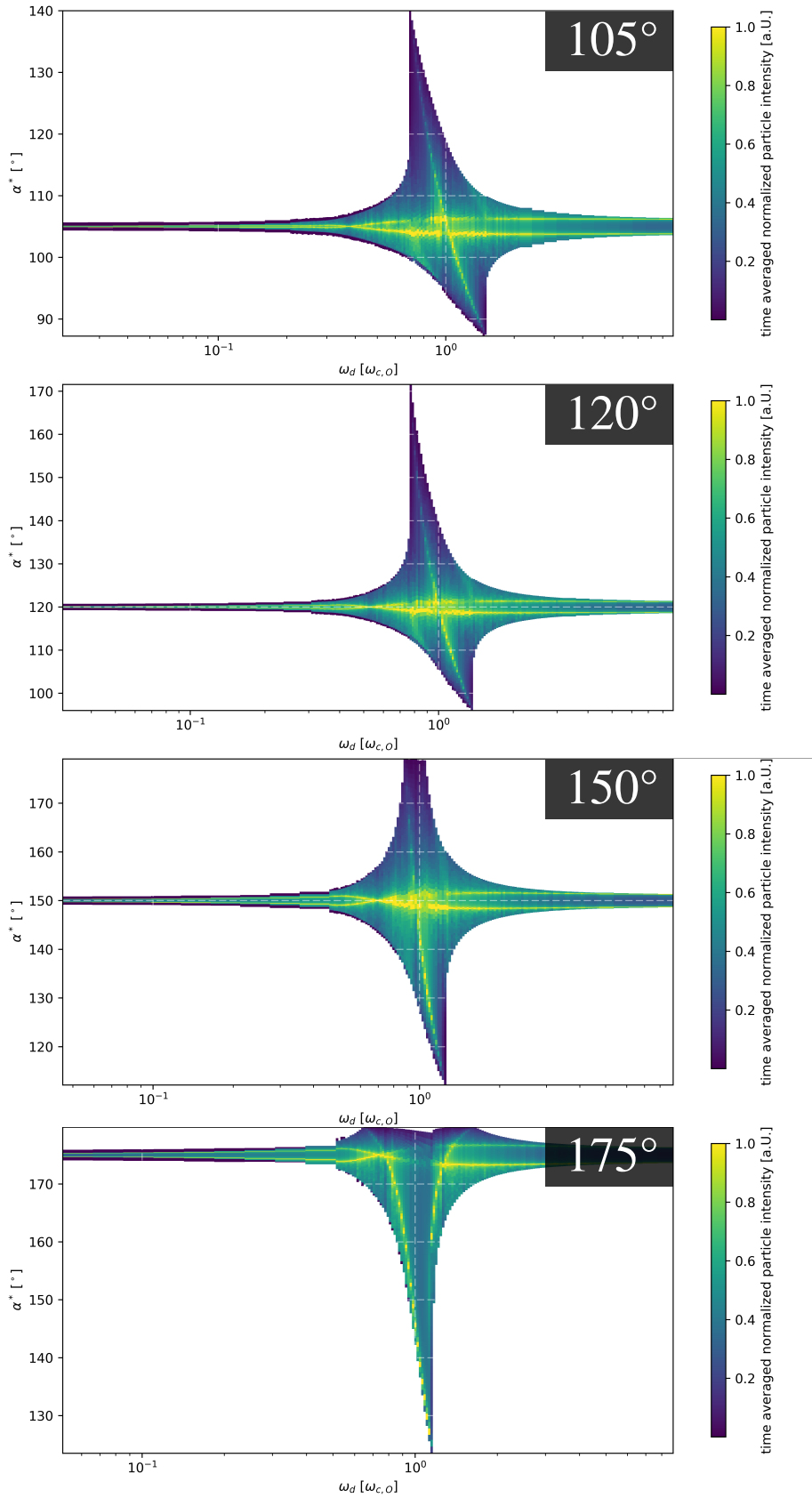


Figure 61: The four plots are analogous to fig. 34, but for pitch angles of  $105^\circ$ ,  $120^\circ$ ,  $150^\circ$  and  $175^\circ$  (The pitch angles are measured with respect to the total magnetic field instead of the background magnetic field).

---

## B Time derivative of the parallel velocity component from Newton's equation

In most simulation setups this work uses a wave magnetic field  $\delta\vec{B} = (\delta B_x, \delta B_y, 0)$  perpendicular and superimposed to a background magnetic field  $\vec{B}_0$  pointing in  $z$ -direction. The electric field is given by a  $\vec{u} \times \vec{B}$  field and is therefore coupled to the wave field. We denote it as  $\delta\vec{E} = (\delta E_x, \delta E_y, 0)$ , which is a vector perpendicular to  $\vec{B}_0$ . The equation of motion given by Newton's second axiom and Lorentz force can then be written as

$$\dot{\vec{v}} = \frac{q}{m} \left( \delta\vec{E} + \vec{v} \times (\vec{B}_0 + \delta\vec{B}) \right) \quad (45)$$

$$\dot{\vec{v}} = \frac{q}{m} \delta\vec{E} + \frac{q}{m} \vec{v} \times \vec{B}_0 + \frac{q}{m} \vec{v} \times \delta\vec{B}. \quad (46)$$

The vector equation's  $z$ -component reads then

$$\dot{v}_z = \frac{q}{m} (v_x \delta B_y - v_y \delta B_x), \text{ where} \quad (47)$$

$v_z$  is a velocity component parallel to the magnetic field and is therefore replaced by  $v_{||}$ . We can also replace the cross product's  $z$ -component by the absolute of the cross product of the perpendicular velocity ( $v_{\perp}$ ) and  $\delta\vec{B}$ , when considering the angle between those quantities. This angle can be interpreted as the phase difference between wave elongation and particle gyration  $\Delta\varphi$ , so that the equation is transformed into

$$\dot{v}_{||} = \frac{q}{m} v_{\perp} \delta B \sin(\Delta\varphi). \quad (48)$$

We now use the conservation of the total energy in the wave frame to state, that the quantity  $\varepsilon = (v_{||} - v_{\varphi})^2 + v_{\perp}^2$  is constant (compare chapter 2.4.2). So its time derivative is 0, which then yields the relation

$$\dot{v}_{\perp} = \dot{v}_{||} \frac{v_{||} - v_{\varphi}}{v_{\perp}}. \quad (49)$$

Inserting this into eq. 48 one obtains

$$\dot{v}_{\perp} = \frac{q\delta B}{m} \sin(\Delta\varphi) (v_{||} - v_{\varphi}), \text{ which} \quad (50)$$

contains interesting factors. The first factor shows, that the change of  $v_{\perp}$  is proportional to the wave amplitude and the particle's charge-per-mass ratio. The second factor makes the derivative proportional to the sine of the phase difference between particle gyration and wave elongation and the third factor is the difference between parallel velocity and wave phase velocity. So the less synchronous the wave and particle are, the larger the magnitude of  $\dot{v}_{\perp}$ . When  $v_{||}$  is larger than  $v_{\varphi}$ ,  $v_{\perp}$  is increased, when the sine is positive. This means a decrease of the difference between  $v_{||}$  and  $v_{\varphi}$ , since  $\varepsilon$  is conserved. So for particles of the right phase the interaction seeks to synchronize wave and particle (the interested reader may also refer to Tsurutani and Lakhina (1997)).

But one needs to be careful interpreting this equation, since  $\Delta\varphi$  is changing over time. It is driven by the difference between particle cyclotron frequency and Doppler shifted wave frequency in the particle frame. We therefore denote

$$\frac{d}{dt} \Delta\varphi = \omega_c - \omega + kv_{||}. \quad (51)$$

Equations 48,49 and 51 create a nonlinear system of coupled differential equations. They have been integrated using Euler's method to obtain fig. 40 in chapter 5.1.5.

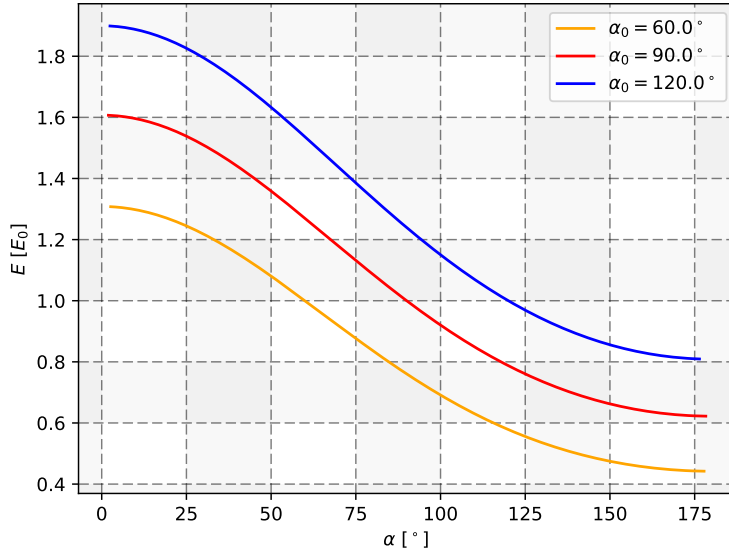


Figure 62: A particle’s energy as a function of its pitch angle, when it is exposed to a wave field of  $0.28\omega_{c,O}$  frequency. The solar wind speed is 450 km/s and the three curves correspond to three different initial pitch angles  $\alpha_0$ .

## C A wave-influenced particle’s energy in the bulk frame as a function of its pitch angle

From the deliberations of chapter 2.4.2 it is well known, that a particle’s energy in the wave frame is conserved, which means for a particle of parallel velocity  $v_{||}$ , perpendicular velocity  $v_{\perp}$  inside a wave field with a phase velocity of  $v_{\varphi}$ , that the quantity  $\varepsilon = (v_{||} - v_{\varphi})^2 + v_{\perp}^2$  is conserved [e.g. Tsurutani and Lakhina (1997)]. Yet, the total energy  $E = (m/2)v^2 = (m/2) \cdot (v_{\perp}^2 + v_{||}^2)$  is not conserved, but a particle’s pitch angle  $\alpha$  can be written as a function of it.

We may normalize the total energy of the particle by dividing it by the particle’s energy at the beginning  $E_0 = (m/2)v_0^2$  and therefore define

$$\tilde{E} = E/E_0 = \frac{v_{\perp}^2}{v_0^2} + \frac{v_{||}^2}{v_0^2}. \quad (52)$$

We then use the conservation of  $\varepsilon$  to obtain  $v_{\perp}^2 = \varepsilon - (v_{||} - v_{\varphi})^2$  and insert it into the equation above to find

$$v_{||} = \frac{1}{2} \left( \frac{v_0^2}{v_{\varphi}} \tilde{E} - \frac{\varepsilon}{v_{\varphi}} + v_{\varphi} \right). \quad (53)$$

From the definition of  $\alpha$  we can denote

$$\alpha = \arccos \left( \frac{v_{||}}{\sqrt{v_{||}^2 + v_{\perp}^2}} \right), \text{ so that} \quad (54)$$

we conclude, that in any wave field a particle’s pitch angle is directly linked to its total energy. For the obtained equation one may first obtain values for  $v_{||}$  as a function of  $\tilde{E}$  from equation 53 and then use the conservation of  $\varepsilon$  to obtain values of  $v_{\perp}$  from these. Then  $\alpha$  can be obtained. For a particle in a wave field of  $0.28\omega_{c,O}$  frequency this has been done to obtain fig. 62.

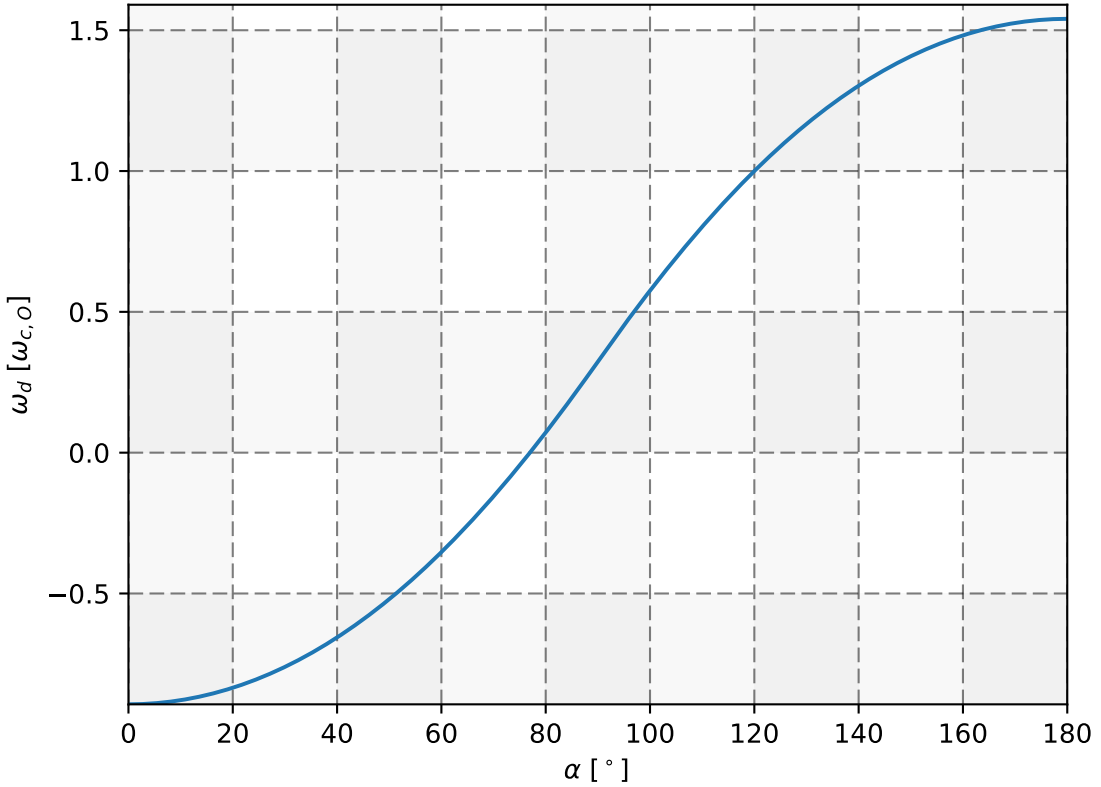


Figure 63: The Doppler shifted wave frequency plotted as a function of the particle's pitch angle.

## D Modification of the parallel velocity by waves

Using the conservation of  $\varepsilon = (v_{||} - v_\varphi)^2 + v_\perp^2$  (compare chapter 2.4.2) the parallel velocity can be derived as a function of the pitch angle for any given initial pitch angle represented by  $\varepsilon$ . We therefore insert  $v_\perp = v_{||} \tan(\alpha)$  and yield a quadratic equation for  $v_{||}$ . Defining  $p := v_\varphi \cos^2(\alpha)$  and  $q := (\varepsilon - v_\varphi^2) \cos^2(\alpha)$  the relation  $v_{||,1/2} = p \pm \sqrt{p^2 + q}$  is obtained. The ambiguity of the equation can be removed by considering, that  $\alpha < 90^\circ$  corresponds to particles moving in positive directions and  $\alpha > 90^\circ$  to particles moving in negative directions. Concluded from the definition of the pitch angle the obtained relation must reach  $v_{||} = 0$  for  $\alpha = 90^\circ$ . So we yield

$$v_{||} = \begin{cases} p + \sqrt{p^2 + q} & \text{if } \alpha < 90^\circ \\ p - \sqrt{p^2 + q} & \text{if } \alpha > 90^\circ \\ 0 & \text{if } \alpha = 90^\circ \end{cases} \quad (55)$$

We may insert this into the Doppler shifted wave frequency  $\omega_d = \omega - k \cdot v_{||}$  in order to find out, how much a change in pitch angle affects resonance.

In the special case of a particle being on a  $120^\circ$  torus at a solar wind speed of 450 km/s and affected by an initially first order resonant wave this is depicted in fig. 63, where negative frequencies correspond to waves being seen with reversed polarizations.

---

## E Implementation of alfvénic waves propagating along the Parker spiral

In a simple configuration, where the background magnetic field points in a constant direction, the transversal alfvénic waves as described in chapter 3.2.1 were physically correct. In the solar wind however, the background magnetic field is an in-ecliptic spiral (see chapter 2.1). Therefore the alfvénic waves - always propagating along magnetic field lines [Prölss (2003)] - won't perform a radial propagation, but a propagation along the spiral. Evidently, this must be considered, when implementing waves in a simulation with underlying solar wind conditions. The following is a work-in-progress description of an implementation of waves propagating along the Parker spiral.

We take a look on the wave function of one of the alfvénic waves described in the foregoing chapter, where the relevant part is given by  $\sin(\vec{k} \bullet \vec{x} - \omega t)$ . It is obvious, that the  $\vec{k} \bullet \vec{x}$ -part describes, how the wave propagates in space. However, it is not responsible for the wave amplitude's direction, which will also change during propagation along the spiral, since it is always perpendicular to it. At this point we drop the vector arrow of  $\vec{k}$  and just consider with  $k$  the component, that is parallel to the magnetic field. Then, instead of  $\vec{x}$  a quantity needs to be put into the wave function, which represents the length  $L$ , that the wave has traveled along the magnetic field line, so that the main part of the wave function becomes  $\sin(k \cdot L - \omega t)$ .

For the studies of this work it is not relevant to actually trace a wave during simulation. Since particle transport is simulated, the focus is set on local field conditions caused by the waves at any particle's location. This means, that a method needs to be found to derive a wave's travel length  $L$  from a given particle's position.

First of all we take a look at the function describing a magnetic field line in the Parker field given by

$$r - r_0 = -\frac{v_{sw}}{\Omega_0 \sin \theta} (\varphi - \varphi_0) \quad [\text{e.g. Scherer et al. (2000)}]. \quad (56)$$

Thereby  $v_{sw}$  is the solar wind speed and  $\Omega_0$  the photospheric rotational period at the latitude  $\theta$ . With  $a := v_{sw}/(\Omega_0 \sin \theta)$  the equation transforms conveniently into  $r(\varphi) = a \cdot (\varphi - \varphi_0) + r_0$ . The problem is (besides the  $\theta$ -dependency of  $a$ ) 2-dimensional. For any given latitude the coordinate system may be rotated, so that the problem fits the in-ecliptic plane (but with a different value of  $a$ ). Hence we will consider the problem in 2-dimensional polar coordinates  $(r, \varphi)$ . Now using  $r(\varphi)$  the length traveled by the wave is calculated with the approach

$$L(\varphi) = \int_{r(\varphi')} ds = \int_{\varphi_0}^{\varphi} \sqrt{r^2(\varphi') + [r'(\varphi')]^2} d\varphi' \quad [\text{e.g. Bronštejn et al. (2012)}]. \quad (57)$$

and with  $r'(\varphi) = a$  and  $\tilde{\varphi}_0 = \varphi_0 - r_0/a^2$  the integral

$$L(\varphi) = a \cdot \int_{\varphi_0}^{\varphi} \left( (\varphi' - \tilde{\varphi}_0)^2 + 1 \right)^{1/2} d\varphi' \quad (58)$$

is obtained. We substitute  $k(\varphi) = \tilde{\varphi}_0^2 - 2\tilde{\varphi}_0\varphi + 1 + \tilde{\varphi}^2$  and  $\Phi(\varphi) = \varphi - \tilde{\varphi}_0$  and obtain from standard integral tables [e.g. Bronštejn et al. (2012)] an antiderivative. Considering  $k(\varphi_0) = 1 + r_0^2/a^4$  and  $\Phi(\varphi_0) = r_0/a^2$  this yields

$$L(\varphi) = a \cdot \frac{\Phi(\varphi)k(\varphi) - \sqrt{k(\varphi)} \cdot \log \left( \sqrt{\Phi^2(\varphi) + 1} - \Phi(\varphi) \right)}{2 \cdot \sqrt{k(\varphi)}} - \frac{a}{2} \cdot \left( \sqrt{\frac{r_0^2}{a^4}} \cdot \frac{r_0}{a^2} - \log \left( \frac{r_0}{a^2} \left( \sqrt{1 + \frac{a^4}{r_0^2}} - 1 \right) \right) \right). \quad (59)$$

In the special case of  $r_0 = 0$ , which will be used in this work, the second part of the difference becomes  $-a \cdot \log(1)/2 = 0$ , which saves computational time. This gives rise to the following algorithm in order to determine the wave's elongation at any particle's location:

- 
- Obtain spherical coordinates  $(r, \theta, \varphi)$  from the particle's position.
  - Determine  $a(\theta)$  and then only consider polar coordinates  $(r, \varphi)$ .
  - Find the starting longitude  $\varphi_0$  of the spiral arm corresponding to  $(r, \varphi)$  using  $\varphi_0 = \varphi - (r - r_0)/a$ .
  - Obtain  $L(\varphi)$  using equation 59.
  - The wave elongation is then given by  $\sin(k \cdot L(\varphi) \pm \omega t + \bar{\varphi})$ .

The  $\pm$  refers to the propagation direction of the wave. A minus corresponds to outward propagating waves (see chapter 2.3.3).  $\bar{\varphi}$  is the wave's phase shift. By creating one wave with  $\bar{\varphi} = 0$  and superimposing it to a wave of perpendicular amplitude vector at the phase shift  $\bar{\varphi} = -\pi/2$ , a circularly polarized wave is created.

Finally the amplitude vectors of the wave need to be determined. Again we will view the problem in the in-ecliptic plane and refer to a rotated problem for locations out of the plane. Then a vector  $\vec{A} = (c\vec{e}_r + d\vec{e})$  perpendicular to the Parker spiral field  $\vec{B}$  at  $(r, \varphi)$  needs to fulfill  $0 = \vec{B} \cdot \vec{A}$ , which transforms with the definition from chapter 2.1 into

$$0 = c - d \frac{\Omega_0 r \sin(\theta)}{v_{sw}}. \quad (60)$$

We set  $d = 1$  and conclude, that then  $c = \Omega_0 r \sin(\theta)/v_{sw}$  applies. So with  $\vec{A}$  the amplitude vector of the first wave is found, that now only needs to be normalized to the wave's magnetic field amplitude. The second wave, superimposed to it, has an amplitude vector pointing into  $z$ -direction. This way, the means of implementing waves propagating along the Parker spiral have been provided.

## F Video: Animated particle velocity under the influence of a continuous mono frequent wave field

The trajectories of two selected particles from fig. 26 (phases: 0 and  $0.5\pi$ ) of chapter 5.1.1 have been animated (compare chapter 4.2 for a detailed view of the boundary conditions). The animation has been written to the compact disc appended to this work. The compact disc is formatted in UDF file system and should therefore be readable by most Windows-based operating systems as well as most Linux-based operating systems. The animation has been written to the root directory with the file name **APPENDIX\_F.mp4**. It has a size of 50.1 MB and is H264-MPEG4 AVC encoded. It has a pixel resolution of  $1920 \times 1080$  with a frame rate of  $\sim 29.97$  frames per second. The audio is encoded via the MPEG AAC Audio codec. The animations shown in the video have been created with *matplotlib* (compare chapter 9). The figures shown in the video have also been created with *matplotlib*, but were modified using *GIMP* (compare chapter 9) to fit the video's pixel resolution. Animated descriptions and text boxes have been added using *Windows Movie Maker* (compare chapter 9). This program was also used to composite the animations and figures into the video file. The video was written to the compact disc using the file explorer of Windows 10.